MASTERARBEIT / MASTER'S THESIS

Titel der Masterarbeit / Title of the Master's Thesis

'The spatial distribution of charged dust particles in the outer solar system'

verfasst von / submitted by

Stefanie Reiter, BSc

angestrebter akademischer Grad / in partial fulfilment of the requirements for the degree of

Master of Science (MSc)

Wien, 2021 / Vienna, 2021

Studienkennzahl lt. Studienblatt / degree programme code as it appears on the student record sheet:	UA 066 861
Studienrichtung lt. Studienblatt / degree programme as it appears on the student record sheet:	Masterstudium Astronomie
Betreut von / Supervisor:	Mag. Dr. Christoph Lhotka

Contents

Acknowledgements

I would like to take this page to thank everyone who has helped me in the process of working on this thesis.

First and foremost, I would like to thank my supervisor Dr. Christoph Lhotka for giving me the opportunity to write this thesis and supporting the process every step of the way, from his insight into working with Mathematica to the many hours spent discussing the results. Thank you also for proofreading the manuscript and for offering many suggestions for improvement!
Secondly, my thanks go to the Austrian Science Found FWF for granting me the opportunity to work on the topic of this thesis as a student assistant in the course of project number P-30542.

I would also like to thank the friends I made in the last few years for the many discussions of exercises during our studies and, most importantly, for offering distractions, especially the many evenings spent playing D&D. Special thanks go to Lukas Winkler for reading over many, many excerpts of this thesis and offering support on all my LaTeX-questions.
Similarly, I would like to thank my friend Pia Elmecker-Plakolm for proofreading the entire thesis and checking for linguistic mistakes. (Especially for pointing out all my long and overly complicated sentences, I hope I was able to reduce at least some of them.) Marina Golzar, thank you for the many hours of listening to me talk about my computations but also for helping me take my mind off of the work. I am very glad I met you.
Finally, I would like to thank my parents for giving me the opportunity to pursue my studies and supporting me in everything I do. Special thanks to my mother for always being there for me and for trying to keep my house plants alive the many times I forgot during the writing process.

Abstract

The aim of this thesis is to study the primary effects of the interplanetary magnetic field on the orbital inclination of charged dust grains positioned in 1:1 mean motion resonance with Jupiter. Observations of the zodiacal light, caused by the scattering of light by micron-sized dust particles, have proven its presence most prominently along the ecliptic plane, but there are also indications of dust bands found at higher ecliptic latitudes, as well. The origin and the cause of this distribution is still unclear. One possible explanation is that the Lorentz force acting on these charged particles may lead to large latitudinal variations, which is supported by the results of this work. In order to study the secular dynamics of charged, micron-sized dust grains in co-orbital motion with Jupiter, a semi-analytical model was developed, focusing on the evolution of the inclination and the longitude of the ascending node. These are the orbital elements most strongly affected by the Lorentz force, and they are therefore used to analyse the particle motion in more detail. Using the Gauss equations, it was possible to reduce the equations of motion in the orbital elements to the dynamically relevant terms containing the long-term evolution of the orbit. Methods of series expansion and temporal averaging were used to determine these results and create the model. In addition, the Newton equations of motion were implemented to numerically compute the full dynamics of the particles.

The model recreates the main features dominating the structure of the parameter space of the inclination and the ascending node, most specifically the existence of both rotational and librational orbits, as well as a minimum amplitude solution. The latter is related to an equilibrium position in terms of the Lorentz force. Further results of the subsequently performed parameter study have shown that the model performs best for particles of medium and large sizes ($\geq 2\,\mu$m). These objects display periodic oscillations in their inclinations, enabling the computations with the model. The orbital planes of the smallest particles behave in a non-periodic manner, according to the results of the numerical simulations.

Additionally, the findings suggest that the proximity to Jupiter is the (early) cause of the disruption of the equilibrium position, as the planet also introduces small variations in the orbital elements, but it does not significantly affect the parameter space otherwise. Simulations of the isolated effect of the interplanetary magnetic field suggest that the orbital planes show the same variations as in the case with the planet, namely a superposition of a secular oscillation (recreated by the model) and higher order harmonics of shorter period lengths (in the full Newton solution). By placing the dust grain at varying solar distances, it was found that these variations of higher frequency are connected to the particle's orbital period.

As far as the combined effect of the magnetic field and the gravitational influence of Jupiter is concerned, we note that the Lorentz force is the dominating influence in the long-term evolution of the orbital plane of micron-sized dust grains. The semi-analytical model developed in this thesis can be used to analyse these secular effects for different particle properties.

1. Introduction

There are a variety of sources from which dust particles located in planetary systems may originate. The most common explanation is that they are created during collisions of asteroids, cometary activity (such as outgassing) or in emission processes. They may also stem from moons and planets in similar ways, by an impact of smaller objects (Koschny et al. 2019) or from plumes extending from the surface. Such is the case for the Saturn moon Enceladus, for example, as was discovered during the *Cassini* flybys (Hansen et al. 2006, see Figure 1.1). Observations have also confirmed particles of interstellar origin in the solar system, as first found in Grün, Zook et al. 1993, by analysing the data from the *Ulysses* spacecraft. These can be differentiated from the particles originating within the solar system due to the direction of their movement and their velocities (for a more in-depth discussion on interstellar dust see e.g. Sterken et al. 2019).

The sizes of the objects – which all together make up the background dust cloud in our solar system – can vary. According to the official definition of dust particles by the IAU Commission F1 as of 2017[1], objects of sizes from submicrons to around 30 µm are referred to as dust particles, while larger objects are termed meteoroids or meteorites (depending on the location in interplanetary space). With this in mind, the examinations done here will mostly focus on analysing the dynamics of particles with a radius of 2 µm. The results for some different sizes will also be studied in comparison to that. It is the dust grains with sizes of some µm, which are responsible for the scattering of sunlight in the solar system, leading to the so-called zodiacal light visible along the ecliptic plane. This effect was already studied by Giovanni Domenico Cassini, among many others.[2] Figure 1.2 shows the zodiacal light with the additional structure of the so-called 'Gegenschein', caused by backscattering of the light in the opposite direction of the sun (Koschny et al. 2019). The observations of the spacecraft Pioneer 10 were crucial for studying the zodiacal light and its connection to the interplanetary dust cloud (Hanner et al. 1976; Matsumoto et al. 2018). Additionally, the data obtained by the Infrared Astronomy Satellite IRAS and the Cosmic Background Explorer COBE (e.g. Dermott et al. 1984 and Berriman et al. 1994, respectively) is further used for analysing the extent and latitudinal variations of the zodiacal light, and hence also the spatial distribution of the associated dust cloud. Observations show some evidence for dust located at higher ecliptic latitudes (Espy et al. 2009), the origin of which is still much debated. This thesis focuses on one possible explanation for the existence of dust grains at such high ecliptic latitudes, namely the influence of the Lorentz force caused by the interplanetary magnetic field.

The dust grain radius strongly influences the effect of different force terms. In contrast to their much larger source objects, dust particles are not only influenced by the gravitational forces

[1] https://www.iau.org/static/science/scientific_bodies/commissions/f1/meteordefinitions_approved.pdf, last accessed on 28.05.2021

[2] Interestingly, Brian May, most widely known for being the lead guitarist of Queen, also worked on the topic of the zodiacal dust cloud and wrote his PhD thesis on the subject (May 2007).

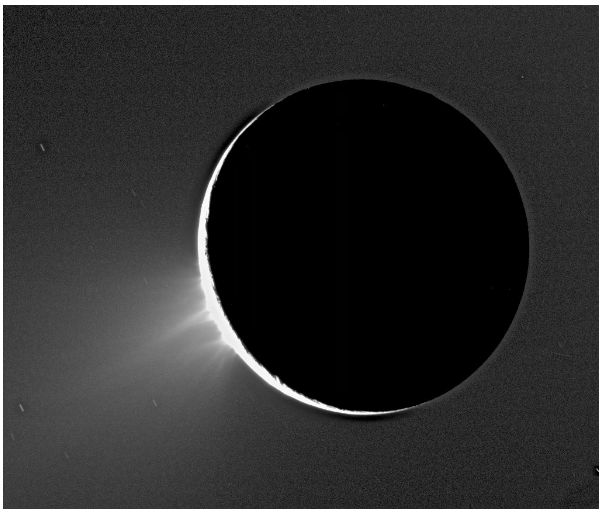

Figure 1.1.: A plume ejecting material from Saturn's moon Enceladus. (Image Credit: NASA/JPL/Space Science Institute, https://photojournal.jpl.nasa.gov/catalog/PIA07758, Public Domain, unaltered)

Figure 1.2.: Observation of the zodiacal light at the La Silla Observatory. (Image Credit: ESO/P. Horálek, https://www.eso.org/public/images/potw1707a/, CC BY 4.0 (https://creativecommons.org/licenses/by/4.0/), unaltered)

within the planetary system, but also by radiative and electromagnetic forces, as well as stellar winds. In combination, these forces determine the particle motion, distributing the small objects throughout the solar system. Depending on the physical parameters of these particles – such as size, shape (Gustafson 1989), composition (Kimura, Okamoto and Mukai 2002), charge – and their initial location after release, the dominating force most strongly influencing the particle dynamics can vary (see also Figure 1 in Lhotka and Galeş 2019). While the stellar gravity typically has the strongest influence on particle motion, the other force terms lead to perturbed Kepler orbits.

On the one hand, the radiation pressure emanating from the central star works in direct opposition to the stellar gravity, as it forces the particle away from its orbit. On the other hand, the so-called Poynting-Robertson effect (Robertson 1937), resulting in loss of angular momentum (which can be understood in the framework of general relativity), and stellar wind particles acting on the dust grains lead to an inward-spiral towards the star. These counteracting forces can lead to more chaotic particle motion, possibly resulting in dust either being blown out of the system by the radiation pressure or spiralling towards the star. Either way, these forces decrease its lifetimes within the planetary system. For further discussion of these effects see e.g. Burns, Lamy and Soter 1979.

Another important factor influencing particle motion is the Lorentz force, which acts on charged objects as they interact with the solar magnetic field, as it is carried further outward in the planetary system by the solar wind. Previous studies analysing the dynamics of dust particles have often neglected this effect, as it most strongly influences very small objects (of less than some µm). In these studies, it is assumed that the dust grains are uncharged. However, there are several processes occurring in the stellar plasma which lead to the charging of the dust particles (e.g. Lhotka, Rubab et al. 2020), the dominant one being photoionisation, resulting in positive surface potentials (Mann et al. 2010) of around 1 V to 10 V (Lhotka, Bourdin and Narita 2016). There have been a number of studies (e.g. Krivov, Kimura and Mann 1998; Lhotka, Bourdin and Narita 2016; Liu and Schmidt 2018a) which have taken into account the interaction of these charged dust grains with the interplanetary magnetic field, finding the dominant effect in a change in the orientation of the particles' orbital planes. In this thesis, we will analyse this effect in detail in the course of a parameter study, and by creating an analytical model qualitatively reproducing the secular evolution of the orbital plane. For the structure of the interplanetary magnetic field, we will assume a generalised Parker spiral model (Parker 1958; Webb et al. 2010). Lhotka and Galeş 2019 have studied the long-term influence of the Lorentz force terms, which will be incorporated into our analytical model.

A more detailed overview on how the different forces affect particle motion can be found in the review paper of Koschny et al. 2019. As this thesis focuses on charged dust particles in the outer solar system, more specifically on dust particles in 1:1 resonance with Jupiter, only the Lorentz force will be incorporated into the computations alongside the gravitational force from the sun and the planet. Additional effects on the results due to the other forces will only be speculated upon in the discussion of the results. This is done in order to be able to study the isolated effects of the interplanetary magnetic field, as it acts on a particle trapped in resonance.

The reasons for the focus on the outer solar system and, more concretely, on the region near Jupiter in general are numerous. Due to the large number of objects located in the outer solar system – in the Kuiper Belt, or comets moving inwards from the Oort Cloud – there is considerable amount of dust found near and beyond Jupiter's orbit. As this is also where the most massive planets are located, the gravitational influence of these bodies are more relevant here than in the inner solar system, especially so in the form of mean motion resonances. These can trap the dust particles and may keep them on stable orbits for extended periods of time, as has been found in a number of previous studies (e.g. Liou and Zook 1995; Liou and Zook 1997). During this time, the radiation pressure and the Poynting-Robertson effect cannot typically dislocate the particle as effectively as outside of resonance.[3] Rather, their effect builds up on these longer timescales until the particle is eventually forced outside of resonance due to the changing parameters of its orbit. Because of this, the neglect of these force terms can be seen as an approximation of the realistic case. The inclusion of these forces would become more important once the particle escapes the resonance. This case is, however, not the focus of this thesis.

[3] Although the solar radiation pressure does cause a simple shift of the location of the resonance due to the reduced effective solar mass, see e.g. Liu and Schmidt 2018b; Kresak 1976.

The case of Jupiter and its Trojan asteroids located along the planet's orbit in the Lagrange points L4 and L5 has been examined more closely in several studies over the last few years (e.g. Liou and Zook 1995). As the Trojans lie in 1:1 resonance with Jupiter, the emerging dust particles may stay on their orbit for a longer time before they are transported outward or inward in the solar system. In the recent study of Liu and Schmidt 2018a and its follow-up paper Liu and Schmidt 2018b, the authors studied the distribution of dust particles originating from the Trojan asteroids, as they are affected by all of the aforementioned forces. They found that a large number of particles can be trapped in the 1:1 resonance for extended periods of time, while others may be ejected from the orbit and can then be trapped in resonances of higher order with Jupiter, or in 1:1 resonance with Saturn, for example. Most interestingly, they found a peak in the inclination distribution for the dust particles with a size of around 1 µm at 40°. This is likely the effect resulting from the Lorentz force, which heavily influences the smaller particles. To create a simplified analytical model explaining and recreating these findings is the main goal of this thesis. As mentioned before, this model will only take into account the effect of the planetary perturbations caused by Jupiter and the effect of the interplanetary magnetic field, as it is assumed to be the cause of the broad vertical distribution found in Liu and Schmidt 2018a.

Another aspect supporting a more detailed study into the regions of the outer solar system is the fact that there already exist several dynamical codes to model the motion and distribution of dust particles in the inner solar system, while there is still a lack of such models for the outer regions. Currently, the two most prominent examples are NASA's Meteoroid Engineering model and ESA's Interplanetary Meteoroid Environment Model. For more information on these also see Koschny et al. 2019 for an overview of both, or McNamara et al. 2004 for the MEM model and Dikarev et al. 2005 for the IMEM model, specifically. Observational data is crucial for the creation of these models, hence the earlier focus on the inner regions. As the future will hopefully also bring an advent of more space missions towards the outer solar system (such as NASA's *Lucy* mission to the Jupiter Trojans[4]), it is advantageous to do preliminary studies on what could be expected for the particle distribution in certain regions, which could then be potentially verified in future observations.

In this thesis, we will do that by analysing the results of two approaches for the computation of the particle dynamics. First, by using the full numerical solution of a particle moving in 1:1 mean motion resonance with Jupiter as it is influenced by the magnetic field. Second, by using a simplified analytical model created from isolating the long-term effects in the parameter space, which the Lorentz force influences most significantly, from the full dynamics. The mathematical background of the two approaches is described in Chapter 2, the derivation of the model in Chapter 3, and the results of the conducted parameter study are analysed in detail in Chapter 4. A more in-depth discussion of what we can conclude from the results for a real dust cloud near Jupiter and what limits the model faces is found in Chapter 5.

[4] https://www.nasa.gov/mission_pages/lucy/overview/index, last accessed on 20.08.2021

2. The Kepler Problem

This chapter focuses on the mathematical framework and definitions used in order to create the model for studying the long-term dynamical evolution of the dust particle. It starts with the basic explanations of the equations and the geometry of the coordinate systems, before going into the derivation of the general equations, which are later used in the computations.

Most of the following sections follow Chapters 1 and 3 and the Appendix Section A.10 of Fitzpatrick 2012, as well as the chapter 'Derivation of Gaussian planetary equations' in the newer online version of this book from 2016[5], and Chapter 1 of Morbidelli 2002. These books were used to work out the derivations and connections between the different coordinate systems and parameters.

2.1. Newtonian Theory of Gravity

The second of Newton's laws of motion states that the change in momentum occurring for a body is equal to (and in the same direction as) the force acting on the body. In order to compute the motion of the object, it is therefore necessary to know how the forces act on the object. In celestial mechanics, the dominant force is the gravitational force between the various bodies, mainly that of the central star in a stellar system. In the simplest case, we would only take into account this aspect, as will be done in these first sections to establish the basics of the calculations.

Gravity is considered a central force, as it works along the line connecting two bodies. As central forces are conservative, the expression for the force $\vec{F}$ can be written as the negative gradient of the gravitational potential energy U, i.e. using $\vec{F} = -\vec{\nabla} U$. Considering a system with only two bodies, the potential energy can be written in terms of

$$U = -\frac{G m_0 m}{|\vec{u}_1 - \vec{u}_2|},$$

with m_0 being the mass of the larger body, m that of the smaller one, G the gravitational constant ($G = 6.674 \cdot 10^{-11}\,\mathrm{m^3 kg^{-1} s^{-2}}$), and the vectors $\vec{u}_1$ and $\vec{u}_2$ as the position vectors of the larger and smaller body, respectively, according to the barycentre of the system.

As both bodies exert a gravitational pull on each other, the forces (here reduced by the mass) can be written as

[5] https://farside.ph.utexas.edu/teaching/celestial/Celestial/Celestialhtml.html, last accessed on 03.08.2021

$$\vec{F}_1 = \ddot{\vec{u}}_1 = \frac{Gm}{\|\vec{u}_1 - \vec{u}_2\|^3}(\vec{u}_2 - \vec{u}_1) \tag{2.1}$$

$$\vec{F}_2 = \ddot{\vec{u}}_2 = \frac{Gm_0}{\|\vec{u}_1 - \vec{u}_2\|^3}(\vec{u}_1 - \vec{u}_2). \tag{2.2}$$

To reduce the number of equations to just one, it is possible to define the relative coordinate $\vec{r} = \vec{u}_2 - \vec{u}_1$, which gives the position vector of the object according to the more massive body.[6] With this, the system reduces to one equation, describing the motion of one body experiencing the effect of an external gravitational force as

$$\ddot{\vec{r}} = -\frac{G(m_0 + m)}{\|\vec{r}\|^3}\vec{r}. \tag{2.3}$$

This can be done because – as the third law of motion states – the forces acting on the two bodies are equal but point in opposite directions. In order to integrate this system, it is necessary to know the initial conditions of both the radius vector $\vec{r}(0) = \vec{r}_0$ and the velocity vector $\dot{\vec{r}}(0) = \dot{\vec{r}}_0$.

Typically, the mass m_0 of the central star is larger by several orders of magnitude than that of the planets or other, smaller objects (especially in the case of dust particles), which is why it is also possible to neglect the smaller mass m.

2.2. The Kepler Elements

While it is possible to study the orbital motion of an object using Cartesian coordinates, it is more practical to use the Kepler elements, which describe the size and the orientation of the orbit in space. For the Cartesian coordinates, the typical frame of reference is constructed in such a way that the orbit lies in the X-Y-plane and the Z-component completes the orthogonal system (towards the ecliptic north). The central star resides in the origin, and the X-axis points towards the periapsis, the point on the orbit closest to the star.

While this reference frame is good enough for studying the motion of one object around the central star, it is not well suited to describe the orbits of a larger number of planets or other bodies, as is pointed out in Fitzpatrick 2012. It is far more useful to study such a problem in the ecliptic reference frame comprised of the coordinates (x, y, z), where the central star again resides in the origin, but the orbital plane of the objects is inclined to that of the ecliptic, which now lies in the x-y-plane and defines the reference frame. In this case, the x-axis points towards the vernal equinox as the typical reference direction, while the z-component again completes the orthogonal system (as shown in Figure 2.1). In this frame of reference, the position vector $\vec{r}$ can be expressed in terms of $\vec{r} = (x, y, z)$.

For the transformation into the ecliptic system, it is necessary to find the Kepler elements describing the orbit. Six such elements exist, with which it is possible to describe the body's

[6] In the solar system, these would be the heliocentric coordinates.

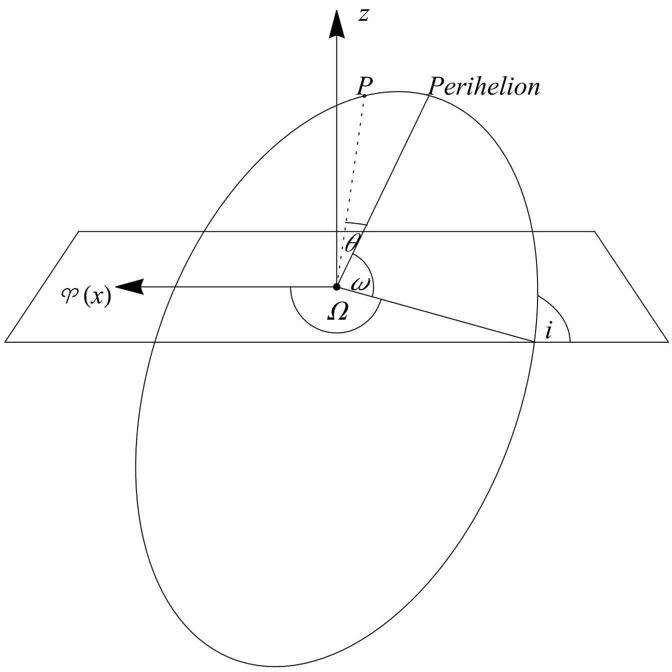

Figure 2.1.: The angular parameters of the orbit give its orientation in space with respect to the ecliptic reference system.

position and velocity at any given time along its orbit. From the first Kepler law, we know that the shape of bound orbits is that of an ellipse. Therefore, the distance of the object to the central star is expressed with the semi-major axis a, which gives the longest distance to the midpoint of the ellipse. On the other hand, the eccentricity e of the orbit defines its ellipticity. If $e \sim 0$, the orbit is roughly circular. This is generally the case for the planets in the solar system.[7]

Considering that the orbit is now inclined to the reference plane – the ecliptic plane – the inclination angle i will also be necessary to transform the coordinate system. If $i \neq 0$, the object's orbit will cross the ecliptic plane in two points. These are the two node points. The ascending node is the one at which the object crosses the ecliptic towards the positive z-axis. The angle between this and the reference point (the vernal equinox) is referred to as the longitude of the ascending node Ω, which can be inferred from Figure 2.1. In the orbital reference plane, the X-axis points towards the periapsis, so for the complete transformation the so-called argument of perihelion ω is also needed, which gives the angle between the ascending node and the object's periapsis.

Lastly, to find the position of the body on its orbit on a given point in time, we would need its true anomaly θ. It is measured as the angle between the perihelion and the vector pointing from the central star (in the focal point of the ellipse) to the object. There are, however, two other definitions for the position of the body, namely the eccentric anomaly E and the mean anomaly M. Contrary to what the name might suggest, the eccentric anomaly is measured on a supposed circular orbit with a radius equal to the semi-major axis of the ellipse. The position of

[7] https://nssdc.gsfc.nasa.gov/planetary/factsheet/, last accessed on 03.08.2021

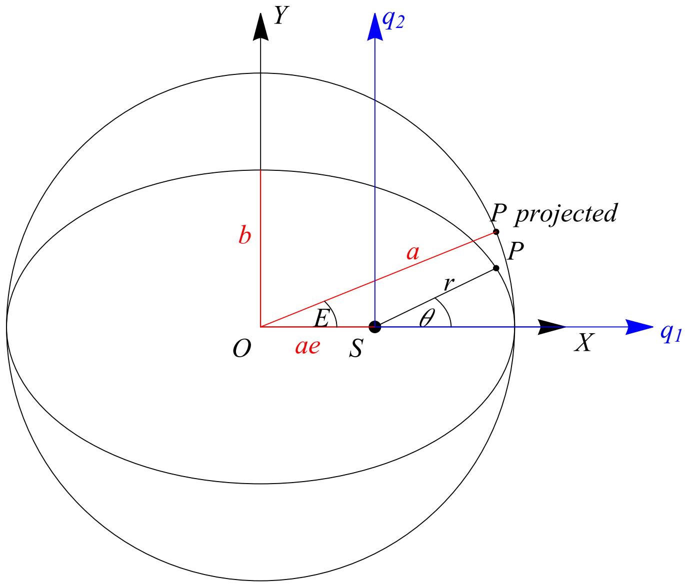

Figure 2.2.: This 2-dimensional sketch shows the geometry of the orbital plane, comparing the actual, elliptic orbit and the projected particle's circular orbit for reference.

the body is projected onto that orbit parallel to the semi-minor axis. Similarly to before, E is then measured as the angle between the perihelion and this projected position as seen from the midpoint of the superimposed circular orbit (which of course coincides with that of the actual orbit). Figure 2.2 demonstrates the geometry for the true and the eccentric anomaly.

The mean anomaly M is again measured on that circular orbit, under the assumption that the body is moving with a constant speed. Using the definition of the mean angular motion of the object as

$$n = \frac{2\pi}{T}, \tag{2.4}$$

with T being the orbital period, the mean anomaly M can therefore simply be defined as $M = n(t - \tau)$, where τ is the time at which the object crosses the perihelion.

2.3. Element conversion

Now that we have defined the Kepler elements, it is relatively simple to see how the transformation from the orbital plane to the ecliptic plane can be done. Before that, however, it is useful to describe the orbit with cylindrical coordinates instead of Cartesian coordinates, so that we have the distance r to the central star and an angular parameter. Making use of these coordinates and the conservation laws within the system, it is possible to describe the orbit in the Kepler elements.

As mentioned in the beginning, the following sections mostly follow the derivations in Chapter 3 of Fitzpatrick 2012 and Chapter 1 of Morbidelli 2002.

2.3.1. Cylindrical coordinates

The unit vectors in a cylindrical system are

$$\vec{e}_r = \begin{pmatrix} \cos\theta \\ \sin\theta \\ 0 \end{pmatrix}, \vec{e}_\theta = \begin{pmatrix} -\sin\theta \\ \cos\theta \\ 0 \end{pmatrix}, \vec{e}_z = \begin{pmatrix} 0 \\ 0 \\ 1 \end{pmatrix}. \tag{2.5}$$

Using these, the radius vector of the orbit can be written as $\vec{q} = r\vec{e}_r$[8] and, taking into account the fact that both r and θ are time-dependent, the time derivative to find the velocity vector yields $\dot{\vec{q}} = \dot{r}\vec{e}_r + r\dot{\theta}\vec{e}_\theta$.

The second derivative of the radius vector gives the acceleration vector, which appears in the equations of motion. We find $\ddot{\vec{q}} = (\ddot{r} - r\dot{\theta}^2)\vec{e}_r + (2\dot{r}\dot{\theta} + r\ddot{\theta})\vec{e}_\theta$. The comparison of this result to (2.3) shows that the acceleration vector can be split into two separate parts of the equations of motion – a radial and a tangential equation comprised by the terms connecting to $\vec{e}_r$ and $\vec{e}_\theta$, respectively, so that we have

$$\ddot{r} - r\dot{\theta}^2 = -\frac{Gm_0}{r^2} \tag{2.6}$$

$$2\dot{r}\dot{\theta} + r\ddot{\theta} = 0. \tag{2.7}$$

In order to solve these equations for r, it is a good idea to rewrite some of these terms using the orbital angular momentum h, which, like the total energy ϵ, is a conserved quantity for the unperturbed two-body problem.

2.3.2. Conservation laws

Any conservative force can be written in terms of the negative gradient of the potential energy. In addition, the general equation of motion from Newton's second law reads $m\frac{d\vec{v}}{dt} = \vec{F}$ and can be expressed as

$$\frac{dK}{dt} = \vec{F}\vec{v},$$

where K gives the kinetic energy written as $mv^2/2$. Hence, the total energy of the system[9] $m\epsilon = K + U$ is constant because

$$\Delta K = \int_{x_1}^{x_2} \vec{F}d\vec{r} = -\int_{x_1}^{x_2} \vec{\nabla}U d\vec{r} = U(x_1) - U(x_2) = -\Delta U, \tag{2.8}$$

[8] To clarify, we note that we use the term $\vec{q}$ for the position vector in the orbital frame. Later, we will use $\vec{r}$ to refer to the vector in the ecliptic frame.

[9] ϵ is given as the specific energy of the system, which means that it equates to the total energy divided by the mass of the object.

as is also discussed in more detail in Section 1.4 of Fitzpatrick 2012. For the Kepler problem, ϵ therefore simply reads

$$\epsilon = \frac{v^2}{2} - \frac{Gm_0}{r}. \tag{2.9}$$

Another conserved quantity is the total (specific) orbital angular momentum in the system. As usual, this quantity is calculated as the cross product of the position and velocity vector in the form of

$$\vec{h} = \vec{q} \times \dot{\vec{q}}. \tag{2.10}$$

Taking into account the expressions for $\vec{q}$ and $\dot{\vec{q}}$ from the previous section, we can see that $\vec{h}$ only has a component in the Z-direction, extending from the orbital plane. The absolute value simply reads

$$h = r^2\dot{\theta}. \tag{2.11}$$

This equation for the angular momentum can be used in the tangential equation of motion, i.e. (2.7), if both sides are multiplied by r. The resulting expression can be rewritten as

$$\frac{d}{dt}(r^2\dot{\theta}) = \frac{dh}{dt} = 0. \tag{2.12}$$

This proves that, if there are no additional non-conservative forces affecting the particle dynamics, the orbital angular momentum is a constant quantity.

Lastly, an additional constant is the so-called eccentricity vector $\vec{V_e}$ (the mass-reduced quantity of the Laplace-Runge-Lenz vector) given by

$$\vec{V_e} = \frac{\dot{\vec{q}} \times \vec{h}}{Gm_0} - \frac{\vec{q}}{r}. \tag{2.13}$$

This vector points from the apoapsis (the point on the body's orbit farthest from the star) to the periapsis and its norm gives the eccentricity e, as explained in Fitzpatrick 2012.

2.3.3. Position and Velocity in the Kepler Elements

Using equation (2.11), we can also rewrite the radial term of the equation of motion, i.e. (2.6), to

$$\ddot{r} - \frac{h^2}{r^3} = -\frac{Gm_0}{r^2}. \tag{2.14}$$

With the help of variable substitution ($r = 1/u(\theta)$), this differential equation can be solved and, when setting one of the integration constants $\theta_0 = 0$ and the other to e (as discussed in Section 3.6 of Fitzpatrick 2012), results for the radius in

$$r = \frac{r_c}{1 + e\cos\theta}. \tag{2.15}$$

Here, the variable r_c encompasses the constants in the equation, so we find $r_c = h^2/Gm_0$. The resulting r forms an ellipse with the eccentricity e. With this, it is also possible to calculate the periapsis and the apoapsis on the orbit. From equation (2.15), it is evident that the smallest value of r is found for $\cos\theta = 1$, and the largest value when $\cos\theta = -1$. Taking into account the geometry of the ellipse with its semi-major axis a from Figure 2.2, these expressions for the distance to the periapsis r_p and to the apoapsis r_a can be explicitly written so that

$$r_p = \frac{r_c}{1+e} = a(1-e) \tag{2.16}$$

$$r_a = \frac{r_c}{1-e} = a(1+e). \tag{2.17}$$

From these equations, we can substitute r_c with $a(1-e^2)$ in (2.15), which hence yields

$$r = \frac{a\left(1-e^2\right)}{e\cos(\theta)+1}. \tag{2.18}$$

Considering that – without the influence of an external perturbing force – a and e remain constant, the time derivative of the previous result yields for the velocity

$$\dot{r} = \frac{a(1-e^2)e\sin(\theta)\dot{\theta}}{(1+e\cos\theta)^2} = \frac{eh\sin(\theta)}{a\,(1-e^2)}. \tag{2.19}$$

It was shown that r_c can be expressed as $a(1-e^2)$. As r_c also relates to h, it is therefore also possible to rewrite the angular momentum with a dependence on the semi-major axis so that

$$h = \sqrt{a(1-e^2)Gm_0} = \sqrt{(1-e^2)}a^2 n. \tag{2.20}$$

The latter expression contains the variable n, which is referred to as the mean motion of the object as it moves on its orbit or, alternatively, as the mean orbital velocity and was already introduced in connection with the mean anomaly M and the orbital period T in equation (2.4). From the third Kepler law, we know that

$$T^2 = \frac{4\pi^2 a^3}{Gm_0} \tag{2.21}$$

$$n^2 = \frac{Gm_0}{a^3}, \tag{2.22}$$

the definition which is used for (2.20). Using the Kepler expressions for r and $\dot{r}$ also allows us to calculate the energy ϵ in terms of the orbital elements. Starting from equation (2.9), expressing the velocity vector in the cylindrical coordinates and subsequently replacing r, $\dot{r}$ and $r^2\theta$ with (2.18), (2.19), and (2.11) yields

$$\epsilon = \frac{\dot{r}^2 + r^2\dot{\theta}^2}{2} - \frac{Gm_0}{r} = -\frac{Gm_0}{2a}, \tag{2.23}$$

which relates to the assumption that a remains constant in the unperturbed problem, as ϵ is a conserved quantity. This equation for the energy also allows the integration of the term $\dot{r}$, using (2.16) for a. This is useful because the result yields the so-called Kepler equation

$$M = E - e \sin E. \tag{2.24}$$

To get to this result, however, a number of steps must be taken in the course of the integration, the main one of them is the substitution of r with the following expression of

$$r = a(1 - e \cos E), \tag{2.25}$$

which introduces the eccentric anomaly E into the equation. This expression for r is then differentiated with respect to E, so that both r and dr can be written in terms of E. After some simplifications and rearranging of variables (which can be found in a some more detail in Section 3.11 of Fitzpatrick 2012), the last step of the integration simplifies to

$$\int_0^E (1 - e \cos E) dE = \sqrt{\frac{Gm_0}{a^3}}(t - \tau), \tag{2.26}$$

which can be solved easily and, with the definition of the mean motion of equation (2.22), results in (2.24).

Additionally, comparing the two expressions for r – equations (2.18) and (2.25) – results in an expression connecting the true anomaly θ of the object and its eccentric anomaly E in the form of

$$\cos\theta = \frac{\cos E - e}{1 - e \cos E}. \tag{2.27}$$

So far, the positional and the velocity vector, now expressed in the orbital elements, describe the two-body problem in cylindrical coordinates for a system in which the body's orbit lies in the X-Y-plane of reference. To transform the coordinate system into the ecliptic system, it is necessary to express the results for the cylindrical coordinates in Cartesian coordinates in order to be able to rotate the system.

2.3.4. System rotation

The periapsis can be written in terms of (2.16) and initially, it lies in the direction of the positive X-axis. Because the origin in the orbital system lies at the location of the central object and not in the midpoint of the ellipse, the X-component of the radius vector expressed in Cartesian coordinates cannot simply be written as (2.16) but rather as

$$X = a(\cos E - e), \tag{2.28}$$

which can be inferred from geometric considerations in Figure 2.2. Similarly, the Y-component lies parallel to the semi-minor axis b but also depends on the position of the object, while the Z-component is zero, which results in

$$Y = a\sqrt{1-e^2}\sin E \tag{2.29}$$

$$Z = 0. \tag{2.30}$$

As pointed out in Section 2.3.1, we use the vector $\vec{q} = (X, Y, Z)$ for the position vector in the orbital frame, in order to avoid confusion with the vector in the ecliptic system, where we will use $\vec{r} = (x, y, z)$ (as in Morbidelli 2002).

Calculating the time derivative of these coordinates again yields the components of the velocity vector. Taking into account the Kepler equation (2.24) and $M = n(t-\tau)$ yields for the derivative of E

$$\frac{dE}{dt} = \frac{n}{1 - e\cos E},$$

so that eventually we find

$$\dot{X} = -\frac{na\sin E}{1 - e\cos E} \tag{2.31}$$

$$\dot{Y} = \frac{na\sqrt{1-e^2}\cos E}{1 - e\cos E} \tag{2.32}$$

$$\dot{Z} = 0 \tag{2.33}$$

for the velocities $\dot{\vec{q}}$ of the Cartesian coordinates expressed in Kepler elements.

The only thing left to do now is the transformation of the orbital reference system into the ecliptic system. As mentioned, the X-axis points towards the perihelion in the orbital reference frame and needs to be transformed in such a way that the x-axis points towards the vernal equinox. As the X-Y-plane lies in the orbital plane, it is first necessary to rotate the system around the Z-axis with ω (compare Figure 2.1). Now, this x'-axis points towards the ascending node. Before we can rotate around Ω, the inclination needs to be accounted for. To do this, we rotate the new x'-axis around i, so that the reference frame is aligned with the ecliptic plane, now residing in the x'-y'-plane. Lastly, we again have a rotation around the z'-axis by the angle Ω to align x with its reference direction towards the vernal equinox. Explicitly, the rotation matrix describing this transformation is written as

$$R_{rot} = \begin{pmatrix} \cos(\omega)\cos(\Omega) - \cos(i)\sin(\omega)\sin(\Omega) & -\sin(\omega)\cos(\Omega) - \cos(i)\cos(\omega)\sin(\Omega) & \sin(i)\sin(\Omega) \\ \cos(i)\sin(\omega)\cos(\Omega) + \cos(\omega)\sin(\Omega) & \cos(i)\cos(\omega)\cos(\Omega) - \sin(\omega)\sin(\Omega) & -\sin(i)\cos(\Omega) \\ \sin(i)\sin(\omega) & \sin(i)\cos(\omega) & \cos(i) \end{pmatrix}. \tag{2.34}$$

This matrix can now be used to transform both the position and the velocity vector of the body from the orbital plane into the ecliptic plane via $\vec{r} = R_{rot}\vec{q}$ and $\dot{\vec{r}} = R_{rot}\dot{\vec{q}}$.

2.3.5. Representation in the orbital elements

The position and the velocity vector, together with a set of initial conditions, can now be used to integrate the equation of motion (2.3) for the two body problem to find the orbit of the object around its central star. The integration process itself is discussed in more detail in the next section. The results will again be given in Cartesian coordinates in the form of $\vec{r} = (x, y, z)$ and $\dot{\vec{r}} = (\dot{x}, \dot{y}, \dot{z})$ and are therefore not the most suitable representation to study the specifics of the dynamical evolution of the orbit. Hence, we will now go in the opposite direction and calculate the orbital elements using the Cartesian coordinates rather than the other way around, again following the framework of Fitzpatrick 2012 and the geometry outlined in Figures 2.1 and 2.2.

As the integration yields both the position and the velocity vector at a given time step, it is possible to calculate the orbital momentum vector $\vec{h}$ using equation (2.10) at any point. The absolute value of this result allows it to derive the semi-major axis from that, as using (2.20) yields

$$a = \frac{h^2}{\mu(1-e^2)}, \tag{2.35}$$

where $\mu = Gm_0$.

However, this calculation already requires the knowledge of the eccentricity e, which, as explained in Section 2.3.2, is simply given as the norm of the eccentricity vector (2.13), so that we have

$$e = \left\|\vec{V}_e\right\| = \left\|\frac{\dot{\vec{r}} \times (\vec{r} \times \dot{\vec{r}})}{\mu} - \frac{\vec{r}}{r}\right\|. \tag{2.36}$$

The inclination angle i can be inferred from $\vec{h}$, as well. As the orbital angular momentum vector is perpendicular to the orbit itself, we find, from the projection of $\vec{h}$ on to the z-axis in the ecliptic reference system, that

$$i = \arccos \frac{h_z}{\left\|\vec{h}\right\|}. \tag{2.37}$$

For ω and Ω, an additional vector can be constructed to simplify the problem, namely the vector $\vec{N}$ pointing towards the ascending node, formed as $\vec{N} = (-h_y, h_x, 0)$. Together with the x-axis in the ecliptic reference system, $\vec{N}$ gives the longitude of the ascending node, resulting for the angle between them in

$$\Omega = \arccos \frac{-h_y}{\left\|\vec{N}\right\|}. \tag{2.38}$$

The argument of perihelion on the other hand can be directly derived as the angle between $\vec{N}$ and the eccentricity vector, which points towards the direction of the perihelion as pointed out in Section 2.3.2. Hence, ω is simply derived via

$$\omega = \arccos \frac{\vec{N}\vec{V}_e}{\left\|\vec{N}\right\| \cdot \left\|\vec{V}_e\right\|}. \tag{2.39}$$

The last parameter needed for the set of six orbital elements describing the object's orbit is the mean anomaly M. However, this angle cannot be derived directly from the integrated parameters, as both the mean anomaly and the eccentric anomaly are measured on the superimposed circular orbit. The true anomaly θ, on the other hand, can be calculated as the angle between the eccentricity vector $\vec{V}_e$ and the position vector of the object $\vec{r}$ (see Figure 2.2), so that

$$\cos\theta = \frac{\vec{V}_e \cdot \vec{r}}{er}. \tag{2.40}$$

This result is plugged into (2.27), which can then be rewritten in terms of E to

$$E = \arccos \frac{\cos\theta + e}{1 + e\cos\theta}. \tag{2.41}$$

The last step is then to simply use this result in the Kepler equation (2.24) to compute the mean anomaly M.

Strictly speaking, these calculations only work as long as the object is not moving on a completely circular orbit (i.e. $e \neq 0$), and the orbit is inclined towards the ecliptic plane. If the latter was not the case, the argument of perihelion and the longitude of the ascending node are not defined, as there would not be an ascending node. To avoid this problem, it is also possible to define the longitude of perihelion $\varpi = \omega + \Omega$ as the angle between the vernal equinox and the perihelion (Morbidelli 2002, p.16). Additionally, if $e = 0$, there would be no periapsis to define this angle, either. To ensure that this will not be a problem for the computations, the minimum value for e is set to 10^{-12}. Furthermore, all simulations runs of the following chapters will use a minimum inclination of $i = 1°$.

2.4. Numerical Solution and Series Expansion

Using the Runge-Kutta method for the `NDSolve` function in Mathematica, it is fairly simple to perform numerical integration of the equations of motion as they are now with any given set of initial conditions. This can be done by rewriting the three second order differential equations we get for (2.3) into six differential equations of the first order by setting $\dot{x} = v_x$ and so on. This leads to the following set of equations:

$$\dot{x} = v_x \qquad \dot{v}_x = -\frac{Gm_0 x}{(x^2+y^2+z^2)^{3/2}} \tag{2.42}$$

$$\dot{y} = v_y \qquad \dot{v}_y = -\frac{Gm_0 y}{(x^2+y^2+z^2)^{3/2}} \tag{2.43}$$

$$\dot{z} = v_z \qquad \dot{v}_z = -\frac{Gm_0 z}{(x^2+y^2+z^2)^{3/2}}, \tag{2.44}$$

with $x(0) = x_0$, $y(0) = y_0$ and $z(0) = z_0$ needed for the initial conditions of the position vector, and $v_x(0) = v_{x,0}$, $v_y(0) = v_{y,0}$ and $v_z(0) = v_{z,0}$ as the initial values of the velocity vector.

However, it is also possible to expand the equations of the Kepler problem into a series of the eccentricity using the Bessel equations, as is also explained in Appendix A.10 of Fitzpatrick 2012 (with the formulas of Gradshteyn and Ryzhik 1980). This can be done because the Bessel equations of the first kind $J_n(x)$ (where n determines the order to which the series is expanded) can be written as

$$J_n(x) = \frac{1}{2\pi} \oint e^{-i(n\Phi - x\sin\Phi)} d\Phi. \tag{2.45}$$

This is used as the coefficient in the Fourier series expansion of the function $e^{ix\sin\Phi}$. A similar form can be found when the eccentric anomaly E is expanded into a Fourier series in terms of the mean anomaly, so that $e^{iE} = \sum_{n=-\infty}^{\infty} A_n e^{inM}$.

The coefficients A_n can be expressed – using the Kepler equation (2.24) – in terms of

$$A_n = \frac{1}{2\pi n} \oint e^{-i[(n-1)E - ne\sin E]} dE = \frac{J_{n-1}(ne)}{n}. \tag{2.46}$$

The fact that the last term can be written so that it includes the Bessel function is evident when comparing the exponent in this integral to that of equation (2.45).

With these expressions, it is possible to expand both the terms $cos(E)$ and $sin(E)$, and – with the latter used in combination with the Kepler equation (2.24) – E into a Fourier series in terms of the eccentricity e, using the Taylor expansion of the Bessel function as shown in Fitzpatrick 2012, p.229. The general form of the first two terms (see Dvorak and Lhotka 2013) yields

$$\cos E = -\frac{e}{2} + 2\sum_{k=1}^{\infty} \frac{\mathrm{d}J_k(ke)}{\mathrm{d}e} \frac{\cos(kM)}{k^2} \tag{2.47}$$

$$\sin E = \frac{2}{e}\sum_{k=1}^{\infty} J_k(ke) \frac{\sin(kM)}{k}. \tag{2.48}$$

In this thesis, we will further use the series expansion up to the second order in e. The results can be seen in Appendix A. From the Kepler equation (2.24), we find for the eccentric anomaly itself

$$E = M + 2\sum_{k=1}^{\infty} J_k(ke) \frac{\sin(kM)}{k}, \tag{2.49}$$

using (2.48).

As r can also be expressed in terms of E, i.e. (2.25), it is also possible to expand r into a Fourier series by simply plugging in the expression of $cos(E)$, which yields

$$\frac{r}{a} = 1 + \frac{e^2}{2} - 2e\sum_{k=1}^{\infty} \frac{\mathrm{d}J_k(ke)}{\mathrm{d}e} \frac{\cos(kM)}{k^2}. \tag{2.50}$$

For the true anomaly θ, the same is done: using equation (2.11), we can write

$$\frac{d\theta}{dt} = \frac{d\theta}{dM}\frac{dM}{dt} = (1-e^2)^{1/2} n \frac{a^2}{r^2} = (1-e^2)^{1/2} \frac{dM}{dt}\left(\frac{dE}{dM}\right)^2 \tag{2.51}$$

$$\frac{d\theta}{dM} = (1-e^2)^{1/2}\left(\frac{dE}{dM}\right)^2, \tag{2.52}$$

taking into account the derivative of the Kepler equation with respect to E yielding $\frac{dM}{dE} = 1 - \cos E = \frac{r}{a}$. Solving this differential equation using the already expanded value for E of (2.49) gives the series expansion of θ in e.

The same can be done for the Cartesian coordinates as well, using the results from Section 2.3.4 for $\vec{q}$ and $\dot{\vec{q}}$, where we can again plug in the expressions resulting from (2.47) and (2.48). These then still need to be transformed into the ecliptic system using (2.34) in order to find $\vec{r}$ and $\dot{\vec{r}}$. As before for the velocity vector, we can alternatively also take the time derivative of the expanded position vector. The resulting equations for the series expansions of the position and velocity vectors in the ecliptic system up to the second order in e can also be found in Appendix A.

With these equations, it is now possible to calculate the position and velocity vector of an object at any given point in time without doing a full integration under the condition that the Kepler elements are constant (except for M, from which the time-dependency arises). This is the case if there is no additional perturbing force.

2.5. Additional external forces

The calculations so far have only taken into account the gravitational influence of the central body on the orbiting object. However, in a realistic star system, there are several other forces that affect orbital motion as well, such as gravitational interaction of the planets or asteroids with each other and the influence of the interplanetary magnetic field, as will be studied in detail in the next chapters. It is therefore necessary to account for external perturbing forces as well, which are introduced into the equation of motion according to

$$\ddot{\vec{r}} + \mu \frac{\vec{r}}{r^3} = \vec{F}, \tag{2.53}$$

where $\vec{F}$ represents an arbitrary force term, which in this case is assumed to already be reduced by the particle mass. Due to the inclusion of this perturbing force, it is no longer possible to assume conservation of the total energy and total angular momentum. Taking into account the equations (2.23) and (2.10), this also means that the orbital elements do not remain constant but vary with time as well. This can be modelled by using the so-called Gauss equations, which are constructed under the assumption that the dominant force term is the solar gravity and that the perturbed object therefore moves on Keplerian orbits. The variation equations of the orbital elements can be constructed by taking the time derivatives of the equations from Section 2.3.5 and taking into account that ϵ and $\vec{h}$ are no longer conserved quantities. The derivations follow the outline of the additional chapter 'Derivation of Gauss planetary equations'[10] of the online version of Fitzpatrick 2012 (hereafter Fitzpatrick 2016).

As we look at the problem in cylindrical coordinates, we can write a general term for any force as $\vec{F} = F_r \vec{e}_r + F_\theta \vec{e}_\theta + F_z \vec{e}_z$.

2.5.1. Gauss equations

The time derivative of the energy can be expressed in terms of $\dot{\epsilon} = \dot{\vec{q}}\vec{F}$, the force times the particle velocity in the form of $\dot{\vec{q}} = \dot{r}\vec{e}_r + r\dot{\theta}\vec{e}_\theta$. Alternatively, taking the time derivative of equation (2.23) yields $\dot{\epsilon} = \frac{\mu \dot{a}}{2a^2}$. Equating these two expressions of the energy and solving for a eventually yields

$$\frac{\dot{a}}{a} = \frac{2h(F_\theta(e\cos(\theta) + 1) + eF_r \sin(\theta))}{(1 - e^2)\,\mu}. \tag{2.54}$$

This expression gives the variation of the semi-major axis with time as a function of the other Kepler elements and of the perturbing force. From (2.54), we can also see that a varies with time due to the influence of the radial and the tangential component of the force, meaning that any orthogonal force components have no effect on the evolution of the semi-major axis.

[10] https://farside.ph.utexas.edu/teaching/celestial/Celestial/node160.html, last accessed on 03.08.2021

The influence of the perturbing force not only leads to a variation of the total energy with time, but also to a change in the total orbital angular momentum $\vec{h}$. The time derivative of (2.10) can be written as

$$\dot{\vec{h}} = \vec{q} \times \vec{F}, \tag{2.55}$$

since the cross product of $\vec{q}$ with itself is zero. This change of $\vec{h}$ comes into play when taking the time derivative of the eccentricity vector $\vec{V}_e$, as can be derived from equation (2.13). Plugging in the definition of both of these vectors, we get

$$\dot{\vec{V}}_e = \begin{pmatrix} \frac{F_\theta r\left(\frac{eh\sin^2(\theta)}{a(1-e^2)}+\frac{2h\cos(\theta)}{r}\right)}{\mu} + \frac{F_r h\sin(\theta)}{\mu} \\ \frac{F_\theta r\left(\frac{2h\sin(\theta)}{r}-\frac{eh\sin(\theta)\cos(\theta)}{a(1-e^2)}\right)}{\mu} - \frac{F_r h\cos(\theta)}{\mu} \\ -\frac{eF_z hr\sin(\theta)}{a(1-e^2)\mu} \end{pmatrix}. \tag{2.56}$$

As these calculations still occur in the orbital reference frame, the time derivative of the eccentricity value $\dot{e}$ is still taken as the value in the X-direction. Simplifying the terms further using the eccentric anomaly E from (2.27) eventually yields

$$\dot{e} = \frac{h(F_\theta(\cos(\mathrm{E})+\cos(\theta))+F_r\sin(\theta))}{\mu}. \tag{2.57}$$

Similarly as for the time variation of the semi-major axis, the eccentricity does not vary due to an influence of the orthogonal force component, but only due to that of the radial and tangential components.

While these derivations are relatively straightforward, the Gauss equations for the angular quantities are a bit more complicated. Taking the time derivative of the radius representation in (2.25) and equating it to the velocity equation of (2.19) allows solving for $\dot{E}$, yielding

$$\dot{r} = \frac{n}{1-e\cos E} - \frac{\dot{a}}{a}\frac{1-e\cos E}{e\sin E} + \frac{\dot{e}}{e}\frac{\cos E}{\sin E}. \tag{2.58}$$

This solution can then be applied to the time derivative of the Kepler equation from (2.24), for which we have

$$\dot{M} = \dot{E}(1-e\cos E) - \dot{e}\sin E. \tag{2.59}$$

Here, we also need the solutions we previously found for $\dot{a}$ and $\dot{e}$, in equations (2.54) and (2.57). In the end, the most simplified version of the Gauss equation for the mean anomaly yields

$$\dot{M} = n + \frac{\sqrt{1-e^2}h\left(F_r\left(\cos(\theta)-\frac{2er}{a(1-e^2)}\right)-F_\theta\sin(\theta)\left(\frac{r}{a(1-e^2)}+1\right)\right)}{e\mu}. \tag{2.60}$$

As before, it is apparent that only the radial and tangential force components lead to additional changes of the mean anomaly with time. Similarly to the unperturbed case, the mean motion n of the body is present in the equation, as well.

To get the Gaussian variation equations for the angles depicting the orientation of the orbit in space, it is necessary to transform the coordinate system from the orbital reference system to the ecliptic system. It is possible to either first rotate the system and then take the time derivative, or the other way around.

Earlier, we have already derived the variation equation for the total angular momentum vector using (2.55). This result can be rotated into the correct reference frame using (2.34). However, doing the rotation of $\vec{h}$ and then taking the time derivative introduces a variation of i (as well as of Ω). Equating the z-components of the two versions of $\dot{\vec{h}}$ allows solving for $\frac{\mathrm{d}i}{\mathrm{d}t}$ (for the full formulation of the $\dot{\vec{h}}$-terms, refer to Fitzpatrick 2016[11]), yielding

$$\frac{\mathrm{d}i}{\mathrm{d}t} = \frac{F_z r \cos(\theta + \omega)}{h}. \tag{2.61}$$

Contrary to the previous equations, we see here that the inclination varies due to the influence of an orthogonal force component, rather than the radial and tangential component. Additionally, the argument of perihelion also influences the evolution of i, while for a, e, and M the only angular term came from the true anomaly θ (or the eccentric anomaly E).

The derivation of $\dot{\Omega}$ is not as clear-cut. For this, we again use both versions of $\vec{h}$ and $\dot{\vec{h}}$. However, to get a proper solution, we calculate $h_x \dot{h}_y - \dot{h}_x h_y$ for both versions and then equate the two terms. After quite some cancelling down, we find the Gauss equation of the longitude of the ascending node as follows:

$$\dot{\Omega} = \frac{F_z r \sin(\theta + \omega)}{h \sin i}. \tag{2.62}$$

Similarly to the inclination, the changes with time on the ascending node arise due to the orthogonal force component acting on the object and also depend on the evolution in both ω and θ. In contrast, the variation in Ω additionally shows a dependence on the variation in i.

The last quantity in need of computing is the argument of perihelion, for which a similar route can be taken: Rotating the eccentricity vector using (2.34), then taking the time derivative of the z-component (as it yields the simplest equation to solve) and equating it to that of the rotated time derivative from (2.56) eventually (again, after some algebra) results in

$$\dot{\omega} = -\frac{h\left(F_r \cos(\theta) - \frac{F_\theta \sin(\theta)(e\cos(\theta)+2)}{e\cos(\theta)+1}\right)}{e\mu} - \frac{F_z r \cot(i) \sin(\theta + \omega)}{h}. \tag{2.63}$$

Different to the other quantities, $\dot{\omega}$ depends on all components of the perturbing force vector, as well as showing some additional dependence on the inclination, similar to $\dot{\Omega}$.

[11] https://farside.ph.utexas.edu/teaching/celestial/Celestial/node163.html, last accessed on 28.05.2021

2.5.2. Forces in the Gaussian system

Similarly to the transformation of the coordinate system, it is also necessary to find the correct expressions for the radial, tangential and orthogonal force components in the ecliptic reference frame and the orbital elements. Additionally, the force needs to be evaluated as to how it acts on the object at a given point in time. Therefore, it needs to be examined in a rotating system, as it follows the body according to its true anomaly θ. So in order to find the components F_r, F_θ and F_z, the three unit vectors from (2.5) need to be rotated to the ecliptic frame according to (2.34) and then multiplied with the force vector in the Cartesian coordinates, to account for the influence of the force in the radial, tangential and orthogonal direction, which is explained in more detail in Moulton 1914, p.402 sq.[12] This general expression yields the following results[13]

$$\begin{aligned} F_r = & F_X(\cos(u)\cos(\Omega) - \cos(i)\sin(u)\sin(\Omega)) \\ & + F_Y(\cos(i)\sin(u)\cos(\Omega) + \cos(u)\sin(\Omega)) \\ & + F_{Z,c}\sin(i)\sin(u) \end{aligned} \tag{2.64}$$

$$\begin{aligned} F_\theta = & F_X(\sin(u)(-\cos(\Omega)) - \cos(i)\cos(u)\sin(\Omega)) \\ & + F_Y(\cos(i)\cos(u)\cos(\Omega) - \sin(u)\sin(\Omega)) \\ & + F_{Z,c}\sin(i)\cos(u) \end{aligned} \tag{2.65}$$

$$F_z = F_X\sin(i)\sin(\Omega) - F_Y\sin(i)\cos(\Omega) + F_{Z,c}\cos(i). \tag{2.66}$$

Here, the trigonometric terms for ω and θ are combined within the variable u, which is referred to as the true longitude, accounting for the angle between the vector connecting the central star and the object at a given moment in time and the ascending node, rather than the perihelion (hence $u = \omega + \theta$).

Using the series expansion of θ from Section 2.4, it is possible to also expand the true longitude in the eccentricity (see Appendix A). These terms can then be plugged into the force equations from above. The vector components F_X, F_Y and $F_{Z,c}$ are here already assumed to be expressed in the orbital elements. In order to see how the inclusion of an external influence can be done for individual forces, we will first look at a simplified example.

The simplest case to consider for a perturbing external force is a constant component in any arbitrary direction. Here, we focus on studying the effects of a force vector pointing only in the Z-direction with a constant value of C in the form of

$$\vec{F} = \begin{pmatrix} 0 \\ 0 \\ C \end{pmatrix}. \tag{2.67}$$

Using this vector in equations (2.64) – (2.66), we only find the cylindrical components containing terms of $F_{Z,c}$.

[12] For the sake of comparability, it should be noted that the radial, tangential and orthogonal force components denoted in this thesis as F_r, F_θ and F_z are referred to as R, S and W in the book.

[13] Note that the term $F_{Z,c}$ corresponds to the Z-component of the forces in the Cartesian coordinates, while F_z refers to the orthogonal component in cylindrical coordinates in the ecliptic system.

x_0	y_0	z_0	$v_{x,0}$	$v_{y,0}$	$v_{z,0}$
$3.853 \cdot 10^{11}$m	$6.446 \cdot 10^{11}$m	$1.727 \cdot 10^{11}$m	$-11\,421.4$ m/s	6369.47 m/s	1706.7 m/s
a_0	e_0	i_0	ω_0	Ω_0	M_0
$7.784 \cdot 10^{11}$m	0.01	15°	60°	0°	0°

Table 2.1.: The initial conditions used for integration in Cartesian coordinates (Newton) and orbital elements (Gauss, conversion as in Section 2.3).

For the Newton approach, the integration of the now perturbed Kepler problem can be done by utilising the equations of motion similarly as given in Section 2.4, but instead of using the set of equations of (2.42) – (2.44), they now read

$$\dot{x} = v_x \qquad \dot{v}_x = -\frac{Gm_0 x}{(x^2+y^2+z^2)^{3/2}} \tag{2.68}$$

$$\dot{y} = v_y \qquad \dot{v}_y = -\frac{Gm_0 y}{(x^2+y^2+z^2)^{3/2}} \tag{2.69}$$

$$\dot{z} = v_z \qquad \dot{v}_z = C - \frac{Gm_0 z}{(x^2+y^2+z^2)^{3/2}}. \tag{2.70}$$

The initial conditions for integration can be found in Table 2.1. On the one hand, the resulting values for the position and velocity vector of the Newton integration can now be transformed back into the Kepler elements according to the equations in Section 2.3.5, i.e. (2.35) – (2.39), (2.41), and (2.24) after the integration. On the other hand, it is also possible to directly compute the orbital elements using the Gauss equations, as they now vary with time due to the external force. To do this, the cylindrical force components F_r, F_θ and F_z are used in (2.54), (2.57) and (2.60) – (2.63). We use the series expansion in the true longitude u (as explained in Section 2.4 and given in Appendix A) to express the force terms in the orbital elements, as well as the expansion in E, θ, and r – from (2.49), (2.52), and (2.50), respectively – to be able to compute the Gauss equations. The resulting change in the Kepler elements in comparison of the Newton and the Gauss approach for the example of a and ω can be seen in Figure 2.3. This comparison between these two methods shows that the resulting mismatch in the Gaussian solution is relatively small. The magnitude of the expansion error depends on the order in e that enters the calculations for the angular parameters, E, M, u, and the radius r. Using expansions of these parameters in e up to the second order means that the lower limit for the error is $\sim e^3$. This magnitude is not necessarily reached, as the error also depends on the value used for the constant C, as well as the numerical integration scheme. Additionally, it also has to be kept in mind that the error adds up over time in the course of the integration, eventually leading to a greater deviation on longer timescales.

Table 2.2 shows a comparison between two simulation runs with different C values. Here, we see the expansion error as the largest differences (σ) for each of the orbital elements between the Gaussian results and the full solution after an integration time of 200 yr. Due to the value used for e, the assumption of the error due to the expansion would be of the order of 10^{-6}. This seems to be fulfilled in the case of the smaller constant, while a larger perturbing force term appears to induce greater deviations from the full solution in the approximated results. The results also show that the expansion error for the angular parameters ω and M are larger

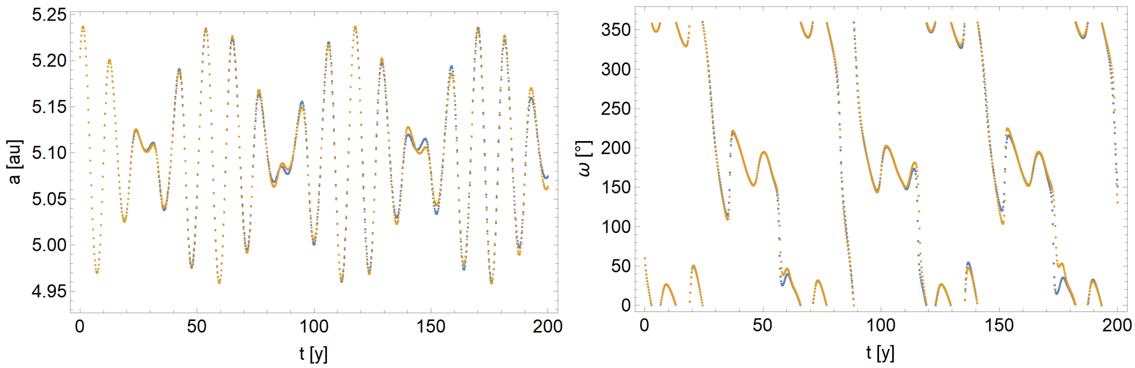

(a) Semi-major axis a

(b) Argument of the perihelion ω

Figure 2.3.: Evolution in a and ω of a dust particle affected by a constant force term $C = 0.1$ for the full Newton solution (blue) and the Gaussian series expansion (orange).

C	$\sigma(a)[AU]$	$\sigma(e)$	$\sigma(i)[°]$	$\sigma(\omega)[°]$	$\sigma(\Omega)[°]$	$\sigma(M)[°]$
0.000 01	$7.448 \cdot 10^{-6}$	$1.078 \cdot 10^{-6}$	$1.576 \cdot 10^{-8}$	0.005	$8.538 \cdot 10^{-7}$	0.005
0.1	0.012	0.016	1.026	89.726	30.915	89.289

Table 2.2.: A comparison in the values of the expansion errors σ in the Kepler elements for two different constant force terms C.

compared to that of the others. This is also noticeable in the example of the dynamics of ω in Figure 2.3b, where we see some larger deviations in the Gaussian solution from the Newton case, especially so after quick changes in ω. On the one hand, this can be understood from the Gauss equations of the angular terms ω and M, (2.63) and (2.60). Both terms are additionally divided by the eccentricity, meaning that the order here is effectively smaller by one order in e, resulting in a poorer fit in comparison. On the other hand, the perturbing force term resulting from (2.64) – (2.66) induces a strong change in these angular terms, leading them to pass through all possible values in the range of $[0, 360]°$, resulting in the (comparatively) large differences in Table 2.2. Effectively, these differences for ω and M in both simulation runs (and in Ω for the larger force term) indicate that the expanded Gauss model has some difficulties in accurately reproducing quick changes in the evolution of the orbital elements over a relatively large value interval.

Figure 2.3a also demonstrates that the oscillation in a is seemingly made up of two components: the long-term behaviour of the particle and overlaying short-period oscillations. The same can also be seen in Figure 2.3b, although the long-term (secular) effect does show a much more significant oscillation, while a seemingly remains constant on average over longer timescales. This secular evolution can be better examined for all orbital elements after isolating it from the smaller oscillations. These are introduced by the mean anomaly M, as the particle orbits the central body. By taking the time average over the mean anomaly, it is possible to average out these yearly short-period oscillations. Averaging M over one whole orbit is done – here with a as an example – in the following way:

$$\dot{a}(a, e, i, \omega, \Omega) = \frac{1}{2\pi} \int_0^{2\pi} \dot{a}(a, e, i, \omega, \Omega, M) dM. \tag{2.71}$$

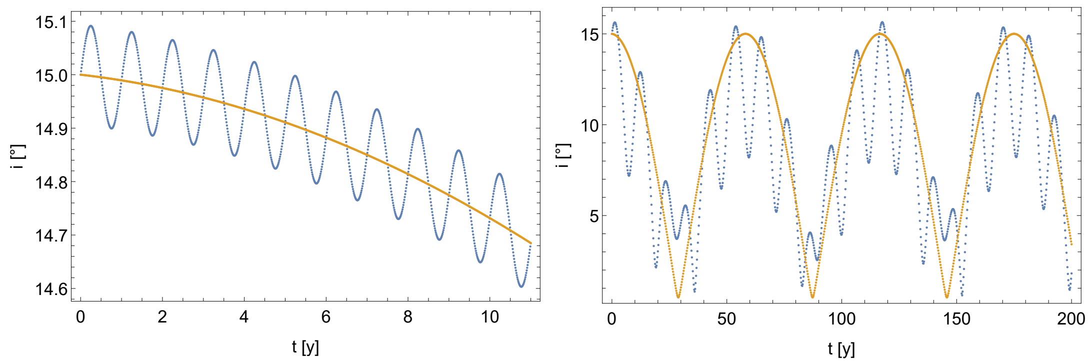

Figure 2.4.: Comparison of the secular evolution. On the left, the result shows the mean of the oscillations, on the right it represents the envelope.

However, as the expressions in the Gauss equations resulting from the series expansions (Appendix A) can become quite long for more complicated forces, it is not useful to do this integration because the computation could eventually take a very long time. In comparison, it is far simpler to equate the terms containing M to 0. This can be done as the mean anomaly only appears in sine and cosine terms, which yield 0 when averaging over one whole orbital period, since the average over trigonometric functions $f(M+2\pi) = f(M)$ is zero.

The six equations resulting from either utilising (2.71) for all orbital elements or the simpler equating of M-terms to zero now approximately represent the long-term evolution of the orbital elements of the particle. The caveat here is that this does not give accurate results (not shown here) when starting with an initial condition of $\omega = 0°$ as this proved to lead to a constant value in both ω and Ω at all times due to the term $sin(\omega)$ occurring in the Gauss equations of both Kepler elements, according to (2.63) and (2.62). This is not further a problem, as values very close to zero can be assigned to ω instead. Alternatively, it is of course also possible to begin the orbit outside of the perihelion and hence start with a true anomaly $\theta \neq 0$ to avoid the constant term in the Gauss equations. Considering that the focus of this thesis is to study particles originating from the Jupiter Trojans, the test object will typically be located at $M = 60°$ in most cases of the computations. Secondly, while the results match the general evolution fairly well, the values of the secular solution do not necessarily represent the mean values around which the complete solution oscillates, but possibly rather an enveloping oscillation, as is indicated in Figure 2.4. This is because the two methods technically integrate two different orbits without knowing the correlation between them, even though they both start with the same initial conditions for the orbital elements. However, these do not necessarily represent the mean values of each of the orbital elements, hence leading to slight differences in their average oscillation.

In conclusion, the Gauss equations can reproduce the dynamics of the full solution qualitatively well. While the expansion error in the angular parameters is larger compared to those in a, e and i, we see from Figure 2.3b that these largest deviations are typically outlier cases. Additionally, we have seen that the secular evolution in the orbital elements can be inferred from the results of the Gauss equations. Creating a model yielding those long-term changes – isolated from the short-period oscillations – for a charged particle in 1:1 mean motion resonance with Jupiter as it is affected by the interplanetary magnetic field is the focus of the next chapter.

3. Perturbations due to Jupiter and the Lorentz force

In the previous chapter, the basics for the integration of the unperturbed Kepler problem were examined, as well as the general effects on the orbital elements that occur when an additional perturbing force comes into play, with an example of a constant force term. Now, the next step is to see how the different forces in question affect the results, by including the influence of a planetary perturber and the solar magnetic field. Before implementing these two force terms, we will first take a look at the geometry of the dynamic system and discuss the unit conversion.

3.1. Unit and Coordinate System

In the course of the test simulation runs of a constant force term described in the previous section, we notice that, when working with SI-units, very small numbers (of the order of 10^{-16}) may occur initially in the equations of the orbital elements due to the form of equations (2.54), (2.57), (2.60) – (2.63), specifically due to the factor $1/\mu$. As they are later multiplied with the larger number of the initial condition for the semi-major axis when plugging in the values of the orbital elements, this is not further problematic when working with Mathematica. Some programs, however, work differently, and as the numbers are comparable to (or smaller than) typical machine precision, it may occur that the smallest numbers are equated to zero. In order to avoid this potential problem, a different unit system will be used in all following computations.

As shown in equation (2.22), the third Kepler law connects the semi-major axis of the particle, with its orbital angular velocity and the solar mass. Expressing the term on the right-hand side as $Gm_0 = \mu$ – as was first introduced for equation (2.35) – we find

$$n^2 a^3 = \mu, \tag{3.1}$$

which must be fulfilled for all unit systems and can therefore be used to derive the correct unit conversion. In place of SI-units, we will work with the base of larger quantities. This means that instead of using meter, the length unit is chosen in astronomical units [AU]. Instead of kilogram, the solar mass [$\mathrm{M}_\odot$] is used for the masses, and instead of seconds the sidereal year [yr] is used for the time. This results in a gravitational constant of the form $G = 39.478 \frac{\mathrm{AU}^3}{\mathrm{M}_\odot \mathrm{yr}^2}$. Together with the assumption that $m_0 = 1\mathrm{M}_\odot$, the mean motion of a particle placed at Earth's distance equates to $n = 2\pi/\mathrm{yr}$, according to (2.4).

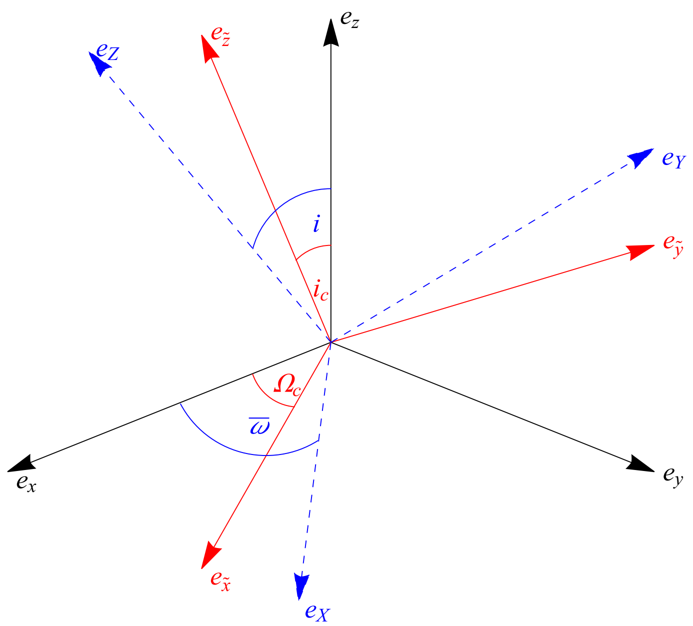

Figure 3.1.: An overview of the reference systems and their angles concerning the ecliptic plane (black) and the equatorial plane (red), as well as the orbital frame of the particle (dashed blue). The angle ϖ gives the longitude of the periapsis, the combined angle of $\omega + \Omega$.

We note that there are also other viable conversion options. For example, it is also possible to set μ to unity, while defining the length unit as [AU] and the mass as [$M_\odot$]. According to equations (3.1) and (2.4), however, this means that the time can no longer be defined by one sidereal year, but rather by 2π yr. Both types of unit systems are equally valid, and it is fairly simple to do a unit conversion between the two. It is only necessary to keep in mind the factor of 2π in cases where it does not cancel out.

The unit system of $(r, t, m) = ([\mathrm{AU}], [\mathrm{yr}], [\mathrm{M}_\odot])$ defines the values used in the following computations. Furthermore, it is also necessary to define the coordinate system in order to understand the geometry of the dynamical problem of a charged dust particle subjected to the influence of the interplanetary magnetic field as it moves in $1:1$ mean motion resonance with Jupiter. As described in Section 2.2, the frame of reference for the computations is the ecliptic frame with coordinates (x, y, z). Figure 2.1 has shown the difference in the orientation between the orbital system and the ecliptic frame. For the implementation of the Lorentz force, however, it is also necessary to include the orientation of the interplanetary magnetic field in the solar system. This introduces a dependence on the equatorial plane of the sun. A comparison between the three frames of reference is shown in Figure 3.1. As before, the coordinates (X, Y, Z) define the orbital system, while (x, y, z) define the ecliptic frame. Additionally, we also have $(\tilde{x}, \tilde{y}, \tilde{z})$, which represent the equatorial frame, in which $\tilde{z}$ is aligned with the solar rotation axis. We also note the appearance of the angles i_c and Ω_c between the equatorial system and the ecliptic frame of reference. These two angles as well as the full magnetic field model and orientation with respect to the equatorial reference frame will be explained in detail in Section 3.3.

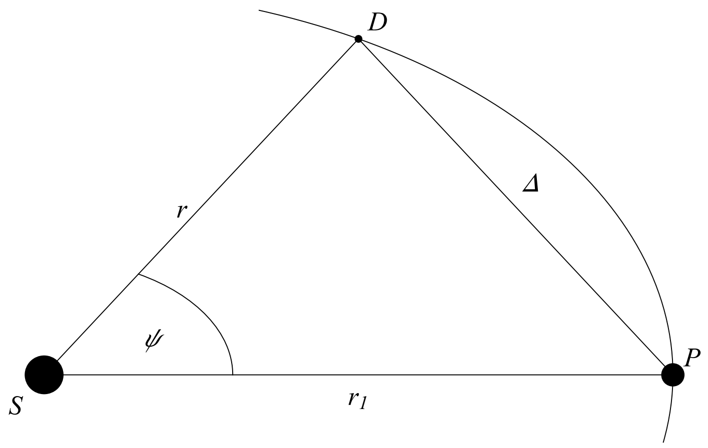

Figure 3.2.: ψ represents the angle between the two position vectors, Δ gives the distance between the position of the dust particle D and the planet P.

3.2. Planetary perturber

The next step is to place a Jupiter-like planet in the system currently containing only the central star and a dust particle, instead of including an arbitrary constant force term. For simplicity, the planet will move on a circular orbit within the ecliptic plane to avoid additional parameters in the calculations. For the position vector $\vec{r}_1$ of the perturbing body, this therefore yields

$$\vec{r}_1 = \begin{pmatrix} a_1 \cos M_1 \\ a_1 \sin M_1 \\ 0 \end{pmatrix}, \tag{3.2}$$

where a_1 and M_1 are the semi-major axis and the mean anomaly of the planet, respectively. With this approach, the planet's inclination i_1 and eccentricity e_1 do not need to be taken into account. In turn, this also means that ω_1 and Ω_1 of the planet are not defined, as already pointed out in Section 2.3.5. Figure 3.2 shows the position of Jupiter and the dust particle relative to each other and to the sun.

Similarly to the central star, the planet also influences the dust particle gravitationally. The potential energy in this case (see e.g. Lhotka and Celletti 2015) is written in the form of

$$\begin{aligned} U = -Gmm_1 \Bigg(& \frac{1}{((x-x_1)^2 + (y-y_1)^2 + (z-z_1))^{1/2}} && (3.3) \\ & - \frac{xx_1 + yy_1 + zz_1}{(x_1^2 + y_1^2 + z_1^2)^{3/2}} - \frac{1}{(x^2+y^2+z^2)^{1/2}} \Bigg), && (3.4) \end{aligned}$$

where the variables in $\vec{r} = (x, y, z)$ represent the coordinates of the dust particle as before, and the terms with subscript 1 represent the parameters of the planet. We notice that, originally, the term $\frac{1}{r}$ had been left out of (3.4). These first computations (not shown here), however, resulted in inaccurate results for the phase space (the parameter space discussed in detail in Section 3.2.3), which was corrected by including these terms.

The force term $\vec{F}_1$ of the planetary perturber results directly from the gradient of U, i.e. $\vec{F}_1 = -\nabla U$. This yields an additional external force (e.g. Lhotka and Galeş 2019; Murray and Dermott 2000) of

$$\vec{F}_1 = -Gm_1 \begin{pmatrix} \frac{x_1}{(x_1^2+y_1^2+z_1^2)^{3/2}} + \left(\frac{x-x_1}{((x-x_1)^2+(y-y_1)^2+(z-z_1)^2)^{3/2}}\right) \\ \frac{y_1}{(x_1^2+y_1^2+z_1^2)^{3/2}} + \left(\frac{y-y_1}{((x-x_1)^2+(y-y_1)^2+(z-z_1)^2)^{3/2}}\right) \\ \frac{z_1}{(x_1^2+y_1^2+z_1^2)^{3/2}} + \left(\frac{z-z_1}{((x-x_1)^2+(y-y_1)^2+(z-z_1)^2)^{3/2}}\right) \end{pmatrix}. \tag{3.5}$$

The solar gravity terms from (2.42) – (2.44) are modified by a reduction of the mass of Jupiter so that this equation contains the term $m_0 - m_1$[14]. This results from the inclusion of the term $\frac{1}{r}$ in (3.4), which was done in order to correct the frequency of the oscillation and to place the resulting orbits around the centre point in the phase space (Section 3.2.3).

Plugging (3.5) into the general equation of motion, i.e. (2.53), yields the Newtonian equations of motion for integration. For the Gauss equations, it is possible to insert the series expansions for the dust particle coordinates $\vec{r}$ (given in Appendix A) in (3.5) and to compute the cylindrical force components using (2.64) – (2.66). Those results can then in turn be used in the variation equations (2.54), (2.57), (2.60) – (2.63) to directly compute the orbital elements. We refer to this computation as the 'hybrid' approach. While this works, the resulting mixture of terms makes it difficult to isolate the system from the short-period oscillations to receive its dynamically relevant terms when studying the secular evolution, as was done in the previous chapter for the constant force term. Therefore, a different approach is needed.

3.2.1. Potential approximation

Instead of directly plugging the force term into the equations, it is also possible to start with an approximation of the potential U. To expand (3.4) into a series in small parameters ($\frac{a}{a_1} - 1$, e), the first and second term are treated separately, following the approach of Lhotka and Celletti 2015. Starting with the first term (referred to as $\frac{1}{\Delta}$), it is evident that it only depends on the distance between the two vectors $\vec{r}$ and $\vec{r}_1$. The denominator can be rewritten as $\|\vec{r} - \vec{r}_1\| = ((\vec{r} - \vec{r}_1)^2)^{1/2}$. Referring to the angle between the two vectors $\vec{r}$ and $\vec{r}_1$ as ψ (see Figure 3.2), and the length of $\vec{r}$ as r therefore yields

$$\frac{1}{\Delta} = \frac{1}{\sqrt{(x-x_1)^2 + (y-y_1)^2 + (z-z_1)^2}} = \frac{1}{\sqrt{r^2 + r_1^2 - 2rr_1 \cos\psi}}. \tag{3.6}$$

As we are studying the dynamical behaviour of dust particles in 1:1 resonance with a Jupiter-like planet, the difference between the vector lengths is only small, meaning that $r \sim r_1$. Hence, the value $\rho = \frac{r}{r_1} - 1$ is very small. Rearranging the terms of the previous equation and substituting r with $r_1(\rho + 1)$ and $2\cos\psi = 2 - A$ yields

[14] The values for the mass and the semi-major axis of the planet were taken from https://nssdc.gsfc.nasa.gov/planetary/factsheet/jupiterfact.html, last accessed on 07.06.2021.

$$\frac{1}{\sqrt{r^2 + r_1^2 - 2rr_1 \cos\psi}} = \frac{1}{r_1\sqrt{A}} \frac{1}{\sqrt{1+\rho+\frac{\rho^2}{A}}} = \frac{1}{r_1\sqrt{2}\sqrt{1-\cos\psi}} \frac{1}{\sqrt{1+\epsilon}}.$$

This is a useful representation of the terms, as both the expression $\frac{1}{\sqrt{1-\cos\psi}}$ and $\frac{1}{\sqrt{1+\epsilon}}$ can be written as an infinite series so that

$$\frac{1}{\sqrt{1-\cos\psi}} \frac{1}{\sqrt{1+\epsilon}} = \sum_{n=0}^{\infty}\sum_{m=0}^{\infty} (-1)^n \binom{-1/2}{n} (\cos\psi)^n \binom{-1/2}{m} \epsilon^n, \tag{3.7}$$

where $\epsilon = \rho + \frac{\rho^2}{2}$ is small, as explained before. For the approximation of the first term in the potential, we therefore already have two orders in the expansion, one in $cos(\psi)$ and one in ρ due to the form of the series.

Due to the geometry of the problem (compare Figure 3.2), the second term in (3.4) can simply be written as

$$\frac{\vec{r}\vec{r}_1}{r_1^3} = \frac{r\cos\psi}{r_1^2}, \tag{3.8}$$

which leads to an additional term in $\cos\psi$ in the expansion of the gradient (3.4). The last two equations combined with the $\frac{1}{r}$ term now yield an approximation for the potential energy of the perturber problem, that is exact only at the limit of $n, m \to \infty$ in ρ and $cos(\psi)$ but results in a good approximation already at lower orders, as well.

An additional order of approximation is introduced when computing the gradient of the potential and inserting the expressions for the series expansions in e of the dust coordinates $\vec{r}$, as was already done in the 'hybrid' approach with equation (3.5). Here, we have used a series expansion for the particle's coordinates, but not for the force terms themselves. This made it difficult to isolate the secular terms from the full expression.

However, to examine the long-term evolution of a dust particle influenced by a perturbing body which it lies in resonance with, the key parameter is the resonant angle Φ. This angle contains the mean longitude λ of both bodies, written as

$$\lambda = M + \omega + \Omega. \tag{3.9}$$

In terms of the simplified problem, in which the planet resides in the ecliptic plane and moves on a circular orbit (meaning that $\omega_1 = \Omega_1 = 0°$), the resonant angle (see for example Beauge 1994) reduces to

$$\Phi = \lambda - \lambda_1 = M + \omega + \Omega - M_1. \tag{3.10}$$

Integrating the terms in the Gauss equations containing (multiples of) this angle should suffice to study the long-term behaviour of the orbital elements of the particle. However, with the 'hybrid' approach of the Gaussian expressions, the M_1 terms are separated from the other angular parameters, making it difficult to isolate the terms containing Φ. As the goal of this thesis is to create a simplified mathematical model reduced to these terms, it is therefore preferable to perform the potential approximation despite the longer computation time.

The results of the potential approximation are used to calculate the cylindrical force components according to (2.64) – (2.66) and, with them, the Gauss equations (2.54), (2.57), and (2.60) – (2.63). The advantage of those terms, in comparison to the results of the shorter, much faster 'hybrid' approach for the Gauss model using (3.5) in (2.64) – (2.66), is that these expressions are easier to manipulate in order to combine the angular terms needed for the resonant angle into trigonometric expressions. Therefore, they are easier to isolate from the rest of the variables, making it possible to analyse the secular terms, i.e. those containing multiples of Φ.

3.2.2. Resonant terms

As already discussed in Section 2.5.2 for perturbed particle motion resulting from a constant force term, the high-frequency terms of the full solution do not alter the overall long-term evolution of the orbital elements. Hence, we can use methods similar to a frequency analysis in order to filter for the relevant frequencies – namely the ones containing (multiples of) the resonant angle Φ – and those only contributing to short-period oscillations. This, as pointed out previously, is facilitated by the expansion of the potential in which these terms can be combined more easily, as they are already summed up in the trigonometric expressions. This process is comparable to that of the example in Section 2.5.2, the difference being that instead of setting all terms containing M to zero, we set all terms which do not contain multiples of Φ to zero.

By isolating the system from these influences and keeping only the secular terms, it was found that (after some rearranging and combining of other terms) the resulting expressions for the Gaussian equations can each be rewritten in the form of a Fourier series:

$$\dot{a} = \sum_{k=0}^{K} \sum_{l=0}^{L} \sum_{m}^{M'} c_{klm}^{(a)}(e) \cos(ki) \sin(l\Phi + m\omega) \tag{3.11}$$

$$\dot{e} = \sum_{k=0}^{K} \sum_{l=0}^{L} \sum_{m}^{M'} c_{klm}^{(e)}(e) \cos(ki) \sin(l\Phi + m\omega) \tag{3.12}$$

$$\frac{\mathrm{d}i}{\mathrm{d}t} = \sum_{k=0}^{K} \sum_{l=0}^{L} \sum_{m}^{M'} c_{klm}^{(i)}(e) \sin(ki) \sin(l\Phi + m\omega) \tag{3.13}$$

$$\dot{\omega} = \sum_{k=0}^{K} \sum_{l=0}^{L} \sum_{m}^{M'} c_{klm}^{(\omega)}(e) \cos(ki) \cos(l\Phi + m\omega) \tag{3.14}$$

$$\dot{\Omega} = \sum_{k=0}^{K} \sum_{l=0}^{L} \sum_{m}^{M'} c_{klm}^{(\Omega)}(e) \cos(ki) \cos(l\Phi + m\omega) \tag{3.15}$$

$$\dot{M} = \sum_{k=0}^{K} \sum_{l=0}^{L} \sum_{m}^{M'} c_{klm}^{(M)}(e) \cos(ki) \cos(l\Phi + m\omega), \tag{3.16}$$

where the c terms are polynomials in e depending on the order to which the series is expanded (in this case $\mathcal{O}(e)^3$). The orders k and l depend on the order to which $cos(\psi)$ is expanded (in this case $\mathcal{O}(\cos\psi)^{13}$), while the order m appears only as either 0 or ± 2, making c zero in all other cases of m. We notice that all equations contain the factor $Gm_1\sqrt{a\mu}/\mu$ within their coefficients.

These expressions contain the dynamical information needed to study the secular evolution of the dust particles. It is therefore far more efficient to analyse these terms rather than computing the full result of the variation equations resulting from the potential approximation containing several thousand terms in total. All angular parameters apart from i vary with *cos*-terms of the resonant angle, while a, e and i do so with *sin*-terms. Additionally, the inclination appears to be the only orbital parameter oscillating with $sin(ki)$-terms. Lastly, an analysis of the full solutions (not give here) has shown that the c terms behave differently for the different Kepler elements. For the derivatives of a, i and Ω, the eccentricity appears with an even exponent (either 0 or 2), while in the equation of e itself it appears only in first order terms. In M and ω, no terms in e are found, which, as pointed out earlier, is due to the division by the eccentricity in their general equations in (2.60) and (2.63).

Figure 3.3 provides a comparison between the full Newton equations and these approximations of the resonant terms using the Gaussian variation equations. As can be seen here, the strongest deviation from the full solution is found in e and ω, which is possibly due to the truncation error of $\mathcal{O}(e)^3$. As can be inferred from the results, the error shows a link between these two orbital elements, as e decreases too fast, while ω increases to slowly. However, as the results do show a well enough agreement for the other parameters, these small deviations are accepted for the purpose of this study, as it does not focus on the evolution of e and ω, but rather on that of the inclination (and Ω), as will be seen in more detail in the course of Section 3.3.

3.2.3. Validation of the approximation

As pointed out in Section 3.2.1, the advantage of the potential approximation is that it is quite simple to combine the angular terms into trigonometric expressions, allowing to define the secular evolution of the dust particle by the equations (3.11) – (3.16). The disadvantage is that there are now three different expansion orders (in ρ and $cos(\psi)$ as well as e) in the model. All three add some approximation error into the result, which is why it is necessary to find a good balance in the orders of the three small parameters. This is also important in connection to the necessary computational time, as the number of terms for each of the Gaussian equations for higher orders, such as for the twelfth order in $cos(\psi)$ for example, is already around 1000.

After running several tests (not pictured here) with several combinations of the different orders, it appears that the expansion in the $cos(\psi)$ term is the dominant term that needs to be expanded to a higher order to minimize the error. This term induces a frequency shift in the angular variables leading to quite a strong difference in the periods. As the series technically contains an infinite number of frequencies, developing the series to small orders of course means that not all frequencies for an exact match are represented. Similarly, rewriting some of the $cos(\psi)$ terms of two small exponent values as an example, we find

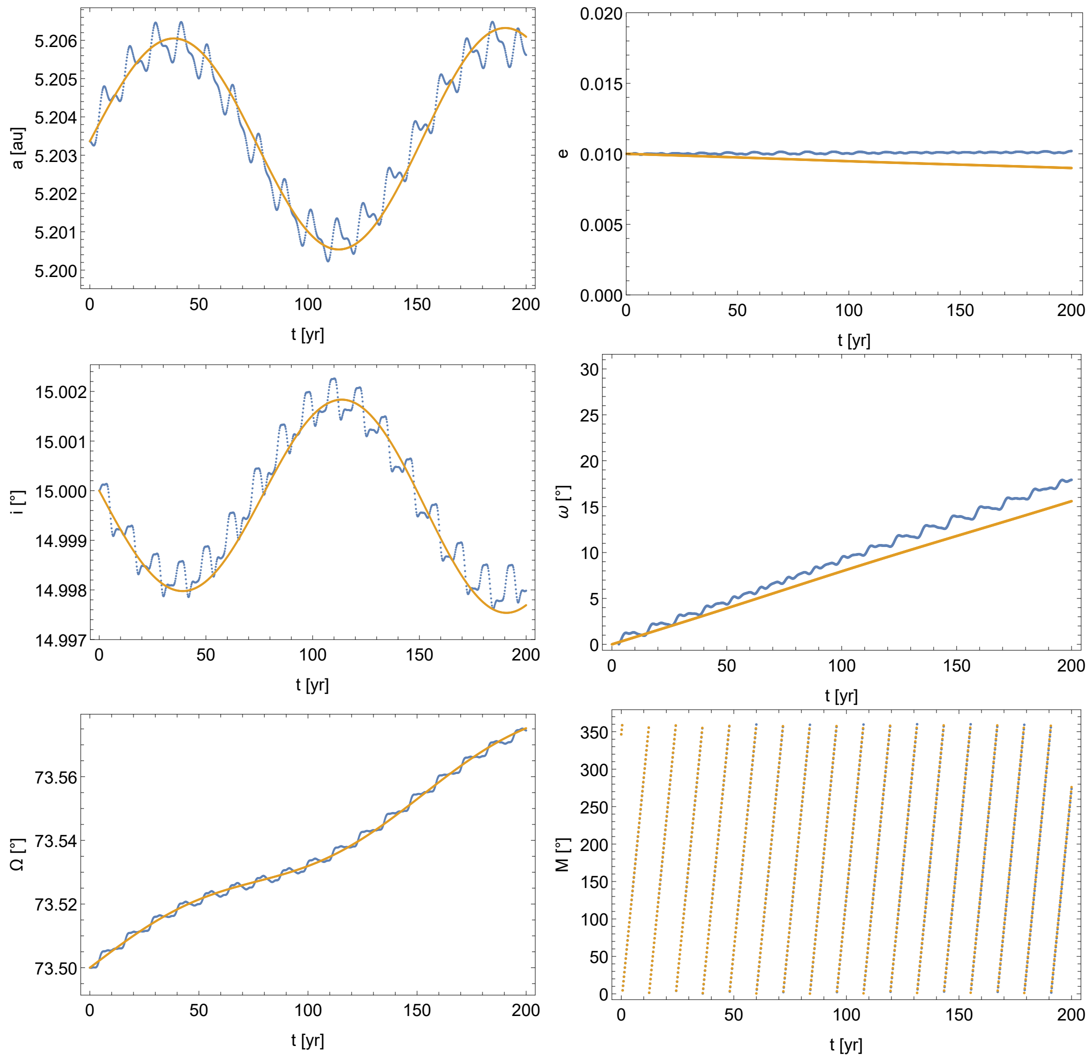

Figure 3.3.: Comparison of the evolution of the Kepler elements for the full Newtonian solution (blue) and the resonant Gaussian equations (yellow) for uncharged particles affected by a planetary perturber.

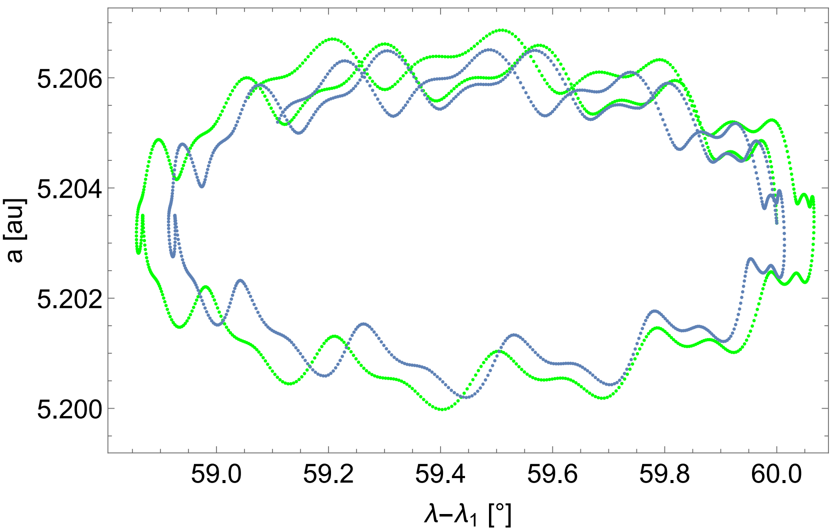

Figure 3.4.: Phase space diagram of the approximated Gaussian solution (green) and the full Newtonian solution (blue) for an integration time of 200 yr.

$$\cos\psi^2 = \frac{1}{2}(1+\cos 2\psi)$$
$$\cos\psi^4 = \frac{1}{8}(3+4\cos 2\psi+\cos 4\psi),$$

which shows that higher order terms in $cos(\psi)$ also contain lower frequency terms in multiples of ψ. This means that at small orders, there are also low-frequency terms missing. Changing to a higher order therefore results in an improvement of the fundamental frequency, leading to a better agreement in the results. In comparison, increasing the order in the term of $\frac{r}{r_1}-1$ does not yield a comparable improvement, instead a change in the order of this term becomes apparent only in the sixth or seventh decimal place.

Integrating over longer periods of time (not pictured here) has shown that while the result of the approximation of the potential is generally very good on short timescales, the agreement between this series expansion and the full Newton solution diminishes increasingly, especially in e and ω but also in the other orbital elements, as was the case for the constant force term in Section 2.5.2 because the numerical error in the integration adds up over time. The case for e and ω is already noticeable in Figure 3.3. In contrast to the results of the Newtonian equations of motion using (3.5) in (2.53), Figure 3.4 shows the deviations of Gauss approximation in both the semi-major axis and the resonant angle $\lambda-\lambda_1$ after some time, while the qualitative structure is preserved. The latter shows stronger deviations as the total error here is made up of the errors in ω, Ω and M. Additionally, as already mentioned in Section 2.5.2, the approximation error in the argument of perihelion and in the mean anomaly is also generally larger than in the other parameters, in this case for example in comparison to a, due to the form of the equations (divided by e). However, Figure 3.4 clearly shows that the qualitative shape of the orbit in the phase space is generally reproduced by the Gaussian solution, especially when looking at shorter timescales. It is also worth pointing out that the smallest errors occur for i

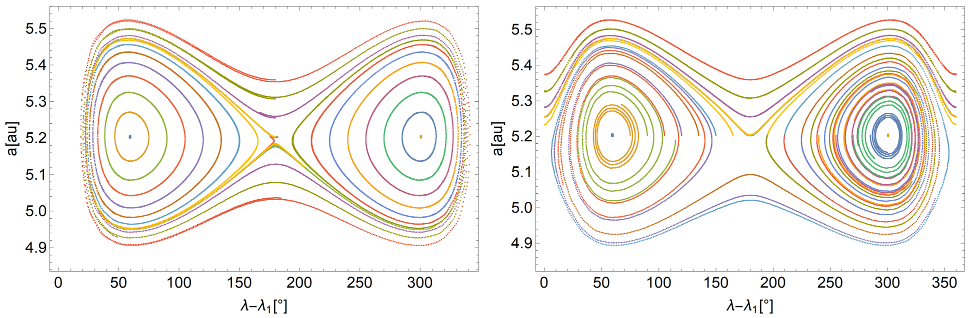

Figure 3.5.: Full phase space diagram of the full Newtonian solution (left) and the approximated resonant Gaussian solution (right).

and Ω (results not shown here), indicating that the representation of those two orbital elements via this approximation works quite well, which is important as studying the evolution of the inclination is the main goal of this thesis.

Additionally, results of further tests of the phase space using the simplified resonant model of (3.11) – (3.16) are given in Figure 3.5. This shows that the model can accurately reproduce different kinds of orbits (librational, rotational, tadpole, horseshoe orbits). However, it does not completely accurately represent the solutions farthest away from the equilibrium positions at the Lagrange points – i.e. 60° and 300° in $\Phi = \lambda - \lambda_1$ from equation (3.10). At later points in time, the solution at these points do not show closed lines, either. This indicates that the approximation works best near the equilibrium points but only on relatively short timescales of a few hundred years before the approximated motion deviates more strongly from the full numerical solution.

3.3. Lorentz force

The influence of the Lorentz force on the motion of charged particles is generally expressed as

$$\vec{F}_L = q\vec{E} + q(\vec{v} \times \vec{B}),$$

where q represents the charge of the particle, $\vec{v}$ its velocity, $\vec{E}$ the electric field vector and $\vec{B}$ the magnetic field vector. More specifically, in the case of the solar system, this equation is rewritten (as in Grün, Gustafson et al. 1994) to account for the solar wind so that with this velocity, $\vec{u}_{SW}$, we find

$$\vec{F}_L = q(\vec{v} - \vec{u}_{SW}) \times \vec{B}. \tag{3.17}$$

This can be done as the field lines of the interplanetary magnetic field are assumed to be carried outwards by the plasma motion, which is why it is also referred to as the ‘frozen-in’ magnetic field. According to Lhotka, Bourdin and Narita 2016, in combination with no background electric current resistivity, the electric field vector can be rewritten as $\vec{E} = -\vec{u}_{SW} \times \vec{B}$, resulting in (3.17).

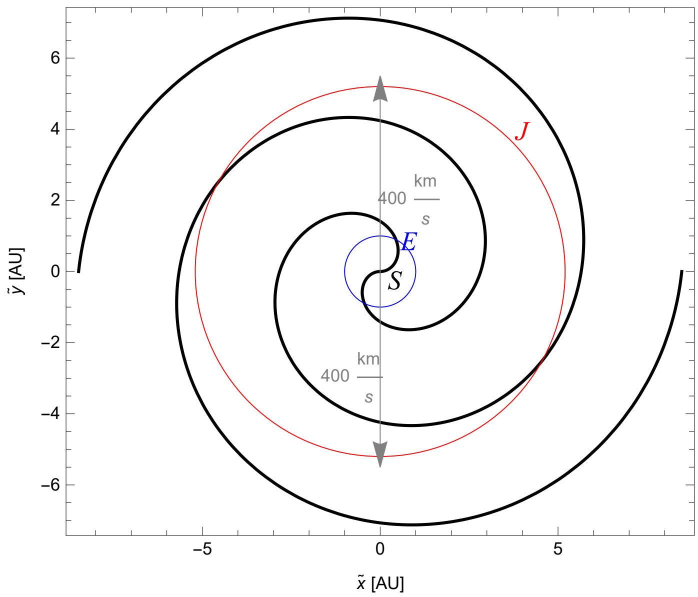

Figure 3.6.: Sketch of the shape of the Parker spiral for a solar wind speed of 400 km/s within the equatorial $(\tilde{x}, \tilde{y})$ plane (compare Figure 3.1).

The model for studying the influence of the solar magnetosphere on the orbital elements of a dust particle that is used here was originally derived in Lhotka and Galeş 2019 and includes the modified Parker spiral model given in Webb et al. 2010 taking after the original model by Parker 1958.

3.3.1. The Parker Spiral

In Parker 1958, the author suggested that the solar wind carries the magnetic field into the outer regions of the solar system. The assumption of a uniform, radially expanding solar wind yields for the velocity

$$\vec{u}_{SW} = u_{SW} \vec{e}_r.$$

For the magnetic field, this would hence lead to a radial configuration of the field lines. However, as the sun rotates, the radially stretched lines are wrapped into a spiral structure, as can be inferred from the sketch in Figure 3.6. The shape of this structure is also heavily influenced by the solar wind speed, as demonstrated in Lhotka and Narita 2019, as smaller wind speeds result in a more coiled up structure of the field lines.

The original Parker model did not take into account the polar component of the magnetic field, but only defined the radial and tangential component. Any normal component in the force term therefore vanishes. A more generalized approach for this model also includes the dipole structure of the magnetic field, meaning the sign of the magnetic field strength is different in regions above or below the solar equator (which has been incorporated into the model in Webb et al. 2010). This is explained in more detail for different approaches in Lhotka and Narita 2019.

Taking this structure into account furthermore leads to a connection of the rotation axis (i.e. the $\vec{e}_{\tilde{z}}$-axis in Figure 3.1) and the dipole axis via the so-called tilt angle. As the polarity at a given region in the solar system depends on the orientation of the magnetic equator relative to the sun's equator based on the solar rotation, the tilt angle would describe the angle between these two planes.

Additionally, the original Parker model assumes a time-independent magnetic field, which again only works as a rough approximation of the real dynamics. Most importantly, it neglects the effect of the solar cycle resulting in a polarity alteration within a period of 11 years and also in a variation of the tilt angle on shorter timescales, depending on the magnetic activity (see for example Smith, Tsurutani and Rosenberg 1978 and Jokipii and Thomas 1981). While it is possible to incorporate these effects into magnetic field models, this has not been done in the course of this work, as it solely focuses on studying the basic effects of the magnetic field on the evolution of the inclination of dust particles and on finding a mathematical model able to recreate the qualitative aspects of the problem. For this reason, the tilt angle is assumed to be zero in the following calculations (as in Figure 3.1), meaning that the magnetic field axis coincides with the rotational axis. Otherwise, an additional system of reference would need to be included to describe the orientation of the dipole structure.

The model of the interplanetary magnetic field in this work is written in the form of

$$\vec{B} = \frac{B_0 r_0^2}{r^2} \left(\frac{\vec{r}}{r} - \frac{\Omega_s}{u_{SW}} \vec{e}_{\tilde{z}} \times \vec{r} \right) \tanh \left(\frac{\alpha \vec{r} \vec{e}_{\tilde{z}}}{r} \right), \tag{3.18}$$

as in Lhotka and Galeş 2019. Here, the parameter B_0 represents the background magnetic field strength at a reference distance of r_0 (typically 1 AU), $\vec{r}$ gives the position vector of the particle orbit as before (again with $r = \|\vec{r}\|$), and Ω_s represents the rotation rate of the star. The latter can be written as $\Omega_s = \frac{2\pi}{24.47d}$, wherein d is given in days.[15] As already explained above, the vector $\vec{e}_{\tilde{z}}$ represents both the rotation axis of the sun and the dipole axis of the magnetic field in the case of this thesis.

In equation (3.18), α is not to be seen as a physical parameter but rather as a formal parameter to implement the sign change of the magnetic field at the solar equatorial plane. Therefore, it is related to a physical effect, i.e. the heliospheric current sheet, which is connected to the change in polarity, as it is the boundary separating the magnetic north and south. This is sketched in Figure 3.7, which also shows that larger values of α are necessary to correctly model the thin transition region. Strictly speaking, due to the solar rotation and the tilt of the magnetic field axis compared to the rotation axis in more realistic cases, the current sheet is not a flat structure but rather oscillates around the equator (see e.g. Smith 2001). Depending on the orientation of the magnetic axis with respect to the rotation axis of the sun, the oscillations of the current sheet within the equator can be quite large, leading to a so-called 'ballerina skirt' model (also discussed in Lhotka and Narita 2019). This is not further taken into account here, however, as the assumption for the equation is that the magnetic axis coincides with the rotation axis.

[15] For the sake of comparability, we note that for a unit system assuming $\mu = 1$, the factor of 2π in Ω_s cancels out during the day-to-time unit conversion (as the time is defined by 2π yr), while this is not the case for the assumption of $\mu = 39.478$ as is used in this work (see Section 3.1).

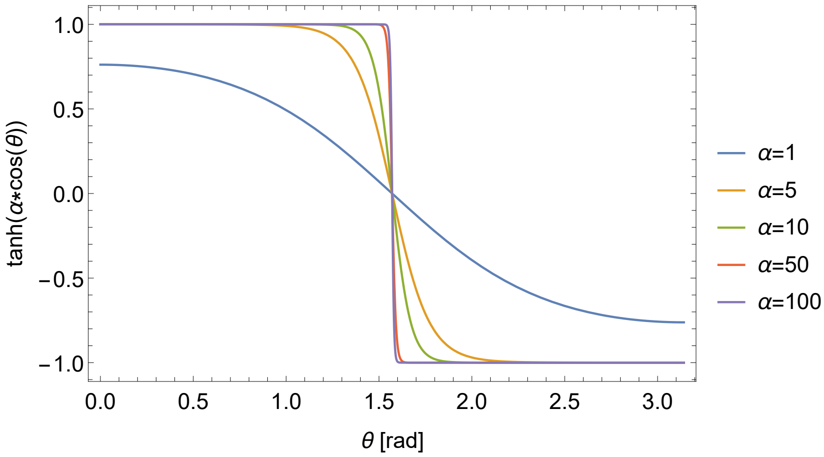

Figure 3.7.: The sign change as modelled by the *tanh*-function in equation (3.18) for different values of α. The term $\cos\theta$ results from the rotation of the z-vector. The graphic is reproduced from Figure 3 in Lhotka and Galeş 2019.

In order to implement the Lorentz force term into the equation of motion in (2.53), we now only need to insert (3.18) into (3.17) and to express the rotation axis vector $\vec{e}_{\tilde{z}}$ in terms of the ecliptic reference system.

3.3.2. Influence on particle motion

For the integration of the Newtonian equations of motion, Eq. 16 from Lhotka and Galeş 2019 was adopted in the form of

$$\vec{F}_L = -\frac{qB_0 r_0^2}{mr^2}\left(\frac{\vec{r}\times\dot{\vec{r}}}{r} + \frac{\Omega_s}{r}\vec{r}\times(\vec{r}\times\tilde{R}_{rot}\vec{e}_z) + \frac{\Omega_s}{u_{SW}}(\vec{r}\times\tilde{R}_{rot}\vec{e}_z)\times\dot{\vec{r}}\right)\tanh\left(\frac{\alpha\vec{r}\tilde{R}_{rot}\vec{e}_z}{r}\right), \tag{3.19}$$

where $\vec{e}_z$ gives the unit vector in the z-direction in the ecliptic reference frame in Cartesian coordinates and $\tilde{R}_{rot}$ corresponds to the rotation matrix of (2.34) for $\omega = 0°$ (compare Eq. (8) in Lhotka and Galeş 2019). Here the values for Ω and i in $\tilde{R}_{rot}$ are fixed to $\Omega_c = 73.5°$ and $i_c = 7.15°$, which are the so-called Carrington elements (after Carrington 1863) and specify the orientation of the rotation axis with respect to the ecliptic.[16] Ω_c gives the angle between the vernal equinox (which coincides with the x-axis of the ecliptic reference system) and the intersection of the solar equator and the ecliptic plane (the new $\tilde{x}$-axis). Similarly, i_c gives the angle between the z-axes of the ecliptic and the equatorial plane, not to be confused with the inclination i of the orbital plane of the dust particle. The values for these angles used here are taken from Beck and Giles 2005, who proposed these numbers from helioseismology

[16] For clarification purposes, the Carrington elements in this thesis are labelled with the subscript c, (i_c, Ω_c), in order to avoid any confusion between these two angles and the initial conditions for the inclination, i_0, and the longitude of the ascending node, Ω_0, in the course of this thesis. In the literature (as in Beck and Giles 2005 and Lhotka and Galeş 2019, for example), however, the Carrington elements are usually referred to as i_0 and Ω_0.

measurements. The rotation of the z-axis of the ecliptic reference systems around these values results in the vector $\vec{e}_{\tilde{z}}$ from (3.18). For comparison between the reference systems of the ecliptic, the equator and the orbital plane, as well as their particular angles, see Figure 3.1. It is because of the assumption that the solar rotation axis and the dipole axis coincide (i.e. the tilt angle between these two is zero) that it is possible to use the Carrington elements in these computations. Otherwise, different values would need to be used in the rotation matrix to account for the angle between the ecliptic z-axis and the dipole axis.

For the integration of equation (3.19) in the Newtonian equations of motion, it is assumed that $\alpha = 100$, as in Lhotka and Galeş 2019. This was done to ensure that the $tanh$-term resembles the Heaviside step function (as in Figure 3.7) in order to represent the sign change but to avoid the discontinuity. In terms of the physical effect, this models a rather thin heliospheric current sheet. Figure 3.7 also shows that smaller α values result in a much less steep decline, modelling a broader transition region between the magnetic north and south. The parameter q in equation (3.19) gives the charge of the dust particle. The charge itself can be calculated as

$$q = 4\pi\epsilon_0 UR, \tag{3.20}$$

where ϵ_0 is the dielectric constant in vacuum and U is the surface electric potential that a grain of radius R possesses. It is important to note from (3.19) that the Lorentz force not only depends on the charge but rather on the charge to mass ratio $\frac{q}{m}$, where m of course represents the mass of the dust particle, as before.

Equation (3.19) of the Lorentz force can now simply be implemented in (2.53) as the perturbing force $\vec{F}$, either by itself or also in addition to the perturbing force of the Jupiter-like planet. This integration (together with a set of initial conditions for $\vec{r}$ and $\dot{\vec{r}}$) again yields the complete numerical solution for the evolution of the orbital elements of the dust particles.

3.3.3. The secular dynamics

To examine directly the effect of the magnetic field on the orbital parameters, (3.19) needs to be converted into the cylindrical force components and plugged into the Gaussian equations of motion. As the main goal of this thesis is to study the mean effect of the Lorentz force on the inclination specifically, it is possible to adopt the results of Lhotka and Galeş 2019 into the computations. In this paper, the authors already calculated this average contribution and found that only the normal force component F_z (resulting from (2.66)) does not average out and hence leads to a secular effect on the Kepler elements. As can be inferred from the Gaussian equations, the Lorentz force should, therefore, mainly act on the inclination and the longitude of the ascending node, from (2.61) and (2.62), while the other elements can approximately be assumed to remain constant. This is roughly accurate for a and e, while ω does vary more significantly due to the influence of the normal force component in (2.63). This effect, however, is also roughly cancelled out on average and should not affect the evolution in i and Ω significantly.

The change on secular timescales for i and Ω is used here as it was derived in Lhotka and Galeş 2019 in the form of

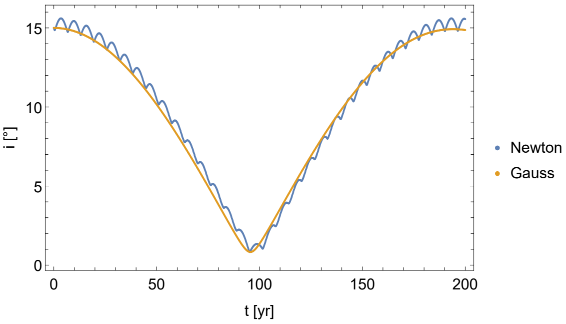

(a) Temporal evolution of i.

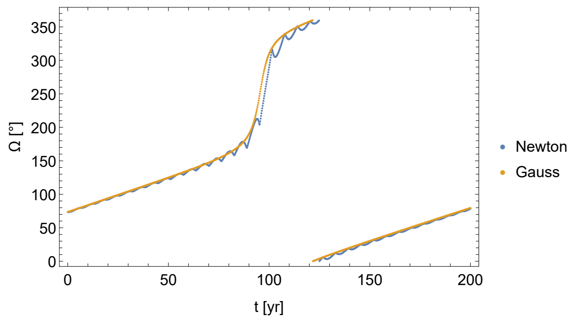

(b) Temporal evolution of Ω.

Figure 3.8.: An example for the comparison of the evolution in i and Ω for the full Newtonian solution and the Gaussian approximation of the influence of the Lorentz force.

$$\frac{\mathrm{d}i}{\mathrm{d}t} = -\alpha\frac{qB_0}{2m}\left(\frac{r_0}{a}\right)^2\left(\left(1 - z_0\cos i\frac{\Omega_s}{n}\right)(x_0\cos\Omega + y_0\sin\Omega)\right) \tag{3.21}$$

$$\begin{aligned}\frac{\mathrm{d}\Omega}{\mathrm{d}t} = -\alpha\frac{qB_0}{2m}\left(\frac{r_0}{a}\right)^2&\left(\left(\cot i - z_0\frac{\Omega_s\cos(2i)}{n\sin i}\right)(y_0\cos\Omega - x_0\sin\Omega)\right.\\ &\left.+\cos i(1-2z_0)\frac{\Omega_s}{n} + z_0\right).\end{aligned} \tag{3.22}$$

The parameters q, m, B_0, α, r_0, and Ω_s here are the same as before in (3.18) and (3.19), but we also see explicitly a dependence on the mean motion n. Additionally, there is an influence of the variables x_0, y_0 and z_0, which are simply the components of the vector resulting from $\tilde{R}_{rot}\vec{e}_z$ which appeared in the full equation (3.19). These vector components are therefore also connected to (i_c, Ω_c) and hence give the rotation axis in ecliptic coordinates.

The two equations above show the dependence of the amplitudes and frequencies of the variation in i and Ω on $\alpha\frac{q}{m}\frac{1}{a^2}$, so it depends on the distance to the star, the charge to mass ratio of the particle and α, which was the mathematical parameter used in (3.18) to model the polarity of the magnetic field. The reason for the direct proportionality to this parameter in contrast to a trigonometric relation as in the full equation for the Lorentz force is the simplification done in Lhotka and Galeş 2019 for the *tanh*-term (Eq. 21 in the paper). Here, the authors also point out the limitations of this approximation, namely that it can only be used for small eccentricities and inclinations, as well as small deviations of the magnetic axis (or alternatively in this case also of the rotation axis, i_c) from the z-axis of the ecliptic plane. Additionally, the above equations only contain the terms up to the first order in the $\tilde{R}_{rot}\vec{e}_z$ components and the eccentricity. Nevertheless, Figure 3.8 shows that the agreement between the Newton solution and the Gaussian approximation in i and Ω is very good.

The direct proportionality on α that results from the approximation leads to a difficulty in comparing the results to the full solution, in the sense that a value for the parameter different from that in the Newton equations has to be chosen here. Taking the same value of $\alpha = 100$ greatly overestimates the resulting variations in most cases. Hence, a different parametrisation of the current sheet is used in the Gaussian model to counteract the error resulting from the approximation of the *tanh*-term, as will be seen in the next chapter.

4. Parameter Study

Using equations (3.19), (3.21), and (3.22) from the previous chapter, it is now possible to study the secular evolution of dust particles in the inclination and the longitude of the ascending node under different initial conditions, i_0 and Ω_0, as well as different charge to mass ratios $\frac{q}{m}$. This is done to analyse the influence of the Lorentz force on these orbital elements in more detail and to see whether we find results for the inclination similar to those of the simulations in Liu and Schmidt 2018b. The results will allow drawing some tentative conclusions on the spatial distribution of the charged dust particles concerning their distribution near Jupiter, especially in regard to their ecliptic latitudes.

This chapter is split into several sections, starting with the general temporal evolution of the orbital elements and the parameter space they create, and how well it can be approximated by the secular model. Then, we focus on how different parameters in the equations modify this evolution. Lastly, we will focus on if and how these modifications change for different orbits, and which differences arise in the case with and without Jupiter. In the first few sections, the dust particles are located at the Lagrange point L4 (so for the resonant angle $\Phi = 60°$), later these results are also compared to those of a particle positioned at L5, moving on a horseshoe and tadpole orbit, as well as to an orbit located outside of resonance. Throughout the sections, comparisons between the full Newton solution – i.e. equation (2.53) with $\vec{F} = \vec{F}_1 + \vec{F}_L$ from (3.5) and (3.19), respectively – and the approximations for i and Ω using the averaged Gaussian equations – via a combination of (3.21) and (3.22) with (3.11) – (3.16) – are made to validate the model and to determine its strengths and weaknesses.

For the sake of comparability and to keep an overview over all of the variables, Table 4.1 shows the typical values used for each of the parameters and symbols. When varying one of the parameters, the others are always kept at the value assigned here unless explicitly stated otherwise within the text.

4.1. Validation of the model

Firstly, it is important to validate whether the simplified Gaussian model – comprised of equations (3.21) and (3.22) – can accurately reproduce the evolution of the inclination angle and the longitude of the ascending node. As already mentioned in Section 3.3.3, the parameter α adds some level of difficulty in the computation. The chosen value changes the curves (or, more specifically, their periods) resulting from (3.21) and (3.22) quite significantly, and it is not possible to use the same value as in the full equation here due to the approximation of the *tanh*-term. However, as will be explained in more detail in Section 4.4, the α value, which is necessary for fitting, can be calculated in a relatively simple process, once the variation frequency in i and Ω is known from the Newtonian solution. The form of this calculation was found after

Parameter	Value
B_0	3 nT
n	0.529 357 yr^{-1}
r_0	1 AU
R	2 µm
U	5 V
u_{SW}	400 000 m/s
x_0	0.119 342
y_0	−0.035 350 7
z_0	0.992 224
α_G	8
α_N	100
ϵ_0	$8.854\,187 \cdot 10^{-12}$ A s/(V m)
ρ	2.8 g/cm^3
Ω_s	93.7872 yr^{-1}
a_0	5.203 AU
e_0	0.01
i_0	1° to 20°
ω_0	0°
Ω_0	73.5°
M_0	346.5°

Table 4.1.: The values set for the different parameters (taken from Lhotka and Galeş 2019). If not specified otherwise, the parameters are kept constant to the values listed here for initialisation of the different simulation runs.

running several tests in order to automate the computation process. Initially, the adjustment was done by eye, by comparing the Gaussian solution to the full solution and varying α until the periods of both results were comparable. Figure 4.1 demonstrates the considerable agreement between the full Newtonian solution and the Gaussian model for different initial inclinations in the range of $i_0 = [1, 20]°$. In comparison, Figure 3.8 has shown the match for both orbital elements only for an $i_0 = 15°$. It is evident that the influence of the magnetic field leads to much stronger oscillations in i and Ω than what is found by just taking into account the effect of Jupiter, which was seen in Figure 3.3.

Although the approximation used in the model only accounts for the oscillations in i and Ω, Lhotka and Galeş 2019 have shown that the other orbital elements are largely unchanged by the Lorentz force on secular timescales. This is not as clearly the case for the argument of perihelion ω, as (2.63) shows the dependence of its evolution also on the normal component of the force terms, which does not average out for the Lorentz force. This does not pose a significant problem for the examinations here as the approximations for i and Ω do not include a significant dependence on the other Kepler elements aside from the small contribution of ω in the secular terms of the three-body problem, as equations (2.61) and (2.62) show. However, as Figure 3.3 has already demonstrated, the variations in i and Ω due to the influence of Jupiter are only small (of the order of 10^{-3} deg and 10^{-2} deg, respectively, although for Ω the effect does increase with time rather than oscillate, but it does so fairly slowly). Therefore, any deviations

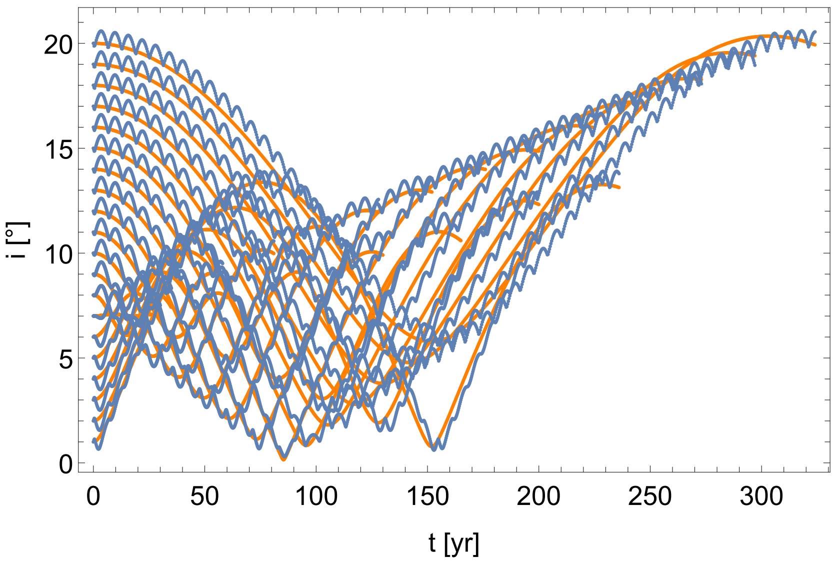

Figure 4.1.: The temporal evolution of different initial inclinations (from $i_0 = 1°$ to $i_0 = 20°$) with other parameters fixed as in Table 4.1 for Newton (blue) and Gauss (orange).

from the full Newtonian solution due to the missing ω in the approximation of the Lorentz force should not be very significant, especially during the first few hundred years, as Figure 3.8 (in comparison to Figure 3.3) shows a much stronger increase in both i and Ω due to the influence of the magnetic field. This is interesting to note because the deviation in ω from the full solution is quite significant in some cases, as was seen after some preliminary tests for different starting values in ω_0 (not pictured here). For $i_0 = 15°$, for example, ω passes through all possible values during one full period in i in the full solution, while it only shows a change of $5°$ in the model. Despite this deviation, the results in i and Ω are in a very good agreement. The comparison of the two computation approaches, as shown in Figure 3.8, indicate that the dynamics in this parameter space are most heavily influenced by the Lorentz force, as ω appears in neither of the equations (3.19), (3.21) nor (3.22).

Upon investigating the resulting Gaussian approximations in the other Kepler elements (not pictured here), it appears that in combination with the secular terms from the three-body problem, M is also mostly comparable to the full solution. It can hence be approximated with the given set of Gaussian equations (so seemingly being mostly affected by the influence of Jupiter), while for the other parameters the differences between the results of the two approaches – due to the addition of the Lorentz force terms into the full equation (3.19) and to neglecting their approximations in the secular model – are much greater. However, it also has to be pointed out that the deviation from the full solution with time does become more evident for the mean anomaly as well already after around 100 yr. So for this parameter, the Lorentz approximation further increases the problem of a greater mismatch on longer timescales already found from results of the potential approximation (compare Figure 3.4). Similarly, the model for i and Ω shows these deviations as well, but on slightly longer timescales of around 300 yr.

In conclusion, the secular model is able to qualitatively describe the evolution of the inclination and the longitude of the ascending node very well, despite including only the approximations in those two orbital elements.

4.2. Structure of the i-Ω-space

With the previous findings in mind, it is not preferable to demonstrate the results of this model in the phase space of a-Φ when comparing the full Newton solution and that of the resonant Gaussian equations (as was done before in Figure 3.5 for the case of just Jupiter) and studying the general effects on the dynamics due to the interplanetary magnetic field. As explained in Section 3.2.3, due to the expansion errors adding up over time, the Gaussian results cannot fully reproduce the curves in this phase space (especially not at larger distances from the equilibrium solutions). Additionally, as this simplified model for the Lorentz force does not take into account the evolution of all Kepler elements, and specifically not of ω, this means that the mean longitude λ of the dust particle cannot be calculated accurately, leading to a large difference in the a-Φ-phase space between the two simulation runs. Hence, it is better to study the results in the i-Ω-space, where the necessary equations are accounted for and the results generally display a good agreement between the two approaches (as shown in Figure 3.8), indicating a good representation of the dynamics in this parameter space.

For the representation of the results in the phase space, as seen in Figure 4.2, it is important to keep in mind that the temporal evolution cannot be directly inferred from it, as there is no longer a direct dependence on time in the graphic, as was the case in Figure 4.1, for example. However, this also means that the difference in the period of the oscillation in the Gaussian and the Newtonian solutions does not affect the general shape of the results in this parameter space, even without adjusting the α-value in the model. Furthermore, what can be inferred from this representation is any deviation leading to a change in the typical motions seen in Figure 4.2. Here, the orbits show distinct curves, which are repeated for every secular period cycle, resulting in the closed curves for the Newton solutions. Any possible deviation from that motion leads to a change in these curves. For example, this was seen when plotting the results of the Gaussian model for longer timescales, which is likely due to the combination of both the shrinking agreement between Newton and Gauss on longer timescales in the calculations of the third body potential (as explained in Section 3.2.3 and also as pointed out in the previous section) and approximation errors and limitations arising from the Lorentz model, as discussed in Section 3.3.3. These small shifts likely explain why the Gaussian curves do not close exactly after one full period, as can be seen in the upper left of Figure 4.2 near $\Omega_0 = 70°$. This Figure, however, does show that the general shape of the particle motion is very well represented by the Gaussian model nonetheless and that it can recreate the dominant features of this parameter space, which are induced by the influence of the magnetic field.

It is apparent from Figure 4.2 that there are two different regimes of motion for the dust particle depending on its initial location in the ecliptic coordinate system, which can be seen in both the full solution and the Gaussian results. Both librational[17] and rotational orbits are represented in the phase space diagram, in the broadest sense similar also to what is found in the a-Φ-space in Figure 3.5. At the centre of the librational orbits, there also appears to be an equilibrium point. No matter the initial inclination, the maximum value in i for all orbits – and hence also coinciding with the location of this equilibrium – is located at $\Omega = 73.5°$. This can not only be

[17] We note that the term 'librational' refers to the case of the osculating elements presented in most of the following sections. Strictly speaking, these orbits display a so-called 'paradoxal libration' (see e.g. Beaugé and Roig 2001), as we find rotational motion in the representation in proper elements (which will be discussed further in Section 4.6).

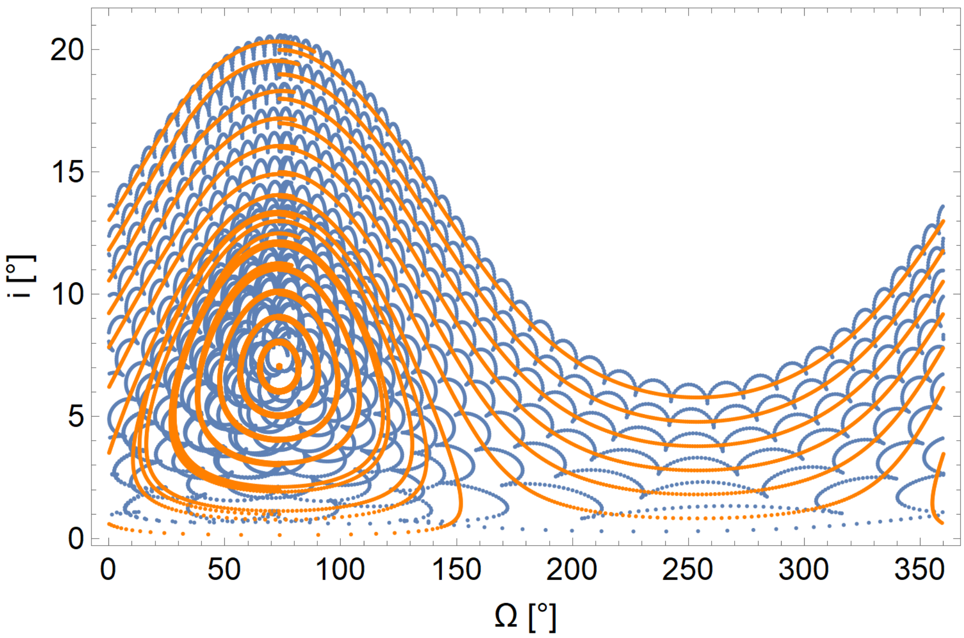

Figure 4.2.: The i-Ω-space for a fixed $\Omega_0 = 73.5°$ and a set of initial inclinations $i_0 = 1°$ to $20°$ for Newton (blue) and the Gaussian model (orange).

inferred from Figure 4.2 but also from (3.21) itself as well, by setting the equation to zero to locate the extrema and then solving for Ω, which yields

$$\tan \Omega = -\frac{x_0}{y_0}.$$

Using the values for x_0 and y_0 from Table 4.1, this yields $\Omega = 73.5°$ for the extremum. Interestingly, this value corresponds to the angle Ω_c, placing the particle's ascending node inside the heliospheric current sheet or, more specifically, aligning it with the node of the intersection line of the ecliptic and the solar equator (compare Figure 3.1), as the particle reaches its highest ecliptic latitude for all initial orbital inclinations.

It is therefore reasonable to assume that the equilibrium point for the Lorentz problem – somewhat similar to the Lagrange points in the a-Φ-phase space – is made up of the set $(i_0, \Omega_0) = (7.15°, 73.5°)$, initially placing the particle orbit within the equatorial plane of the sun and hence within the heliospheric current sheet. This also coincides with the results of Figure 4.2. Technically speaking, this feature in the parameter space is not a real equilibrium point per se, as the additional influence of Jupiter means that while (3.21) equates to zero at this position, the contribution of Jupiter does lead to deviations from that equilibrium. From Figure 4.2, it appears that these deviations are small in the Gaussian model, but the full solution does indicate slightly stronger oscillations. This is discussed further in Section 4.8, but due to the existing oscillations at the supposed equilibrium point, it is perhaps more accurate to refer to it as the minimum librational amplitude solution or simply minimum amplitude solution.

As L4 and L5 are located at $\Phi = 60°$ and $\Phi = 300°$, respectively, and the resonant angle is made up of the mean anomaly, the angle of perihelion and the longitude of the ascending node according to (3.10), it is possible to place the particle in the position of both a Lagrange point and to fulfil the Ω-condition of this (idealized) equilibrium condition of the Lorentz problem. We can achieve this by setting $\omega_0 = 0°$ and $M_0 = 60° - 73.5°$ for the simulations. This was done in the cases of the next few sections, when discussing the results for a particle initialized at the L4 position, as is also noted in Table 4.1. The reason for aligning the particle orbit in this way was to be able to study both the librational and the rotational orbits, as well as cases near the minimum amplitude solution. As Figure 4.2 shows, the latter is only possible when setting $\Omega_0 = 73.5°$. With this set-up, it was possible to investigate how the variations of different parameters influence these regimes of motion.

4.3. Period computation

As Figure 4.1 shows, the full solution of the variation in the inclination and the longitude of the ascending node is given by a superposition of a secular frequency and higher order harmonics. In order to compare the results of the parameter study described in detail in the following sections, we will first briefly depict the computation process of the periods and the amplitudes of the secular oscillations. As already discussed in Section 2.5.2, the dynamically relevant part of this study is the secular oscillation, which is also the part that the Gaussian model is able to reproduce. It is therefore also the frequency and amplitude of these oscillations that we will analyse further. In order to be able to validate the results of the following computations (which will be done in Section 4.11), two different methods were used to find the periods in the independent approaches of the full solution and of the secular model.

In the case of the Newton equations, an iterative function was used in order to locate the first two maxima in each oscillation. As has already been discussed in the previous section, the maximum in i always occurs when Ω reaches a value of 73.5°. It is therefore possible to integrate the Newton set of equation – i.e. equation (2.53) with $\vec{F} = \vec{F}_1 + \vec{F}_L$ from (3.5) and (3.19) – step by step and compute Ω for every time step. Each time, this value is then compared to Ω_c with some tolerance parameter ϵ, as depending on the size of the time step the exact value may not be reached. For the majority the computations, this value was set to $\epsilon = 3°$. If the value of Ω is comparable to the equilibrium condition in this way, the first maximum is found. The same process is repeated a second time in order to locate the second maximum for the computation of one full oscillation period. We note that the integration time for each individual run was therefore different, as every simulation was only run until one whole secular period cycle was completed.

It has to be kept in mind that in the case of librational orbits, Ω_c is also the value at which we find the minimum in the oscillation in i (compare Figure 4.2), as Ω no longer passes through all possible values in $[0, 360]°$. In these cases, it is therefore necessary to also compute the value in the inclination at each time step, i.e. $i(t)$, and compare it to the initial condition i_0. If $i(t) < i_0$ at the time step where $\Omega \sim \Omega_c$, a minimum has been located and the computation continues until it finds the maximum. Additionally, we note that this algorithm for locating the maxima in the oscillations in i does not function as well in the case of the minimum amplitude solution. Due to the deviation from the equilibrium position caused by Jupiter and then the occurrence of small oscillations slightly augmented by the magnetic field, the amplitudes in both i and Ω are small on the one hand. On the other hand, the oscillation is not of a periodic nature. The

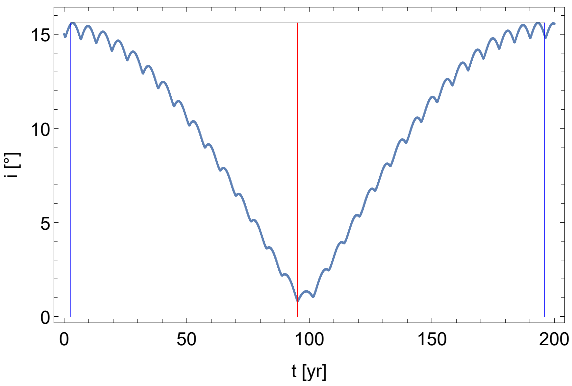

(a) Newton

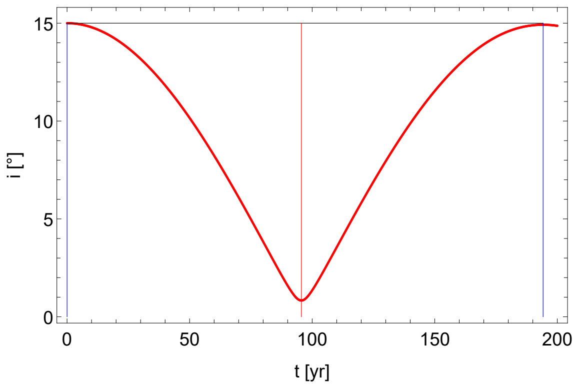

(b) Gauss

Figure 4.3.: An example of the results of the period computation for the Newtonian and the Gaussian case, where the red line marks the location of the minimum, the blue lines the first and second maximum and the overlying black line represents the period length.

algorithm to compute the period length can therefore not be used in this case. The behaviour of the minimum amplitude solution itself will be discussed in more detail in Section 4.8.

For the amplitudes of the secular oscillations, the results were found by simply picking out the maximum and minimum value in i within the integration range and subtracting them. Therefore, this calculation should not introduce any additional uncertainties into the results. However, it should be kept in mind that due to the iteration process, the computations only run up to the position of the second maximum, hence not taking into account any effects or deviations that may occur on longer timescales. It is possible that the maximum value increases slightly over time, for example. This was, however, not found when doing tests for individual cases on longer timescales (not shown here). The resulting parameters found by implementing this period function in the integration process are demonstrated in Figure 4.3a.

In the case of the simplified resonant model, the period was calculated by making use of a function already implemented in Mathematica, namely the `FindPeaks` function, which, as the name suggests, locates the largest values in a function. As it locates both local and global maxima, this function cannot as easily be used for the Newton results due to the additional higher order harmonics. For the smoother functions resulting from the Gaussian approximation, this does not pose a problem. In these cases, the Gaussian equations are integrated over a set period of time (here $T = 3000\,\mathrm{yr}$) and then the function is used to locate the peaks in i, which are given at the time step of the integration. After then matching these time steps to their actual values in years, the period is calculated by simply subtracting the second maximum position from the first. This is done as the Gaussian approximation deviates more from the Newton solution with time, and so it is likely that taking into account later maxima and averaging over the whole set of peaks found within a given timescale would not improve the results but rather falsify them, leading to larger differences between the Gaussian period and the Newton results.

The amplitude is calculated in the same way as before, by locating the minimum and maximum value over the whole interval and subtracting them from each other. The resulting uncertainties in the period are generally smaller than in the case of the Newton integrations due to the fact that there are no additional oscillations 'misplacing' the minimum position (compare its location in Figures 4.3a and 4.3b).

In order to quantify the uncertainty arising from the period calculation, the results in the period lengths of the following sections will be shown with error bars determined with the results indicated in Figure 4.3. As explained already, the main results of this algorithm are the time steps at which the first two maxima occur. With that, the period is taken as the time interval between these two extrema. The uncertainty σ is computed by determining the difference between the intervals of the first maximum t_1 to the minimum t_{min}, and the minimum to the second maximum t_2 in the following way:

$$\sigma = (t_2 - t_1)\left(1 - \frac{t_{min} - t_1}{t_2 - t_{min}}\right). \tag{4.1}$$

Sometimes, σ can be quite large, which, in some cases (typically for the results of the Newton approach), is related to the method of finding the minimum in connection to the higher harmonics and the shift in the minimum stemming from that. The position of the minimum is chosen by simply taking the smallest value from the interval up to the second maximum, so its position within the interval is not necessarily located midway between the two maxima, leading to larger uncertainties. An example of this is shown in Figure 4.3a.

With the methods of the period and amplitude computation in mind, the next sections will depict the results of the parameter study.

4.4. The role of the α parameter

As mentioned earlier, while α models a physical effect – the sign change of the magnetic field at the heliospheric current sheet (in this case coinciding with the solar equator) – the parameter itself is only a formal parameter. Therefore, it cannot be equated to a real physical value, making it difficult to fix it to a specific number.[18] There is still only little known about the specifics of the current sheet in particular, and the modelling of the function via the *tanh*-term only serves as an approximation under the assumption of a certain broadness of the current sheet determined by α (compare Figure 3.7). It is therefore important to be consistent in the use of this parameter. For the solution of the Newton equations using (3.19), a value of $\alpha_N = 100$ is adopted for the majority of the following computations (and has also been in the results discussed so far), while the results in the Gaussian equations for i and Ω are created by adjusting α_G to the value resulting in the best fit to the full solution. As pointed out in Section 4.1, the direct proportionality to α_G in (3.21) and (3.22) leads to limitations of the model and can induce a strong change in the frequency of i and Ω. This can lead to relatively

[18]This is generally difficult for most of the parameters in the equations, as many of them are only estimates on the actual values, for example for the particle density (which is assumed to be fixed to $\rho = 2.8\,\mathrm{g/cm^3}$ here, as in Lhotka and Galeş 2019), as well as for the surface electric potential U. This is due to the lack of observational data, in contrast to the difficulty in fixing α to a certain value, as it is not a physical, observable quantity at all.

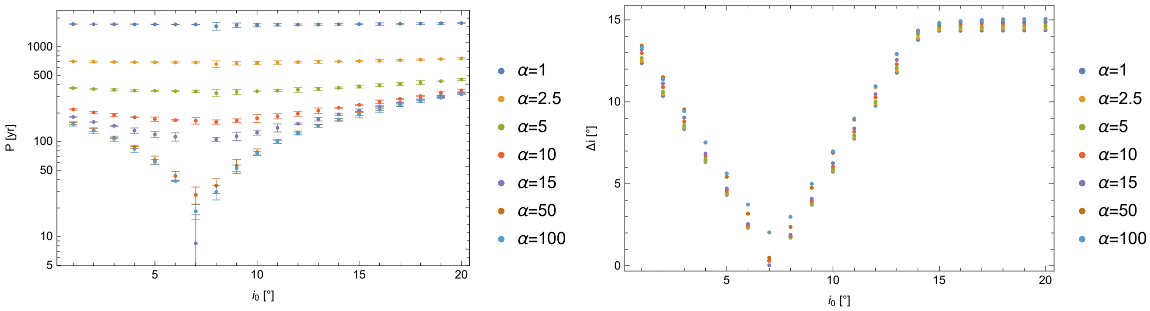

(a) Period to initial inclination.

(b) Amplitude with respect to i_0.

Figure 4.4.: Changes in the period and amplitude in the variation of the inclination for different values of α_N, modeling different sizes of the heliospheric current sheet.

strong temporal deviations from the full solution for an inappropriate value of the parameter. However, as both Figures 4.1 and 3.8 show, this is avoided with the correct choice of α_G.

After running several simulations and comparing the applied adjustments in α_G for different initial conditions (not pictured here), it was found that the value of α_G necessary in the resonant equations, best fitting to the Newton solution, can be found by first using an arbitrary value (for example $\alpha_G = 8$, as was done here) and then determining the periods P_{res} and P_{newt} for both solutions. By computing P_{res}/P_{newt} and multiplying the result to the initially chosen α_G, it is possible to fix the parameter to a fitting value in the resonant solutions. It is not an entirely exact solution to the problem, as it includes the uncertainty in the period computation from both the Newton case (as discussed in the previous section) and from the Gaussian model. Additionally, as the approximation error in the simplified resonant model adds up over time, the deviation in the period increases as well. These difficulties lead to the slight deviations from the Gaussian solutions seen in Figure 4.1 for some cases. However, the qualitative agreement between the two results is still very good, especially for the first hundred years, as has already been illustrated in Figure 3.8. It is also possible to do a simple adjustment of α_G by eye for a comparison between the two approaches, as was done initially. However, this impedes a fully automated calculation process. Instead it is much more practical to combine the two period computation algorithms from Section 4.3 in the way described above.

We generally fix $\alpha_N = 100$ for the Newton computations, in order to satisfy the approximation for a sign change function (as can be inferred from Figure 3.7, and as was done in Lhotka and Galeş 2019). However, it is still informative to look at the resulting change in the period and amplitudes of i and Ω for different values of this more technical parameter, and to see how it affects the results. They are provided in Figure 4.4. As explained earlier, the α term in the $\vec{B}$-model (3.18) approximates the sign change of the magnetic field at the solar equator by using the *tanh*-function. Smaller α values therefore may lead to a broader approximation of this region (as suggested by Figure 3.7). This is represented in Figure 4.4a, as for $\alpha = 1$ the periods are longest and roughly the same for all initial inclinations studied here. For such a broad current sheet, the orbits of all simulated particles within this i_0-range are likely placed inside the transition region, which might explain the uniformity in the period lengths. The oscillations show higher frequencies with increasing α_N (and therefore a narrower current sheet), as well as differences depending on i_0, which are discussed in more detail in Section 4.7.

The error bars in Figure 4.4a show the uncertainty arising from the period calculation. They were computed using equation (4.1). The majority of the uncertainties are quite small, and some larger ones can be explained by the effect of the shift of the minimum location due to the higher order harmonics, as explained in the previous section. In other cases, especially for $i_0 = 7°$, the larger σ value is due to the change in the shape and 'type' of the oscillation near the minimum amplitude solution, as has been mentioned earlier. This is discussed in more detail in the course of the next sections. Additionally, a more general discussion of the quantification of the errors arising from the period computation can be found in Section 4.11.

When looking at the resulting amplitudes in Figure 4.4b, we find typically larger values for larger α_N. The actual value, however, most strongly depends on the initial inclination and we see a clear V-shape in the results, with the smallest amplitudes found at $i_0 = 7°$, which of course corresponds to the minimum librational amplitude orbit being located at 7.15°. From this shape, the different regimes of motion in the i-Ω-space can also be inferred. As the amplitude values seem to 'saturate' at $i_0 = 14°$, this is likely the inclination around which the particle motion transitions from librational to rotational, as the particle orbit in the i-Ω-space is no longer restrained to a small oscillation in the orbital elements. For the longitude of the ascending node, this means that the orbital plane of the particle now passes through all possible values and therefore the orbit displays rotational behaviour rather than librational in the parameter space. This corresponds to the results of Figure 4.2, in which the rotational orbits are also seen for the cases of initial inclinations of 14° and upwards at $\Omega = 73.5°$.

Interestingly, the amplitudes in Figure 4.4b, while showing differences of up to 2° or 3°, are comparable in all cases of α, displaying the same features of librational and rotational behaviour found in the initial inclination range. This indicates that even for a broader current sheet a minimum amplitude solution is found, although it seems to show a longer secular period oscillation. Modelling a broader current sheet by diminishing the α value therefore leads to the same overall trend of the dynamics in the i-Ω-space but to a uniform frequency of the oscillations in all studied cases, as has been inferred from Figure 4.4a.

In conclusion, the α parameter in the full Newton solution, α_N, seemingly mostly affects the periods, and, in order to recreate the effect of a thin current sheet, the value is fixed to $\alpha_N = 100$. In the Gauss model, α_G also mostly affects the periods. It can be adjusted to specific values, to not only be able to model the slope (as well as the minimum and maximum) in the i-Ω-space but the temporal evolution of i and Ω, as well.

4.5. Particle size and surface electric potential

As in the previous case for the change in α_N, a change in both the particle size R and the surface electric potential U of the particle also leads to a change in the resulting frequency of the oscillation of the inclination and the longitude of the ascending node, as well as to differences in the amplitude. The two values U and R are combined in the charge to mass ratio $\frac{q}{m}$. (3.20) shows that the charge depends on both the surface potential and the size of the particle. Rewriting the mass also in terms of the particle radius (we assume spherical geometry for the dust grain) eventually yields for the charge to mass ratio

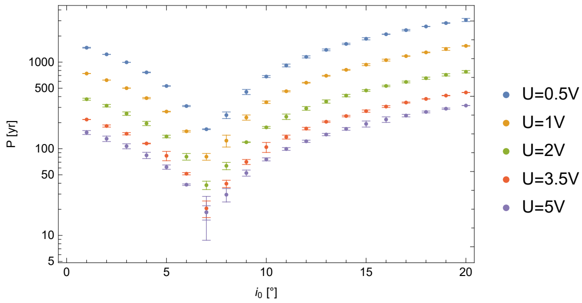

(a) Period to i_0

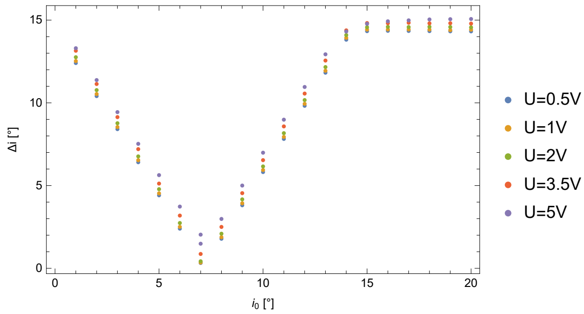

(b) Amplitude to i_0

Figure 4.5.: Period and amplitude of the evolution of i for different surface electric potentials U with a fixed particle size of $R = 2\,\mu\text{m}$.

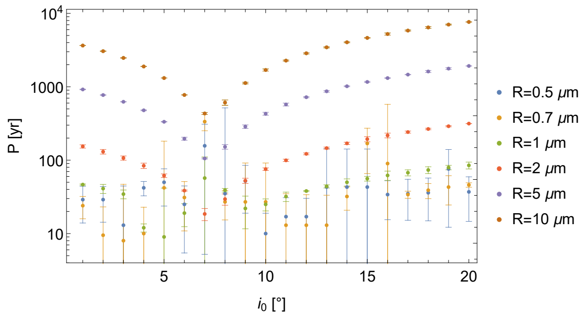

(a) Period to initial inclination

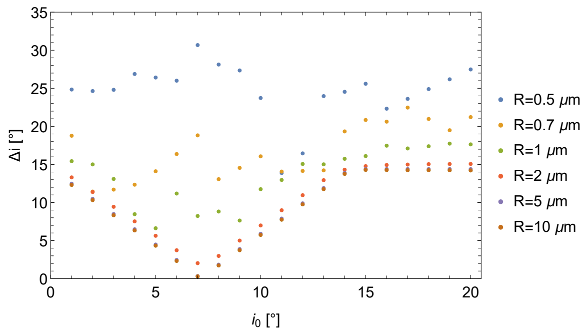

(b) Amplitude with respect to i_0

Figure 4.6.: Period and amplitude of the evolution of i with time for different particle sizes R with a fixed surface potential of $U = 5\,\text{V}$.

$$\frac{q}{m} = \frac{3\epsilon_0}{\rho}\frac{U}{R^2}, \tag{4.2}$$

in which the particle density ρ is assumed to be constant and fixed to the value in Table 4.1, as for ϵ_0. Changes in the charge to mass ratio therefore only depend on changes in either the surface potential of the particle or its size, making both parameters interesting candidates for further simulations.

As can be inferred from Figures 4.5a and 4.6a, showing the results of the U- and R-variation, respectively, larger charge to mass ratios generally lead to higher frequency oscillations for all studied initial inclinations. This is the expected outcome as the Lorentz force is proportional to $\frac{q}{m}$. Similarly, the runs with the largest charge to mass ratio also displayed the largest amplitudes in all cases of both Figures 4.5b and 4.6b. As described in Section 4.3, the amplitudes were again computed by subtracting the minimum from the maximum value in i within the individual integrated intervals. The dispersion in the results of the same initial inclination is largest in the case of $i_0 = 7°$. For the larger values of i_0 from around $i_0 = 14°$ onwards (at which point the amplitudes seem to saturate and we again find rotational orbits, as is the case in Figure 4.2), the spread in the amplitudes is smaller and roughly the same for all surface potential values in

Figure 4.5b. This indicates that a moderate change in U affects the librational orbits slightly more.

This is not the case, however, for all different particle radii studied in Figure 4.6. It was found that there is a minimum particle radius, below which the period computation is no longer accurately feasible, as the oscillation of the particle is no longer of a periodic nature. This minimum radius is found to be at around 1 µm. Alternatively speaking, dust particles with sizes of more than 1 µm display discernible long-period oscillations (a clearly distinguishable secular frequency with smaller superimposed higher harmonics). Therefore, these dust grains show a temporal regularity in their i variation (and hence in their spatial distribution along the ecliptic latitude). Smaller particles, which are more strongly influenced by the Lorentz force, do not. This can be inferred from Figure 4.6a. Evidently, the smallest particles show none of the regularity in the period that was found in the previous discussion for the case of variations of α and also of U. This is the reason for the larger error bars seen in Figure 4.6a in the cases of particles of $R \leq 1\,\mu\text{m}$. A possible explanation is that there are no longer any long-period oscillations to determine. We notice that the emergence of the patterns in amplitude and period for different initial inclinations obtained around the equilibrium solution is only really found accurately for particle sizes of around 2 µm and larger.

Most interesting perhaps is the fact that the minimum amplitude solution previously seen in all cases is seemingly not found for the case of the smallest particles, which is inferred from Figure 4.6b. Both the 0.5 µm and the 0.7 µm objects display their largest amplitudes in i in the case of the $i_0 = 7°$ run. However, upon taking a closer look at the temporal evolution resulting from these cases, it has been found that for the first few time steps, the particles do remain in somewhat of an equilibrium state, or at least represent what would be expected from a minimum amplitude solution. This state, however, is disrupted very quickly and the strong influence of the Lorentz force (likely in combination with a 'nudge' from Jupiter) leads to these large oscillations. Possible explanations and implications of this are discussed in Sections 4.9 and 4.10, as well as in the next chapter.

The simplified Gaussian model for the resonant terms can also no longer correctly reproduce the results of the full solution in the cases of $R \leq 1\,\mu\text{m}$. For smaller radii, the Lorentz force strongly dominates the evolution of the inclination and the longitude of the ascending node[19]. However, as the Gaussian equations are grounded in the assumption that the objects move on perturbed Keplerian orbits, meaning that the gravitational force is assumed to be the dominating factor while the objects are only further affected by some less significant additional perturbing forces, this means that these equations cannot yield the correct results anymore once this assumption is no longer fulfilled. For smaller particles, it would therefore be necessary to change the initial approach for the Gaussian equations to that of particles moving in a magnetic field where gravity would introduce an additional perturbation, rather than the other way around. This approach may be worth further investigation in the future. For particle sizes down to roughly 1 µm, the model can still mostly reproduce the maximum values resulting in the inclination for the rotational orbits, even though it cannot replicate the exact shape of the variations. For the librational orbits, the oscillations show a much stronger deviation from their periodic variation at smaller sizes, already at around 1 µm, where the model can no longer give a good enough approximation of the amplitude but rather yields much smaller values. In this case, the Gaussian model yields periodic oscillations for all R, which is no longer in agreement with the

[19] Compare also Figure 1 in Lhotka and Galeş 2019.

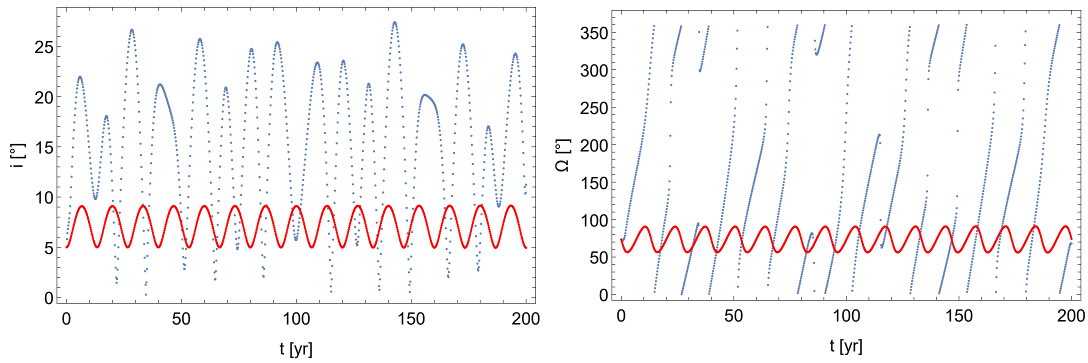

(a) Comparison in i.

(b) Comparison in Ω.

Figure 4.7.: Comparison of the Newtonian solution (blue) and the Gaussian model (red) in i and Ω for $R = 0.5\,\mu\text{m}$ and a fixed surface potential of $5\,\text{V}$.

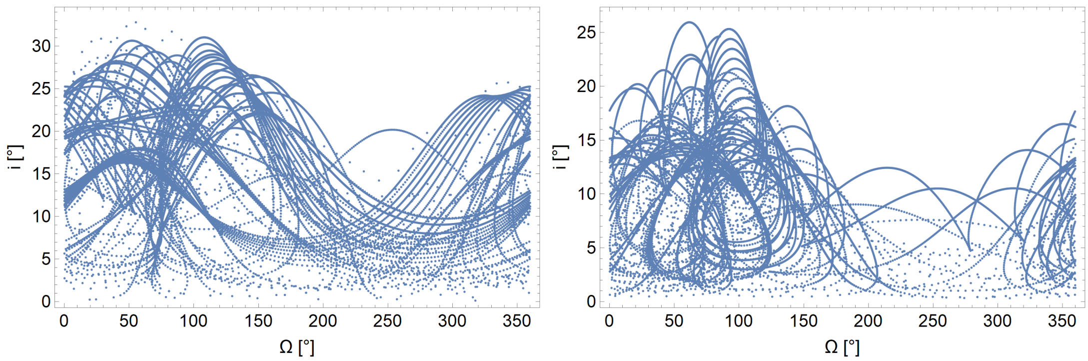

(a) $R = 0.5\,\mu\text{m}$

(b) $R = 0.7\,\mu\text{m}$

Figure 4.8.: Phase space diagram in i and Ω for the smallest studied particle sizes with a fixed surface potential of $5\,\text{V}$.

full solution for the smaller radii, as is evidently seen in Figure 4.7 for the case of the smallest particle size studied here. This means that the minimum particle radius for the evaluation of the secular period also corresponds to a lower limit for the application of the Gaussian model.

As both the particle size and the surface electric potential influence the charge to mass ratio, this limitation in the radius of a minimum of $2\,\mu\text{m}$ can also be seen as an upper limit on the charge to mass ratio itself to a value of around $\frac{q}{m} = 0.0119\,\text{C/kg}$ (as the computations here are done with the assumption of $U = 5\,\text{V}$, when varying the other parameters). For larger values, the structure in the i-Ω-space (i.e. Figure 4.2) is no longer found as clearly as before. In the case of the $0.7\,\mu\text{m}$ particle, it is still possible to discern some librational behaviour but this is no longer the case of particles with sizes of $0.5\,\mu\text{m}$, as can be inferred upon comparing Figures 4.8a and 4.8b.

On the other hand, larger particle sizes (or a smaller surface potential) lead to smaller charge to mass ratios – so to a weaker influence of the Lorentz force – as equation (4.2) shows. This in turn leads to much lower frequencies, as was already seen in both Figures 4.5a and 4.6a. Here, we find a difference of one order of magnitude in the former between charge to mass ratios of $0.0012\,\text{C/kg}$ and $0.0119\,\text{C/kg}$ (so the difference in the period scales directly to the difference

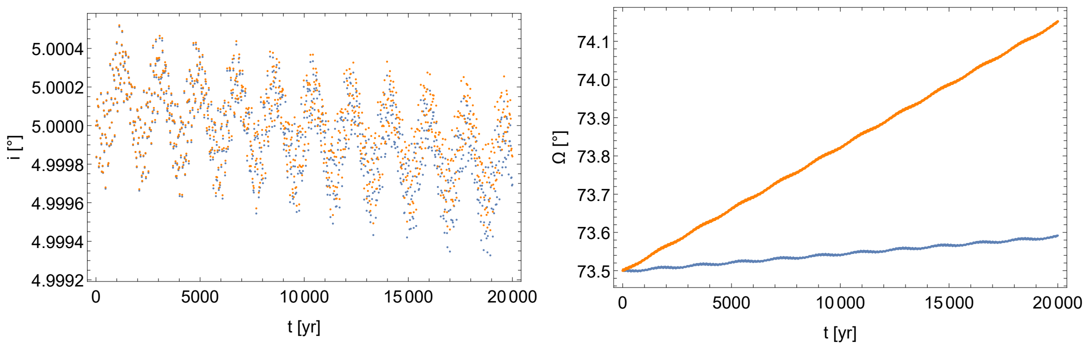

(a) Comparison in the inclination.

(b) Comparison in Ω.

Figure 4.9.: Comparison of the solution including the Lorentz force (with $U = 5\,\mathrm{V}$ and $R = 650\,\mu\mathrm{m}$, blue line) and the solution for $U = 0\,\mathrm{V}$ (orange) in i and Ω.

in the ratio), and even slightly larger values for the case of $\frac{q}{m} = 0.000\,47\,\mathrm{C/kg}$. These smaller charge to mass ratios hence also display a much shallower initial increase in the inclination. This already becomes noticeable for particle sizes of around $5\,\mu\mathrm{m}$ but especially so for radii of more than $10\,\mu\mathrm{m}$. For particle sizes of more than $603\,\mu\mathrm{m}$, the resulting i and Ω eventually start to resemble those in the systems with no Lorentz force, as has been found after running several tests of different R. In order to place some constraint on the particle radius up to which the influence of the magnetic field dominates, we simulated the particle dynamics (with the Newton approach) by starting with the case of both a smaller and larger R. Then, we continuously shortened the size difference of that interval to locate where a noticeable change in the behaviour of i and Ω occurs. A particle radius of $R = 603\,\mathrm{nm}$ is where the change in Ω becomes similar to the slope of the case where $U = 0\,\mathrm{V}$ (and hence shows a similar slope as in Figure 3.3), as was studied for the case of one of the librational orbits. For particles with an $i_0 = 5°$, the slope in Ω changes from descending to ascending at around this particle size, indicating that the dynamics in the i-Ω-space likely lose their structure and features found in Figure 4.2, which are induced by the interplanetary magnetic field.

An example of the comparison of a case with large particle sizes to the case with no influence of the Lorentz force at all can be seen in Figure 4.9, for both the change in i and the slope in Ω. For this Figure, a particle size of $R = 650\,\mu\mathrm{m}$ was used to demonstrate that the behaviour of the inclination is already roughly similar to that of the uncharged case, while Ω does show a greater deviation from the case with no magnetic field still for such large particle sizes. This deviation is of course further reduced by gradually increasing the radius of the object.

At sizes of more than $10\,\mu\mathrm{m}$, the integration time already needs to be much longer to be able to discern the different regimes of motion, as the frequencies of the oscillations are so much lower in comparison to the smaller particles. To determine the loss of the librational behaviour, the integration time was set to $90\,000\,\mathrm{yr}$. The resulting solution in the i-Ω-space (not pictured here) did not resemble a discernible pattern, but rather just an accumulation of data points around roughly the same value, as would be expected from Figure 4.9.

In conclusion, we have found that a change in the charge to mass ratio most strongly leads to a change in the period of the oscillation in i and Ω, with longer periods for smaller charge to mass ratios. The amplitudes, on the other hand, remain roughly the same up until a value of around

$\frac{q}{m} = 0.0119\,\mathrm{C/kg}$, or a minimum particle radius of $2\,\mu\mathrm{m}$. For smaller particles – i.e. larger charge to mass ratios – the structure in the i-Ω-space becomes more chaotic. We also note that the Gaussian model can only be applied to dust grains with $R > 1\,\mu\mathrm{m}$. Placing an upper limit on the particle radius, at which point the i-Ω-structure changes and is no longer dominated by the influence of the magnetic field, is difficult due to the long integration times necessary. It is beneficial to take a different approach by transforming the results into the proper elements space.

4.6. Proper elements space

Another representation of the Kepler elements can be done in action-angle variables (derived from the secular Hamiltonian), the so-called proper elements. These stand in contrast to the typically used orbital elements in the expressions so far, which are also referred to as the 'osculating' elements. As explained in Section 8.3 of Morbidelli 2002, the osculating elements vary strongly due to perturbations of the body caused by external forces, while the proper elements – in ideal circumstances – are constants of motion. In a realistic system, with several forces perturbing particle motion, this is not exactly the case (due to the averaging processes, e.g. Lemaitre 1993), either. However, the variation in these elements are smaller in amplitude than in the osculating elements, allowing them to be considered quasi-constants.

For most astronomical purposes, the studied proper elements space is composed of the eccentricity and the longitude of perihelion ϖ (see e.g. Murray and Dermott 2000) in the form of

$$h = e \sin \varpi \tag{4.3}$$
$$k = e \cos \varpi . \tag{4.4}$$

As the focus of this study, however, lies on the evolution of the inclination and the longitude of the ascending node without exact computation of e and ϖ in the Gaussian model, another set of equations must be used. These are written as

$$p = \sin\left(\frac{i}{2}\right) \sin \Omega \tag{4.5}$$
$$q = \sin\left(\frac{i}{2}\right) \cos \Omega . \tag{4.6}$$

For each set of (i_0, Ω_0), these equations form a circular motion in the p-q-space, with an approximately constant proper radius i_p and proper frequency $\Omega_{p,f}$ in comparison to the stronger oscillations in the osculating i and Ω.

Equations (4.3) – (4.6) are derived from the Lagrange planetary equations. In contrast to the Gauss equations, the Lagrange equations are formed from a so-called disturbing function in the equation of motion, an additional term in (2.3). This function contains all perturbations affecting the body. For more details on the derivations see Appendix B in Fitzpatrick 2012

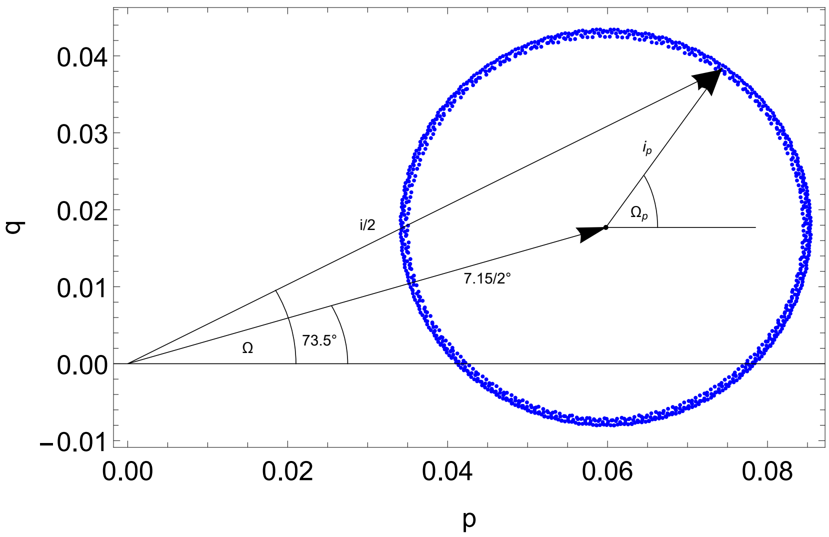

Figure 4.10.: Representation of an orbit in the p-q-space, and a depiction of the meaning of i_p and Ω_p in contrast to the osculating elements i and Ω.

(based on the work of Brouwer and Clemence 1961). The resulting equations for the orbital elements have a limitation in that representation, as small values of e and i result in a singularity in some cases. The definitions of the alternate orbital elements h, k, p and q are used to avoid that.

As described in Chapter 7 of Murray and Dermott 2000, the equations of motion of a body of negligible mass on a perturbed Keplerian orbit can also be written in the form of $\dot{h}$, $\dot{k}$, $\dot{p}$ and $\dot{q}$. This can be done in the case of secular theory, i.e. with the so-called Laplace-Lagrange secular solution. These result in differential equations, for which boundary conditions are needed. The parameters resulting from those conditions are referred to as the proper elements. The comparison in the proper elements space between them and the osculating elements can be seen in Figure 4.10[20]. Evidently, the variable i_p remains nearly constant, while i shows much greater oscillations. Additionally, Ω_p oscillates between $[0, 360]^\circ$, while Ω does not in the case of this orbit. The parameters for the orbit pictured in Figure 4.10 were set to $R = 5\,\mu\text{m}$ (so that we have smaller amplitudes in the higher order harmonics to better demonstrate i_p) and $i_0 = 10°$. The rest of the parameters are the same as in Table 4.1.

Finding a suitable upper limit for the particle size with the results in i and Ω so far has proven to be quite an ambiguous matter, as has been seen in the previous section. As will be seen, it is far easier to place constraints on that account by going into the proper element space. By studying the effect of varying particle size on i_p and $\Omega_{p,f}$, some more precise constraints can be placed on the influence of the interplanetary magnetic field on larger particles.

Firstly, in order to simplify the analysis of the results, the proper elements orbit for the different initial conditions in (i, Ω) was always positioned around the origin of the proper elements space

[20] Compare also Figure 7.3 in Murray and Dermott 2000, in which the authors show the proper elements space in p and q for a particle only affected by a planetary perturber. The biggest difference in these two cases is the displacement vector to the centre of the orbits (i.e. i_{forced} and Ω_{forced} in that Figure). In our case, this vector depends on the heliospheric current sheet, while in Murray and Dermott 2000, it depends only on the planet's properties.

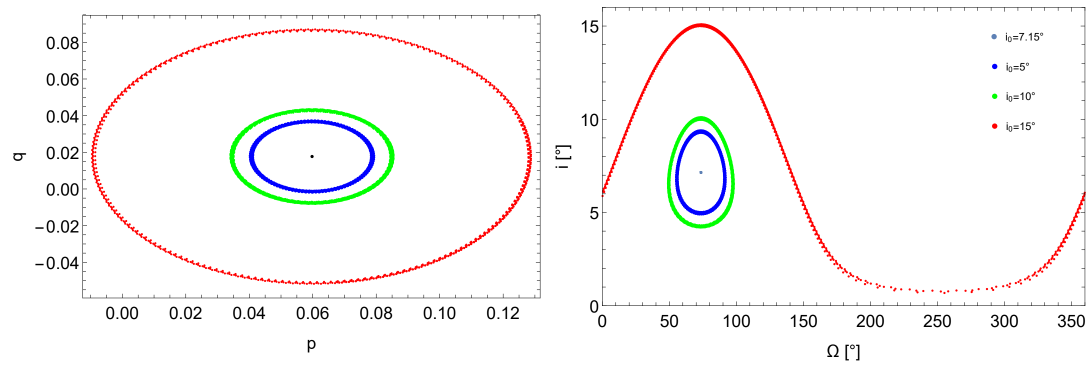

(a) Proper elements

(b) Osculating elements

Figure 4.11.: Comparison of four different orbits in proper elements space and in the osculating i-Ω-space. Evidently, the representation of both the rotational and librational orbits resembles a circular motion around the minimum amplitude orbit in p-q-space.

by subtracting the minimum amplitude solution (i.e. by correcting the displacement seen in Figure 4.10). This can be done because in the proper elements space, all types of orbits are represented as a circulation and are collocated around the minimum amplitude solution, as is indicated in Figure 4.11. By placing it in the center of the coordinate system according to

$$\begin{pmatrix} p \\ q \end{pmatrix} = \sin\left(\frac{i}{2}\right)\begin{pmatrix} \sin\Omega \\ \cos\Omega \end{pmatrix} - \sin\left(\frac{i_c}{2}\right)\begin{pmatrix} \sin\Omega_c \\ \cos\Omega_c \end{pmatrix}, \tag{4.7}$$

it was much easier to compute the proper radius and frequency at any given point in time. By placing the proper elements orbit around the origin, the conversion to the radius i_p can now be done easily, analogue to polar coordinates with $i_p = \sqrt{p^2 + q^2}$. While this value can approximately be seen as a constant, it does show some variation due to the higher order harmonics, which are not averaged out in the case of the Newton integration (compare Figure 4.10). As the variations are small in comparison to those in the osculating elements i and Ω, the mean value is taken here as the representative of i_p.

In order to compute the proper frequency, the following path is taken: first, the angle of the radius vector is computed at every time step, according to $\Omega_p = \arctan \frac{p}{q}$[21]. Second, the frequency itself is found by subtracting the value of one time step t_n from the following time step t_{n+1} and then dividing the result by the size of the interval $t_{n+1} - t_n$. In the course of the integrations, the time step was always set to 5 yr, as all integration runs were done for the same integration time of 5000 yr in total. The reason for this relatively long integration time (in comparison to the typical secular period of the oscillations, e.g. Figure 4.5a) is that the periods become longer for larger particles (see Figure 4.6a), and the integration time therefore needs to be adapted for all values to be able to compare the proper elements on the same timescales. Similarly to before, the proper frequency is also not a real constant of motion but again varies mainly due to the higher order harmonics. For this reason, we take the mean value of the list of $\Omega_{p,f}$ values, as well.

[21] This is different to the conversion from polar coordinates ($\phi = \arctan \frac{q}{p}$) due to the phase shift of 90° in the definition of the proper elements.

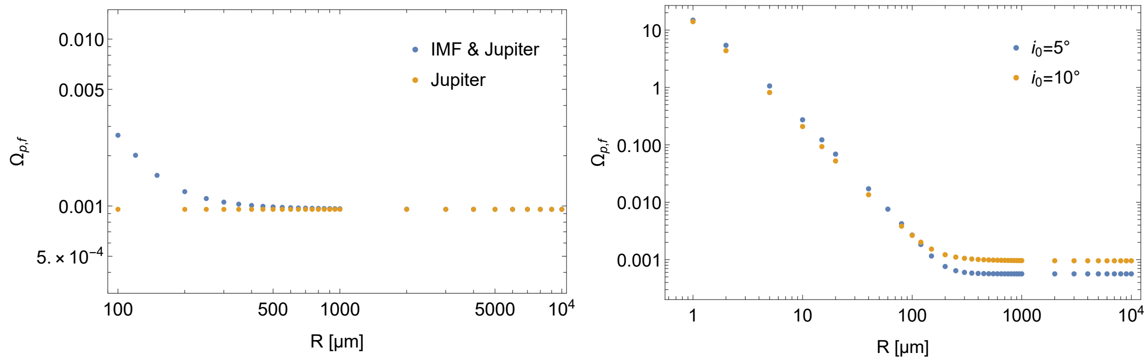

(a) $i_0 = 10°$

(b) Comparison of two i_0

Figure 4.12.: The mean proper frequencies (in °/yr) for a wide range of particle sizes R, comparing charged and uncharged particles, as well as two different orbits for the former case.

This was done for a larger range of particle sizes than in the previous section, as the secular period and the amplitude did not need to be computed. Instead only the integration for a set timescale needed to be run for several values of R. These computations were done first for $i_0 = 10°$ and then also for $i_0 = 5°$, to be able to compare possible constraints on particle size to that found in the previous section, and to see whether these constraints also depend on the initial inclination. The rest of the parameters were again set to the values in Table 4.1. Additionally, the same set of initial conditions were also used in simulation runs studying the motion of uncharged particles ($U = 0\,\mathrm{V}$, i.e. no interaction with the magnetic field). The results are displayed in Figure 4.12. We note that the results were computed with the Newton solution only, as the Gaussian model has the additional dependence on the adjustment of the α parameter, which would further complicate the analysis of the relation between the proper elements and the particle size.

As can be seen in Figure 4.12a, the proper frequency converges towards a value of around $9.5 \cdot 10^{-4}$ deg/yr, which is the value fixed by the influence of Jupiter. The oscillations in the proper elements driven by Jupiter are small, yet still noticeable in this representation and seem to dominate the evolution in the proper elements space for particle sizes of around 500 µm in the case of $i_0 = 10°$. As Figure 4.12b shows, the qualitative shape of the evolution of $\Omega_{p,f}$ is the same for both studied cases of i_0, while the values and the 'convergence limit' are different. It is interesting to note that for initially smaller inclinations, the proper frequency is slightly higher in the case of smaller particle sizes, while for larger R, this orbit shows smaller values in $\Omega_{p,f}$. This indicates that the variations driven by Jupiter are faster for more highly inclined orbits, while those dominated by the magnetic field maybe occur slightly faster for the $i_0 = 5°$ case. Interestingly, this transition occurs for a particle size of around 100 µm. Therefore, we also find a dependence of the proper frequency on the initial inclination (and hence also on i_p).

The comparison of the $i_0 = 5°$ case for the charged and uncharged particle (not pictured here) gives a similar result as Figure 4.12a, but the convergence of the two cases seems to occur a bit sooner, at a particle size of around 400 µm. This indicates an additional dependence on any upper constraint for the particle size on the initial conditions. In the previous section, the upper limit for the $i_0 = 5°$ orbit was assumed to lie at around 600 µm, due to the sign change in the slope in the evolution of Ω. As this comparison of the slope with and without the influence of

Jupiter cannot be reproduced by the orbit cases of $i_0 \geq 7.15°$ (as in these cases the direction of the slopes are already the same), this criterion cannot be applied for all orbits. An alternative upper constraint on the radius could therefore be given by the value of 200 µm, at which point the functions change their shape and start to converge towards the value set by Jupiter in both studied orbit cases, as can be inferred from Figure 4.12b. This would perhaps be the best value to set as some kind of upper limit, as there does not seem to a dependence on initial inclination for this turning point.

In conclusion, it is not unambiguous to set a fixed upper limit on the particle size for all studied orbits. Transforming into the proper elements space, however, does allow identifying a more concise change in the results.

4.7. Different initial conditions for i and Ω

As would likely be expected from (3.21) and (3.22), both the chosen value for the initial inclination and for the initial longitude of the ascending node strongly influence the oscillations in i and Ω. Different initial conditions lead to different frequencies and amplitudes, which has already been observed in the previous study on α, U and R. The initial orientation of the orbital plane therefore strongly influences its evolution.

For the periods in i and Ω, it appears that for initial values of inclination both larger and smaller than $i_0 = 7°$ the oscillation frequency is smaller (and hence the period is longer) for all values of surface potential U. A phenomenon that has already been seen in Figure 4.5a (and Figure 4.4a in the case of α). This indicates that towards the minimum amplitude solution, the period of the oscillation of i decreases quite significantly. As is also generally seen in these two figures as well as in Figure 4.6a, the uncertainty in the $i_0 = 7°$ calculations is more significant than for (most of) the other computations. This is because as i_0 approaches the value of the equilibrium condition, the oscillation loses its long-periodic shape (similar to the case of the smaller particles no longer displaying periodic oscillations), making it difficult for the algorithm to evaluate a period in such a variation. Therefore, it is reasonable to assume that near the equilibrium point of such a system, the secular period is no longer definable in an accurate way. Rather, the resulting variation likely only shows non-periodic oscillations instead of a discernible regular long-term evolution, i.e. a secular frequency overlain with higher order harmonics.

This is further supported by the fact that the Gaussian model can no longer accurately reproduce the resulting shape of the oscillation in i. As the equations (3.21) and (3.22) only take into account the long-period terms that do not average out over longer timescales, the assumption that at the minimum librational orbit a resonant period is no longer definable could explain this discrepancy. Strictly speaking, the Gaussian model of the equilibrium solution would represent an idealized case of such a system, as the amplitude remains very small at 7°, so the solution is nearly constant, as can be inferred from Figure 4.13c. This has also been observed in Figure 4.2, where the Gaussian result resembles an equilibrium point, while the full solution shows additional short periodic variations. This results in a wider range of inclination values that the orbital plane can reach.

Furthermore, it also has to be mentioned that the significant change in the frequency with the dependence on the inclination is not as well represented in the resonant equations using

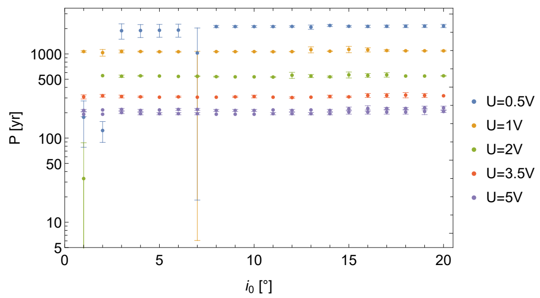

(a) Period to i_0, $\alpha_G = 8$

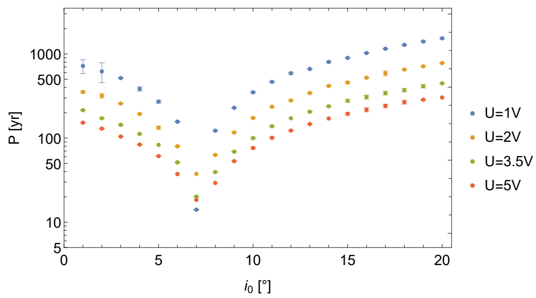

(b) The same as 4.13a, but with adjusted α_G

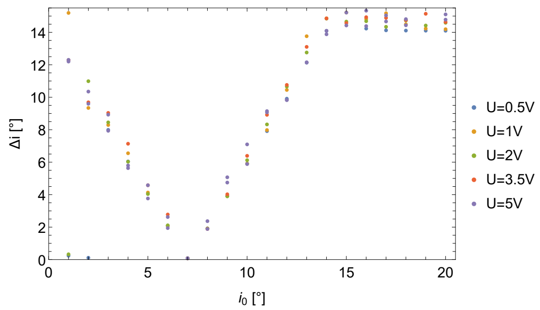

(c) Amplitude to i_0, $\alpha_G = 8$

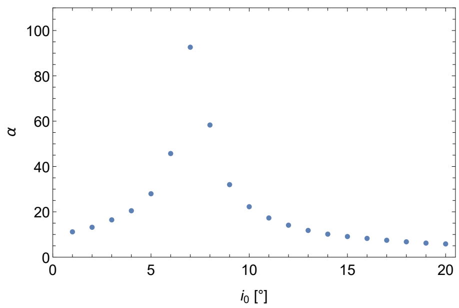

(d) Values of the α_G parameter to i_0

Figure 4.13.: Results for the Gaussian approximation and necessity of α_G adjustment. The left panels show the results of the period and amplitude of the oscillation in i to the initial inclination without adjusted α_G depending on different U. The upper panel on the right-hand side again shows the period but with the adjustment in α_G from the comparison to the full Newton solution. The lower right panel shows the values found for α_G from this comparison.

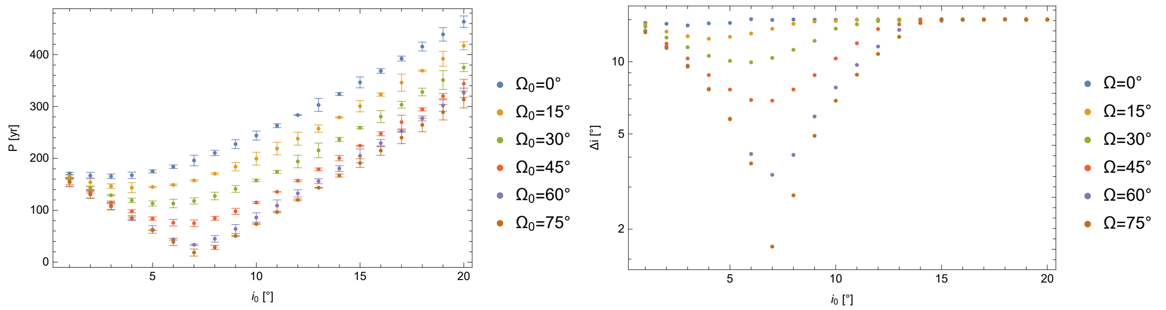

(a) Period of the i-oscillation to initial inclination depending on Ω_0.

(b) Amplitude with respect to the initial conditions.

Figure 4.14.: Changes in the period and amplitude in the variation of the inclination for different initial Ω.

the Gaussian model without significant adjustment of the α_G-parameter in the way described in Section 4.4. The change in amplitude with i_0, on the other hand, can also be seen in the results using only an arbitrary value of $\alpha = 8$, as can be inferred from Figures 4.13a and 4.13c. Additionally, Figure 4.13d also shows that the adjustment needs to be more significant for inclinations near $i_0 = 7°$. Again, this implies that the Gaussian result near the minimum librational amplitude cannot reproduce the resulting oscillation of the full solution. Rather, it also shows a periodic evolution, which is why the value of α_G in this case is so much larger than the others, as the algorithm tries to adjust the value according to a non-periodic comparison. It is interesting to note, however, that the Gaussian model does recreate the effect of the different charge to mass ratios (in this case due to a change in U), as indicated in Figure 4.13a. It therefore appears that neither a change in U nor in R requires a significant adjustment in α when comparing the different simulation runs for the same initial inclinations (when taking into account the limit of the minimum particle size). Further investigations have indicated that for larger values of the charge to mass ratio, a change in α_G does yield better fitting results. The change from the initial value is only small and the difference can potentially be neglected as an approximation, at least in comparison to the stronger change necessary to model the influence of the initial inclination value. However, by making use of the adjustment in α_G explained in Section 4.4, Figure 4.13b shows that the model is also able to reproduce more accurately the effect on the periods arising from different i_0, as well.

It is of course also interesting to look into the change in the oscillations in i and Ω due to a change in Ω_0. So far, all simulations have initially placed the particle's ascending node at the node of the intersection line of the ecliptic and equator, so always fulfilling one part of the Lorentz equilibrium condition. To ensure that the calculations are all still initiated at L4, the particles are now set to an initial mean anomaly of $M_0 = 60° - \Omega_0$. The range of values for Ω_0 was chosen as $[0°, 75°]$ in intervals of 15°.

For larger Ω_0 values, the resulting amplitudes in i are mostly comparable to the previous results, as can be inferred from Figure 4.14b. At $\Omega_0 = 0°$, the amplitudes are roughly the same for all inclination values, meaning that we find rotational motion in all cases. By increasing Ω_0, the amplitudes resemble the previous results, and we find that the smallest amplitude in i (and similarly also in Ω, not pictured here) is again found at $i_0 = 7°$, here for $\Omega_0 = 75°$. Hence, in this starting location, the particle's orbital plane does not deviate too much from its initial orientation, at least in the early evolution, as it starts closest to the minimum amplitude solution out of all the simulation runs of the Ω_0 study. Similarly, Figure 4.14a indicates the same behaviour, as we find the smallest period in the $i_0 = 7°$ case only for larger Ω_0 values, while smaller initial longitudes do not show this effect. These results rather indicate that the period increases steadily with i_0 for smaller initial Ω, which differs from the previous results, as they all either showed uniform periods for the given i_0-range or a decline towards 7°. Hence, in order to study the effects and all different structures in the amplitude and frequency of the i and Ω oscillations discussed so far, it is important to place the particle at (or at least near) $\Omega_0 = \Omega_c = 73.5°$. Figure 4.14b also clearly demonstrates the transition from the rotational regime to the librational regime for a wider set of initial inclinations at larger Ω_0. This again coincides with what has been inferred from the full i-Ω-phase space in Figure 4.2.

Therefore, it appears that the most relevant parameters dominating the dynamical evolution of the dust particle are the initial conditions i_0 and Ω_0, while the values of the charge to mass ratio only slightly alter the results in all cases, at least down to a minimum particle radius of around 2 µm. Below this point the particle motion can no longer be predicted by the model due to the loss of temporal regularity in the oscillations of the inclination of a charged particle trapped in the 1:1 mean motion resonance with Jupiter.

4.8. The minimum amplitude solution

As has already been shown in Figure 4.2, the i-Ω-space yields structures, which are – in the broadest sense – comparable to that close to the elliptic equilibrium in the a-Φ-phase space in Figure 3.5, resulting for the dynamics of the dust particle in the system without the Lorentz force. Similarly to that, it has been possible to find an equilibrium solution for the magnetically perturbed dust particle, i.e. to find the initial conditions for the Kepler elements, for which the parameters show no variation in the course of the integration. As mentioned before, the solution does not yield a true equilibrium, as the parameters do show some variations due to the additional influence of Jupiter. It is therefore preferred to refer to it as the minimum librational amplitude solution rather than a real equilibrium. In the system of a particle solely influenced by the sun and its magnetic field, however, it is a true equilibrium, which is why the set of values in i and Ω are further referred to as the equilibrium condition for the Lorentz force.

After several tests with various initial conditions, it became apparent that the algorithm for finding the period (discussed in detail in Section 4.3) became less precise for those calculations starting near this orbit. This is the case, because the function we find for the temporal evolution of the inclination looses its typical shape, for which it was possible to find a secular frequency overlain with higher order harmonics. The reason for this is the temporal variation in Ω, which is used for finding the extrema. While for starting positions further away from the minimum amplitude solution, Ω passes through all possible values in the case of rotational orbits, for those positions closer to $(i_0, \Omega_0) = (7.15°, 73.5°)$ the ascending node angle oscillates only around the equilibrium value.

As explained in the previous section, it appears that this secular period is therefore no longer definable, but rather we only see short-period changes which, initially, are likely due to the influence of Jupiter. Looking at the first few years of the evolution in this orbit and comparing it to the case without the influence of the Lorentz force, it seems that the evolution is quite

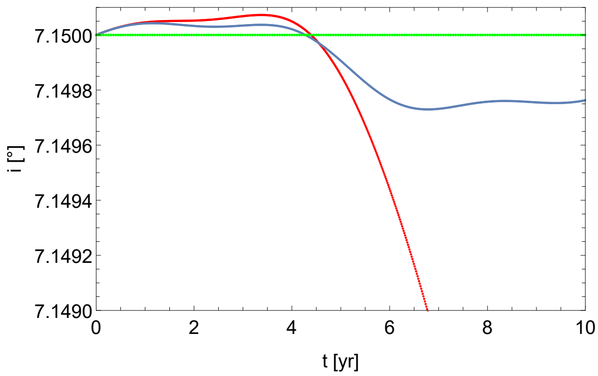

Figure 4.15.: A comparison of the first ten years of three different simulation runs: the evolution in i due to the influence of (i) both Jupiter and the magnetic field (red), (ii) just Jupiter (blue) and (iii) just the Lorentz force (green).

similar. However, already after some years, the influence of Jupiter drives small variations in the inclination of the order of 10^{-5} deg, seemingly positioning the particle slightly outside this equilibrium point, which triggers the influence of the Lorentz force terms. It seems that small deviations from the values set by the equilibrium condition for i_0 and Ω_0 already lead to the emergence from a real equilibrium. This can be inferred from Figure 4.15, where the results of three separate simulation runs are seen: for the case without Jupiter, the inclination is constant, while it is obvious that in the case without a magnetic field, but with the influence of the planet i does show small variations. The combined simulation run with both a magnetic field and Jupiter first shows the effect of the planet but quickly, after around two years, the influence of the Lorentz force increases as the particle is placed outside of the equilibrium position and after around five years, there is already a relatively strong deviation between these two simulations runs.

However, after integrating this orbit for 10 000 yr, it was seen that the ecliptic latitude of such a particle starting its orbit within the heliospheric current sheet does not reach values greater than about 8° or, alternatively, amplitudes of more than 2° in the case of $U = 5\,\mathrm{V}$ and $R = 2\,\mu\mathrm{m}$. This could indicate that the particle motion in the i-Ω-space within the minimum amplitude solution may still be dominated by Jupiter, or the Lorentz force is perhaps dampened by the planet, as the magnetic field seemingly has less influence compared to other initial orientations of the orbital plane. In addition, this idea is further supported when comparing that result to the case of $R = 0.5\,\mu\mathrm{m}$ in Figure 4.6b, where the Lorentz force is vastly dominant in comparison to the influence of Jupiter and we see a far stronger increase in the amplitude of up to 30° for $i_0 = 7°$ on short timescales already.

Interestingly, the Gauss equations do not yield an exact equilibrium result for $(i_0, \Omega_0) = (7.15°, 73.5°)$, as would be expected. Doing these same computations using the approximated equations, we find oscillations in i even in the a simulation run without Jupiter, which should not be the case when placing Ω at 73.5° in (3.21). However, as (3.21) and (3.22) are coupled, the latter equation has to be considered as well, which has not been done up until this point. So far, it has been assumed that the equilibrium condition for the inclination is found at $i_0 = i_c = 7.15°$, as it can be geometrically explained by the overlap with the inclination angle between the ecliptic and the solar equator and physically by the location of the heliospheric current sheet.

When solving (3.22) explicitly for i with the solution for $\Omega = 73.15°$, however, we find $i_0 = 7.041\,81°$. Running another test with these values in place as the initial conditions for the Gaussian model, the results do again show oscillations, but these are only very small with variations around the initial value i_0 of 10^{-5} deg. These are due to the influence of Jupiter, as is apparent when running the same test for the system without the additional planet which results in constant values for all Kepler elements, specifically so for i and Ω, for which the equations of the Lorentz force are in place. In the case of the approximated equations, these deviations are seemingly not enough to lead to a stronger influence of the Lorentz terms and to stronger oscillations, as was the case for the full solution.

Considering that the full Newtonian solution does indicate that the minimum amplitude solution is located at $(i_0, \Omega_0) = (7.15°, 73.5°)$ and that only a small change in these values leads to a destabilisation of this equilibrium (as is inferred by the non-periodic variations in i resulting from the small deviations caused by Jupiter as seen in Figure 4.15), it is unlikely that the slight alteration in i_0 found from the Gaussian approximation has any physical implications. This slight shift in the location of the equilibrium point is rather likely due to the truncation error made in the approximation of the variation equations for i and Ω. In Lhotka and Galeş 2019, the authors point out that the secular terms of the normal component of the Lorentz force used to find (3.21) and (3.22) are taken up to first order in x_0, y_0 and $1 - z_0$. Hence, all higher order terms are neglected in these equations and, when taking into account the values of these parameters in Table 4.1, this can likely explain the small deviation in i_0 for the approximation.

In conclusion, the equilibrium solution suggested by the Gauss equations (3.21) and (3.22) is disrupted early on due to the influence of Jupiter, leading to small amplitude variations of the orbital plane. The position of this minimum amplitude solution coincides with the heliospheric current sheet and can be approximated by the Gaussian model.

4.9. Dynamical behaviour outside of L4

So far, all simulations have modelled the motion of a dust particle located at the L4 point on Jupiter's orbit. It is further interesting to study potential differences for other orbits by comparing the results from the L4 solution to those of the L5 orbit, a tadpole orbit, a horseshoe orbit, as well as to an orbit of a particle moving out of resonance with Jupiter. The aim is to see how strongly the influence of the magnetic field alters the particle motion at different regions in the solar system, and how – or if – the planet may affect them differently.

Similarly to the computations of the L4 region, the calculations in this section were done at $\Omega_0 = 73.5°$ for a range of i_0 =1° to 20°. For the L5 region, Φ was set to 300° by adjusting to the necessary M_0. For the horseshoe and out of resonance orbit, the particle motion was started in the vicinity of L4. The chosen horseshoe orbit is initially located at a distance to the star of $a_0 = 5.5$ AU (which was a value chosen after some test runs with varying distances to find one such orbit), while the out of resonance particle is located at $a_0 = 3$ AU, at the location inside the main asteroid belt[22]. In this region, there is presumably also quite a large amount of dust particles originating from these asteroids, which are also affected by the Lorentz force and by Jupiter. The tadpole orbit is studied at $\Phi = 133.5°$, so at the Lorentz equilibrium point and an

[22] https://astronomy.swin.edu.au/cosmos/m/main+asteroid+belt, last accessed on 30.06.2021.

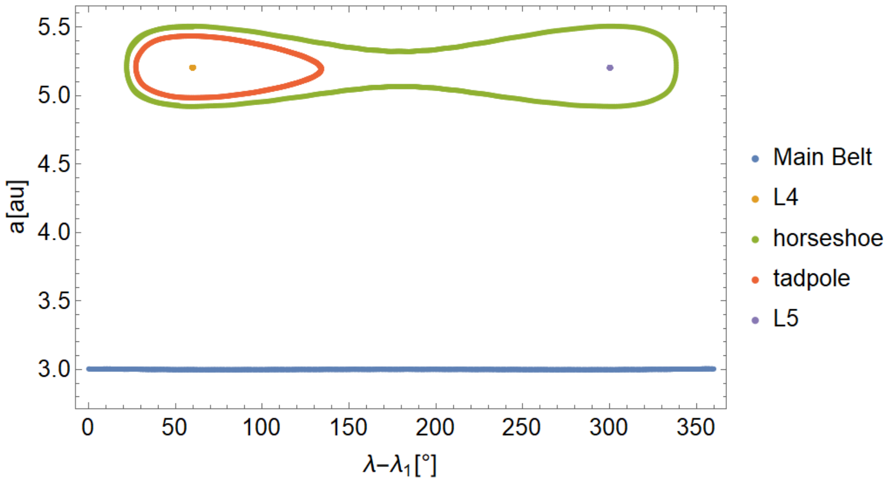

Figure 4.16.: Representation of the different orbits for the simulation runs in the a-Φ-space.

initial mean anomaly of $M_0 = 60°$. As before, during the variations of Ω_0, the mean anomaly is adjusted to always place the particle in that location. The different orbits are shown in Figure 4.16.

After repeating the simulation runs from the previous sections for the other orbits and comparing the results for both the amplitude and the period in i_0 using the full solution of the Newton equations[23], we find a similar structure of the i-Ω-space and also comparable values of the periods and especially the amplitudes. As an example, the i-Ω-space for L5 and the out of resonance case are provided in Figure 4.17. These similarities are interesting to note for the orbits outside of the Lagrange points in general, as it indicates that setting the particle at the gravitational stability points is not as relevant for its motion in the i-Ω-space as would perhaps be expected. The biggest differences arise only when placing the particle further inward or outward in the solar system, as the influence of the Lorentz force becomes stronger or weaker in these cases, respectively, as can be understood from the equations (3.19), (3.21) and (3.22) due to the dependence on $\frac{1}{a^2}$.

In Zhou et al. 2021, the authors showed differences in the Lagrange points L4 and L5 in the case of Venus, when the particles are affected by additional forces. Their results indicate that the most dominant factors leading to asymmetries between L4 and L5 are the solar radiation pressure, the Poynting-Robertson effect and the solar wind, rather than the Lorentz force. The latter is assumed to have a smaller effect except for very small particles. The results of the comparisons in our study have shown that there appears to be no difference between the L4 and L5 cases (for illustration, compare Figures 4.2 and 4.17a), which is in accordance with Zhou et al. 2021, as the other, dominating forces are not considered here and the particles in these simulation runs have a size of 2 µm. The deviations in the values for the amplitude are all of the order of 10^{-1} deg, while the differences in the periods are typically around 10 yr, which lies within the error of the period computation, as will be discussed further in Section 4.11.

[23] We note that the Gaussian model is not used in these comparisons, as the assumption of $r \sim r_1$ was used in the derivation of the equations in Section 3.2.1. Therefore, it cannot accurately model the motion of particles with a different semi-major axis to Jupiter.

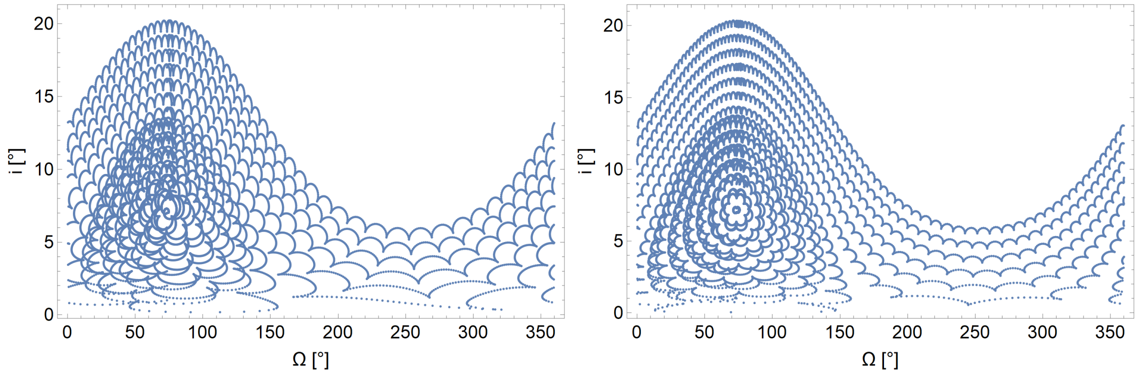

(a) L5

(b) out of resonance

Figure 4.17.: Phase space for a particle positioned at the L5 point and a particle out of resonance.

Upon comparing the results for the particle out of resonance to all other solutions, it becomes apparent that both the period and the amplitude in i resulting from this orbit are smaller on average. When looking at this in the i-Ω-space (see Figure 4.17), it appears that the orbits show a wider spread in the parameter space in the situations in which the dust particle is located near Jupiter, especially for the librational regime. For the case out of resonance, the particle is more than 2 AU away from the perturber, hence it is less heavily influenced by the planet. This reduced gravitational influence of Jupiter is, however, not the reason for the decrease in the amplitude of the short-period oscillations (i.e. the higher order harmonics), as would perhaps first be expected. While it has been seen that the proximity to the planet does seem to 'break' the equilibrium and push the particle outside of it, it does not significantly modify the short-period evolution outside of the minimum amplitude solution. The comparison of the two orbits in Figure 4.17 clearly shows that the case out of resonance results in relatively small variations of the orbital plane, which is not the case for the particle orbit near Jupiter. Further tests have shown, however, that the decrease in the strength of the higher order harmonics can be traced back to the particle's distance to the sun, rather than to Jupiter. This will be discussed in the next section, where we will look at cases at different solar distances without the influence of the perturbing planet.

The comparison to the case out of resonance is a very idealized picture, as in reality, there are further additional forces to consider. For a more accurate representation of this location in these computations, the radiation pressure, the Poynting-Robertson effect and additional influences due to the solar wind (aside from the expansion of the magnetic field lines) would modify the particle motion especially outside of resonance via the other orbital elements. As previous studies have already discussed (e.g. Liou and Zook 1995), dust particles can be trapped inside a resonance for quite a long time (several thousand years), preventing the inward spiral (or outward migration) which would otherwise occur due to the combination of the other forces in these resonant regions. During the time in which the particle is trapped inside the resonance, however, the assumption that the Poynting-Robertson and solar wind effect, as well as the influence of the solar radiation pressure (which causes a simple shift of the location of the resonance) are negligible terms is a reasonable approximation for the problem. However, this is no longer the case for a particle outside of resonance, where these other forces would be dominant. Still, it is interesting to see the change introduced in the parameter space that is attributed to the proximity of the particle to the sun, leading to the slightly larger amplitudes for greater distances, i.e. also near Jupiter.

4.10. System without Jupiter

To study the influence of the Jupiter-like planet on the dynamics of the dust particles in connection with the Lorentz force in greater detail, it was attempted to compare the findings of the previous sections to the system with no perturber at all and hence solely look into the effect of the magnetic field. This was done initially to analyse any supposed contributions of Jupiter on the higher order harmonics, in order to safely be able to rule out this effect in the comparison to the out of resonance case from the previous section.

For the sake of comparability, the starting position of the particle in the simulations without the planet was chosen to match the position in the L4 case with Jupiter. From the investigations (results not pictured here), it was inferred that the shape of the oscillations for all orientations of the orbital plane depending on i_0 – except for the minimum amplitude solution – are the same in both cases. The isolated effect of the magnetic field again results in a superposition of the secular frequency and higher order harmonics, which shows that these do not form due to the influence of Jupiter. The difference between the two scenarios can only really be seen (for the 21 studied cases) in the case of the minimum amplitude solution. In the case without Jupiter, the orbit remains inside the equilibrium position for a longer period of time up to around 100 yr, which is not the case for the gravitationally perturbed particle. Here, the equilibrium position cannot be maintained at all.

One would expect that, if there is no planet further perturbing the system, the particle starting its orbit within the equilibrium point would remain there, as there is no additional force destabilising its motion, as is proposed in Section 4.8 and suggested at least for the first few years in Figure 4.15. However, integrating the full Newton solution for such a system has shown (not pictured here) that this is not the case, but rather the evolution in the i-Ω-space also shows oscillations after some 100 yr for particles starting at Jupiter distance to the sun. In the case of the Gaussian approximation, it was seen that upon initialising the particle location at the Gaussian equilibrium point (with the slightly different values for i_0 in the model, as explained in Section 4.8), the case for a system without Jupiter does remain constant at i_c and Ω_c. There are no other forces which would lead to changes in the two parameters, according to equations (3.21) and (3.22).

It could be that the destabilisation of the Newton cases are due to small computational errors in the integration, as earlier tests have indicated that small changes of the order of 10^{-5} deg in i and Ω can already lead to oscillations producing a minimum librational amplitude orbit rather than a real equilibrium. As this only poses a notable difficulty for this one particular type of orbit (i.e. at $(i_0, \Omega_0) = (7.15°, 73.5°)$), it does not introduce any additional numerical errors into the rest of the computations.

In order to investigate the reduced amplitudes of the higher order harmonics in the case out of resonance seen in Figure 4.17b, several more simulations were run in an interval of $a_0 = [1, 20]$AU,

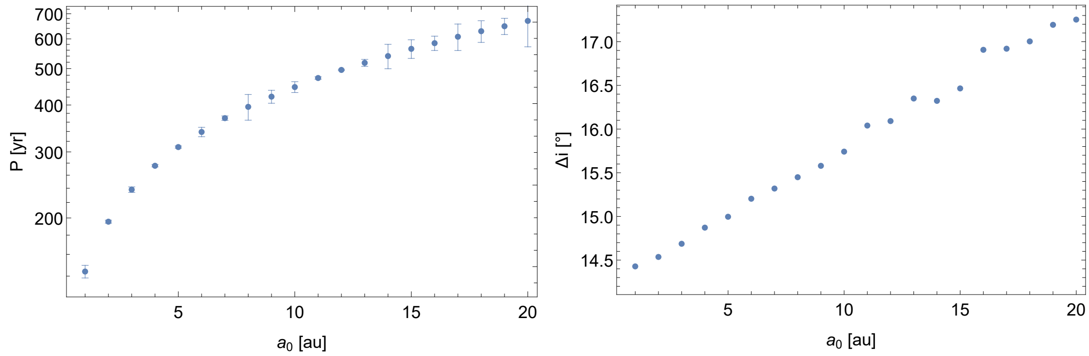

(a) Secular periods to a_0

(b) Amplitudes to a_0

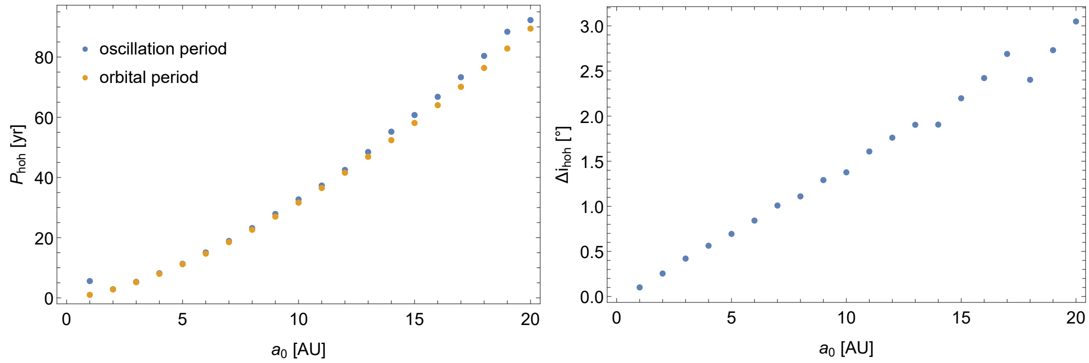

(c) The mean oscillation and orbital period

(d) The median of the amplitudes

Figure 4.18.: Results for the Newton computations of the period and amplitude for the secular oscillation in i (upper panels), as well as for the higher order harmonics (subscript 'hoh', lower panels). The initial value of the inclination is set to 20° in all cases pictured here.

with a step size of 1 AU, to test the influence of solar distance.[24] The initial inclination was set to $i_0 = 20°$ in all cases. Results in Figure 4.18 show that the semi-major axis affects the higher order harmonics in a way already expected from the results of the previous section, namely that both the amplitude and the period increase towards larger distances. This results in the stronger higher order harmonics for the particle located near Jupiter's orbit. Initially, this is perhaps counterintuitive, as the Lorentz force decreases towards larger a, which may lead to the assumption that the strength of the higher order harmonics decreases, as well. Additional tests towards even greater distances of $a_0 = 30$ AU (not pictured here) have shown that these oscillations become more dominant instead, resulting in a more 'chaotic' structure of the i-Ω-space, with a number of overlaps between orbits, already noticeable for a distance of 20 AU.

The correlation between the higher order harmonics and the solar distance is also reflected in a relation of their oscillation frequency and the orbital period, as is suggested in Figure 4.18c. At a given distance, these two values match, indicating that the higher order harmonics arise

[24]We note that the `FindPeaks` function (described in Section 4.3) was used to compute the periods and amplitudes of the higher order harmonics of the Newton solutions. The minima were located by applying the function to the negative data set and determining the maxima there. These results were then again reversed to compute the amplitudes by subtracting each minimum from the nearest maximum.

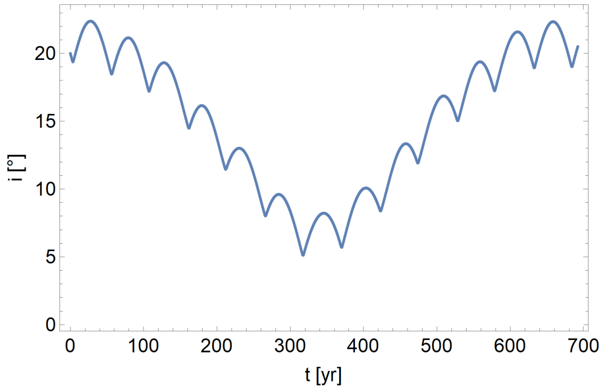

Figure 4.19.: An example of the oscillations in i for a particle located at $a_0 = 20\,\mathrm{AU}$.

due to the sign change at the solar equator, which the particle passes twice in the course of one orbit. This passage then likely results in these smaller oscillations superimposed on the secular evolution. Furthermore, this explains the longer periods of the higher order harmonics at larger distances, as the particle needs more time to complete one full orbit, i.e. its orbital period is longer. Hence, it takes longer until the dust grain passes through the heliospheric current sheet again, prolonging the time until the sign change occurs.

Similarly, this also means that the magnetic field – even though its strength has decreased at larger a_0 – has much more time to act on the particle in one direction before the polarity reversal. This likely results in the larger amplitudes of the superimposed oscillations. In actuality, the size of these amplitudes does not remain constant over one whole secular period, as the higher order harmonics have to follow the shape of the secular curve. As can be inferred from Figure 4.19, this leads to a distortion of the short-period oscillations especially at the inflexion points. Hence, the amplitude values after each orbit completion are not constant. Again, depending on solar distance, these values may vary between a fraction of a degree up to some two to three degrees, with larger deviations at larger a_0. In order to account for these small differences, the median value of the amplitudes was chosen for Figure 4.18d.

In addition, we note that the evolution we see in Figure 4.19 only represents the case for the isolated effect of the magnetic field. For a realistic example of particle motion outside of resonance unaffected by planetary perturbers, it would be important to incorporate additional force terms, namely the solar radiation pressure and the Poynting-Robertson effect. Considering the influence of those forces, it is unlikely that the particle would remain at the given solar distance for a few hundred years, as is the case for the test object in Figure 4.19. Rather, as the particle is 'dragged' towards the sun due to the Poynting-Robertson effect, both the period and the amplitude would decrease with time. This is the case for both the secular oscillations and the higher order harmonics. Instead of the consistent oscillations in i and Ω according to Figure 4.19, it is therefore more likely to find an evolution along the curves shown in Figure 4.18 for the secular and short-period oscillations as the particle moves inwards in the solar system.

Additionally, the results of the simulations without Jupiter seem to suggest that the distance to the sun also influences how long the parameters may remain constant in the case of the minimum amplitude solution (not pictured here). For a distance to the sun of up to 3.8 AU, i and Ω appear to remain constant for prolonged periods of time, while for larger distances the orbit eventually leaves the equilibrium position in the i-Ω-space after around 100 yr in all cases out to 10 AU. At 20 AU, the time it takes for the orbital plane to leave the equilibrium state is about 200 yr. There are no forces affecting particle motion other than the Lorentz force (which should be effectively zero in these cases due to placing the particle within the heliospheric current sheet) and the gravitational force from the central body (which should not introduce any variations in the orbital elements except for the mean anomaly) in this case. Considering that this deviation from the constant value always occurs at around the same time for different distances of more than 3.8 AU in the cases without Jupiter, it is likely that this is due to small numerical errors arising during the integration process, as suggested earlier. These may be due to some difficulty in integrating the effect of the sign change.

4.11. Evaluation of period computation

In the previous sections, the period lengths were given with an error bar derived from equation (4.1). For further validation of the period calculation explained in Section 4.3, the results for the L4 and the L5 points are compared. As the results in Section 4.9 have shown, there do not appear to be any discernible differences in the dynamics of the two locations, when taking into account only the influence of Jupiter and the magnetic field. Any differences in the periods and amplitudes are therefore likely only due to uncertainties in the period calculation. This comparison was done for for each value of i_0 from the variation in the surface electric potential U. For the period, the differences between L4 and L5 resulted in around +10 yr for the L4 results for all U values with the full Newton solution. The case of $i_0 = 7°$ again marks an exception with a difference of less than +5 yr, which is due to the fact that the calculated 'period' for these runs is very short.

As expected, the differences in the amplitudes are only small and reached +1° for L4 only in some cases. Typically the difference between L4 and L5 lies at around 0.5° and this deviation is larger for larger U, indicating that higher charge to mass ratios may lead to a difference in the L4 and L5 distribution, but it is not possible to rule out simple coincidence in this case. It is interesting to note also that the difference in amplitude between L4 and L5 more or less vanishes for $i_0 \geq 16°$, which roughly coincides with the orbits that rotate in the i-Ω-space rather than showing a librational motion, meaning that the rotational cases are the most comparable results for L4 and L5, which also coincides with the fact that the amplitudes of these orbits do not change significantly for different charge to mass ratios, either (compare e.g. Figure 4.5b).

For comparison, the uncertainty in the calculations computed with the method using equation (4.1) has shown larger values in the error bars of the previous figures ranging mostly up to 20 yr and with some outliers up to around 55 yr, especially for higher initial inclinations. This is due to the formula used, as it assumes (for the smallest errors) that the minimum is located right in the middle of the two maxima. However, due to the superimposed higher order harmonics and the way in which the minimum is found in the function, this is not necessarily the case (see Figure 4.3a, where the actual minimum location is shifted slightly to the left). Hence, we find slightly larger errors here, especially for the higher i_0 runs, which have longer periods. These may have quite the difference in the distance of the minimum from the first and second maximum, depending on the strength of the higher order harmonics and, therefore, on the location of the minimum.

For the quantification of the uncertainty of the period computation in the Newton case, it is therefore better to assume an overall uncertainty of around 20 yr. The best way to improve this could be by also locating the minimum in the same way as the maxima. For this a comparison in Ω would likely need to be made to a value of 253.5°, which is where the minimum is located for the rotational orbits in the i-Ω-space according to Figure 4.2, while for the librational regime a more distinct comparison for $\Omega = 73.5°$ would need to be made. This could be done by further implementing the comparison of $i(t)$ to i_0, as already used to differentiate between the maxima and minima. This has already been described in Section 4.3. However, for the purpose of this first general look into the influence of the Lorentz force on the evolution of i and Ω and the differences due to a wide range of initial conditions, this computation works well enough.

Similarly, the differences between the L4 and L5 point are calculated for the Gaussian results in the period and amplitude for the adjusted values, as well, and for L4, the uncertainty calculated with (4.1) is also looked at separately. For the period, the differences between L4 and L5 also show values of up to +15 yr, but the values are more scattered within the $[0, 15]$yr range. This is likely simply due to the combination of both the uncertainty in the approximation of the period in the α adjustment and the error already stemming from the Newtonian period computation. The uncertainties found with (4.1) show on average smaller values than in the Newton cases (see e.g. Figure 4.13b). Again, this is likely due to the absence of the higher order harmonics and the more exact location of the minimum midway between the maxima.

For the amplitude, the differences between L4 and L5 again range only between $[-1, 1]°$. Interestingly, the smallest differences are found near the equilibrium point. This is the case because even though the periodicity of the Gaussian approximation no longer resembles the full solution, these equations yield only very small variations around the initial value, so they would reproduce a more idealised equilibrium. Therefore, as in the Newtonian case, the amplitudes are largely comparable between L4 and L5, indicating no errors in the amplitude computation, while the uncertainty in the period from this computation can be assumed to be smaller on average than in the Newton case, due to the more precise minimum measurement. It can be assumed to be around 15 yr. In conclusion, we note that the uncertainties in both the amplitude and the period arising from the computation methods are generally quite small in comparison to the typical value range, yielding satisfactory results for this investigation into the general effects of the interplanetary magnetic field on the evolution of the orbital planes of charged dust grains.

5. Discussions and Conclusions

In this chapter, we will expand on the results of the previous sections and discuss which implications could be inferred for the dynamics of charged dust particles near Jupiter. This will also be done with regard to what might be expected for findings of future observations, which would serve as potential confirmation of these results. First, possible implications on the general distribution of particles in a dust cloud – inferred from the evolution of i and Ω due to the influence of the Lorentz force – are considered. Second, some deliberations are made on the influence of a more realistic, time-dependent magnetic field and the influence of a different orientation of the heliospheric current sheet within the solar system according to different tilt angles. Additionally, we will also give some more thought to the behaviour of particles outside of the resonant region, with the considerations of additional forces neglected so far. Lastly, some more technical aspects will be considered as well, by discussing the second equilibrium solution suggested by the Gauss equations, and a general assessment of the Gaussian model according to the previous results will be made.

5.1. Implications for particle distribution

Simulations of a singular charged dust particle affected by the Lorentz force as well as by Jupiter do not result directly in an unambiguous picture of the distribution of the large amount of dust expected to reside in the Trojan regions. However, as the results of Chapter 4 do demonstrate the basic effects of the interplanetary magnetic field, it is still possible to make some more general assumptions based on these findings. These allow us to deliberate on how they could be interpreted for larger amounts of dust, assuming an initially evenly distributed cloud of charged particles in resonance with Jupiter. First, however, some more basic information garnered from the results are discussed and briefly compared to those of other studies.

From the previous figures showing the amplitude ranges for given initial inclinations i_0 (such as Figure 4.5b, for example), it is evident that the dust particles show a relatively wide spread in their vertical distribution. This has also been reported in Liu and Schmidt 2018a for larger simulations of dust produced by the Jupiter Trojans. It is interesting to note that in their follow-up paper, Liu and Schmidt 2018b, the authors find an accumulation of dust particles of $1\,\mu\text{m}$ size near $i = 40^\circ$, which would not be expected from the results of this thesis. Here, the only simulation run that reaches a comparable inclination is the case of the $0.5\,\mu\text{m}$ particle, and only if it starts near the equilibrium condition in i and Ω (compare Figure 4.6b). In the course of this thesis, a set initial inclination range of $[1, 20]\,^\circ$ was used, while in Liu and Schmidt 2018a, the simulations were initialised by placing the particles on the same orbit as the asteroids from which they originated. However, while some of the Trojan asteroids do seem to have inclinations of up to 40°, the mean inclination for the L4 region is only around 13.7° according to the results of the sky survey by Jewitt, Trujillo and Luu 2000. Therefore, it is unlikely that the authors started with many cases of $i_0 > 20°$, which could have potentially explained the larger inclination values they found. It should be pointed out, however, that this form of the set-up of the initial conditions of Liu and Schmidt 2018a implies that the Ω condition is likely not fulfilled in the vast majority of their simulation runs (i.e. $\Omega_0 \neq 73.5°$). Therefore, they likely find more rotational rather than librational orbits (compare Figure 4.14b), and – depending on the initial orientation of the orbital plane of the particles along the ecliptic latitude – this may lead to higher inclinations.

Aside from the initial conditions, Liu and Schmidt 2018a used a constant surface potential of 5 V. On that account, their results are most comparable to the simulation run in Section 4.5 for the case of 1 µm particles, for which we have found much smaller inclinations in comparison. What also needs to be taken into account and has been disregarded in the comparison so far is that the simulations in Liu and Schmidt 2018a include the whole set of force terms. They also found that, for small particles, the radiation pressure gains influence, which leads to shorter particle lifetimes. This is an additional effect that may explain the difference in the results. As this force term should not play a major role in the oscillation of i, however, it is unlikely that the higher values found in their simulations are directly due to the radiation pressure. Rather, they may be connected to a greater change in a, e or ω, which would then indirectly influence the distribution along the ecliptic latitude, as well.

Additionally, it also has to be taken into account that Liu and Schmidt 2018a did not use the exact same model of the magnetic field as in the simulations of this thesis (which followed the model of Webb et al. 2010 for the general structure and Lhotka and Galeş 2019 for the secular evolution, as explained in Section 3.3). They modelled the interplanetary magnetic field according to Gustafson 1994 and Landgraf 2000. While the authors make similar assumptions in these models, they also include an average polarity for the magnetic field, which has not been done here. This likely also introduces some differences in the findings. Generally speaking, however, it can be seen that the results of the two approaches are in agreement with each other in terms of a wider spread in the ecliptic latitudes and likely a stronger preference for higher inclinations than would be possible without the influence of the magnetic field. These findings also correspond to what has been expected from other studies, as well. The oscillations in both i and Ω have, for example, also been found in Krivov, Kimura and Mann 1998, wherein the authors have already pointed out that the orientation of a particle's orbital plane is determined by the magnetic field.

Furthermore, even though this thesis has shown that there is a set of initial conditions which yields a minimum amplitude solution, it has been seen that particles starting within that orbit near Jupiter will quickly show a deviation from what would otherwise be an equilibrium position in the inclination and the longitude of the ascending node. Even though these deviations are small and only show oscillations of around 2° in most cases, this still indicates that there may be fewer dust particles than would be expected solely from the equations near the heliospheric current sheet in the vicinity of a planet. On the other hand, further away from any planet, the dust density near the current sheet is likely higher, as here the particle's orbital plane may remain inside this equilibrium position in i and Ω for longer periods of time, as could also be inferred from the comparison between the L5 orbit and a particle out of resonance in Figure 4.17. In the latter case, the particle obviously remains on its minimum librational amplitude orbit at least for a prolonged period of time, showing smaller deviations. This is further discussed in connection to the other force terms, which become more relevant outside of resonance, in

Section 5.3. In the case without any effect of a planetary perturber, the dust density inside the current sheet would likely be highest, as suggested by the simulations runs in Section 4.10. For particles moving on orbital planes which are not aligned with that region, however, the distribution should be the same in either case.

Figure 4.17 also indicates that it is more likely to detect a larger number of dust particles at a given ecliptic latitude near the Jupiter region than further inward in the solar system. As pointed out in Section 4.10, this is largely the case not because of the influence of the planet, but rather due to the change in the shape of the higher order harmonics with increasing solar distance. At Jupiter distance, oscillations of higher amplitude in the i-Ω-space are reached, meaning that more dust particles of initially smaller inclinations tend to reach higher ecliptic latitudes, leading to a wider spread in the vertical direction. On the other hand, the stronger variation of the higher harmonics also means that, in turn, more particles reach smaller values of inclination, which would mean that there would not be a preference for the higher inclinations, exactly. In any case, however, the results indicate that at a distance of around $a_0 = 5.2\,\mathrm{AU}$, a larger number of dust particles can reach slightly more extreme inclinations, likely making more detections at moderate and higher ecliptic latitudes (in this case meaning around 13°) a greater possibility than in cases further inward in the solar system. This is mostly due to the fact that initially smaller inclinations seem to be able to reach larger values, while at shorter solar distances the amplitudes are smaller. Any additional influence by Jupiter itself is noticeable only nearest the minimum amplitude solution, leading to earlier deviations from the equilibrium.

As far as the difference between L4 and L5 is concerned, the results of this parameter study have shown (in Sections 4.9 and 4.11) that there is no great variation between the two locations, when simply considering the evolution of one test particle influenced by the Lorentz force. As pointed out in Section 4.9, this is also in agreement with what has been suggested for the effect of the magnetic field on the symmetry of the two positions in Zhou et al. 2021 (although this work focused on the case of the e-ω-space along Venus's orbit). From our results, it cannot be ascertained whether or not we would find asymmetries in the i-Ω-space between L4 and L5 due to the influence of Jupiter or the magnetic field, or whether the distribution of dust particles would be roughly the same between the two locations (aside from the difference in the actual amount of particles due to the asymmetry in the number of asteroids[25] between the Lagrange points). We would, however, expect that future observations find that the latitudinal distribution of the dust particles are very similar. The simulations also suggest the same for particles moving on a tadpole and horseshoe orbit near Jupiter, as a similar trend in both period and amplitude was found in those cases for different charge to mass ratios. This is interesting to note, as Liu and Schmidt 2018a have pointed out not only a wide spread in the vertical distribution of the dust particles (which was used as an incentive for this thesis), but they also found a wider azimuthal distribution. The results of these investigations suggest that the particle distribution in these regions should be the same or at least similar to that located initially in the Lagrangian equilibrium points. Generally speaking, it is therefore likely that the particle position relative to Jupiter at fixed semi-major axis makes little difference in the resulting evolution of the orbital plane.

As described in the course of Chapter 4, this study takes into account particles of a constant charge, specifically studying the effect of different charge to mass ratios in Section 4.5. The assumption of a constant charge only holds as long as the assumption of a consistent plasma

[25] See e.g. https://minorplanetcenter.net//iau/lists/JupiterTrojans.html, last accessed on 13.08.2021

environment is also satisfied, as pointed out in Lhotka and Galeş 2019. Since the time-dependency of the magnetic field is not taken into account in this thesis, this condition is met. Strictly speaking, however, there are a variety of charging mechanisms in the solar system (for a discussion on some of the different plasma environments see Lhotka, Rubab et al. 2020), which could potentially lead to some variations of this equilibrium charge. However, as discussed in Lhotka, Rubab et al. 2020, any changes typically equilibrate on timescales of a few nanoseconds, indicating that it is unlikely that sudden changes in the particle charge would lead to differences in the results, especially considering the comparatively longer integration times in all cases. The tentative study on different equilibrium values of the charge of dust particles done here, however, does allow some deliberation on how the strength of the particle charge itself influences the distribution. As has been inferred from Figure 4.5, particles with a higher electric surface potential generally show slightly larger amplitudes in their oscillations with a higher frequency, with a difference between 1 V and 5 V of around one order of magnitude. This indicates that it could be more likely to detect particles of a higher surface potential simply because their inclinations display faster oscillations. Therefore, considering a dust cloud with the same numbers for different charge to mass ratios, those of higher charge would likely be detected more often simply due to the stronger oscillations of their orbital plane.

From the shape of the i-Ω-space in Figure 4.2, it can be inferred that, generally, more particles should be detected at smaller ecliptic latitudes up to 14° with Ω between around 0° to 120°. Particles of these parameter ranges show a librational behaviour in the i-Ω-dynamics, and their orbital planes are therefore likely to remain near that position. In comparison, the particles displaying rotational behaviour in the parameter space show a greater change in their orbital plane, meaning that less particles should be detected in those regions on a given timescale. This is the case for particles with a size of around 2 µm. For the smaller particles, the distribution is somewhat more difficult to assess due to the large amplitude ranges we have found for all initial inclinations in Figure 4.6b. It can be said, however, that due to the non-periodicity of their oscillations, it is likely that the smaller dust particles are more uniformly distributed in their ecliptic latitudes. In contrast, the larger particles display a temporal regularity with their unchanging periods, making it on the one hand easier to predict the evolution of their inclinations, but on the other hand also meaning that there are certain i values, where more particles are likely to appear on a given timescale.

Evidently, there is a large number of factors to consider when talking about the distribution of particles in a dust cloud and the likelihood of detection. From the results of Chapter 4, we would expect that future investigations focusing on the region dominated by librational orbits would give a greater likelihood of detection. Furthermore, we would expect more particles of higher charge to mass ratios to be found. The vertical distribution of the dust particles between the L4 and L5 region should be comparable (with respect to the relative numbers of the objects in these regions).

5.2. Possible effects of the solar cycle and the current sheet

When considering the results discussed in this thesis, it is important to keep in mind that the computations used a time-independent model of the magnetic field. Hence, it neglected the change of polarity that occurs every 11 years. This was done in order to understand the basic effect of the Lorentz force terms on the evolution of particle inclination and longitude of ascending node, and to be able to describe these effects with an analytical model. Further simplifications have also been made on the orientation of the current sheet, as it is assumed to be flat and to reside within the equatorial plane of the sun. In reality, these simplifications are quite different from the complex structure of the interplanetary magnetic field, and the solar cycle also influences the orientation and shape of the heliospheric current sheet. Some preliminary considerations on the effect of these additional complexities – and what it could imply for the results – are made in the following.

According to Smith 2001, the size of the heliospheric current sheet increases with the distance to the sun. As also pointed out in this study, it is still unclear what exactly happens within the current sheet itself. It is possible that either the polarity of the magnetic field ‘flips’ via rotation instantaneously, or that the strength decreases to zero as it enters the current sheet before the field lines again emerge with the opposite sign on the other end. In the case of this thesis, the same approach as in Lhotka and Galeş 2019 was used for modelling the current sheet, namely by approximating an instantaneous change in polarity with the *tanh*-function as a representation of the Heaviside function, as seen in Figure 3.7. The thickness of the current sheet in this case corresponds to the α parameter, as already described in detail in Sections 3.3.1 and 4.4. As Figure 4.4a has shown, smaller α values lead to the same frequencies for all initial i_0 cases. As a smaller α corresponds to a broader current sheet, dust particles of small to moderate initial inclinations, for which the orbital planes would now coincide with the current sheet, in this case all show similar behaviours in their oscillation frequencies but not in their amplitudes. This indicates that – in connection with the assumption of a broader current sheet at greater heliocentric distances – while the width of the vertical distribution remains the same, the changes in the inclination with time may become more similar for all particles in those outer regions in a more realistic system.

Taking into account the solar cycle means that particles are influenced differently during the crossing of the current sheet every 11 yr. Depending on the orientation of the orbital plane of particles and their exact position on the orbit, some particles start their orbit in the magnetic south, so with a negative sign for B_0 in (3.19), (3.21) and (3.22). As they complete one orbit, these particles first pass through the ascending node of the intersection line of their orbital plane and the current sheet into the magnetic north, where they then experience the influence of a positive magnetic field, before again ending up in the magnetic south. The opposite is true for the particles starting in the regions with the positive B_0 environment. This sign change – occurring twice per orbit for all particles except for those near the minimum amplitude libration – is likely the reason for the higher order harmonics, as has been found when studying the i-Ω-space of a particle unperturbed by Jupiter in Section 4.10. In the system of this thesis, all test particles of the simulations start their orbit in the magnetic north, which is why the higher order harmonics all have the same shape. A periodic flip in the sign between the two regions could either lead to a dampening of the variations in i and Ω, or it could excite them. Either way, this effect would likely most strongly influence the particles initially starting within or near the minimum libration amplitude solution. These are the ones that would pass through the heliospheric current sheet most often, as their orbital planes oscillate around it, and therefore would likely experience the greatest effect of the polarity change occurring every 11 yr.

In order to test the effect of a reversed polarity on the particle motion and the resulting orientation within the i-Ω-space, another simulation was also done with a factor of $-B_0$ to

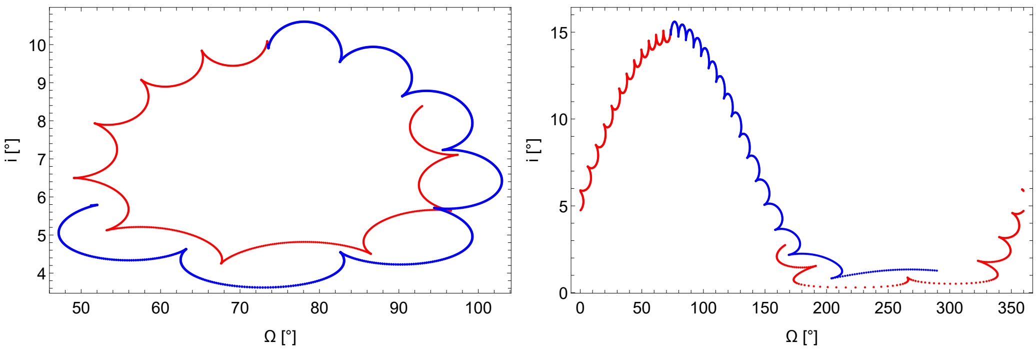

(a) i_0=10° (b) i_0=15°

Figure 5.1.: Difference in the orientation within the i-Ω-phase space for two initial inclinations (with $\Omega_0 = 73.5°$ for both) in the case of a positive B_0 (blue) and a negative B_0 (red).

compute the results for two test orbits of a 2 µm particle on both a rotational and a librational orbit. The other parameters are again set to those given in Table 4.1. While the previous simulation runs have always shown a clockwise motion within the parameter space, going first to higher Ω values (in the case of $i_0 > 7.15°$ and vice versa for initially smaller inclinations), the opposite is the case for the reversed magnetic field, as can be seen in Figure 5.1. Additionally, the evolution also shows a change in the behaviour of the higher order harmonics, as the maximum of one case corresponds to a minimum in the other case, while the fundamental oscillation remains the same in either scenario, showing only a small time delay and shift in the resulting inclination values. This corresponds to the conclusion drawn from Section 4.10, that the higher order harmonics correspond to the sign change (and hence to the orbital period), as they now show the exact opposite shape.

The results of Figure 5.1 may indicate that the change of polarity – as the evolution in the i-Ω-space changes its orientation – may lead to a dampening of the oscillations rather than an excitation in the long run, when implementing the influence of the solar cycle and considering the ensuing constant change in polarity. It is difficult, however, to make more precise assumptions about this effect as it would be necessary to study it in more detail. Previous studies (e.g. Fahr, Scherer and Banaszkiewicz 1995; Moro-Martín and Malhotra 2003) have suggested that the inclusion of the solar cycle would likely mean that the overall influence of the magnetic field averages out on longer timescales. This possibility cannot be ruled out, as the orientation within the magnetic field changes, while the structures remain the same. Therefore, it could be that there is no 'net effect' after several years. However, it should also be kept in mind that – depending on the initial conditions of the particle – the periods of the oscillations are different, meaning that the orbits nearest the minimum amplitude solution can likely complete one full variation period before the polarity changes due to the solar cycle. So it seems likely that a distinction will need to be made between different orbits and their behaviours when affected by the solar cycle, as well. In Moro-Martín and Malhotra 2003, the authors have also pointed out this dependence of the effect of the sign reversal on the orbital plane, as well as on the orbital period (and hence the solar distance). Specifically, they mention the influence of the Lorentz force on charged particles trapped in resonance with Jupiter as a potential case for a non-zero 'net effect'.

Additionally, this thesis utilises the assumption that the magnetic dipole axis and the rotation axis of the sun have the same orientation, meaning that the current sheet lies wholly within the equatorial plane. This is not necessarily the case as has been pointed out in Section 3.3.1 and is discussed in more detail in Lhotka and Narita 2019, which presents the 'ballerina skirt' model among others (see also e.g. Alfvén 1977). This structure further complicates the considerations of the minimum amplitude solution especially, as there would be no initial configuration that would allow the particle's orbital plane to remain aligned with the current sheet for prolonged periods of time. This is already difficult for a 'flat' shape, due to the additional perturbations introduced by Jupiter in this case. In terms of the full dynamics in the i-Ω-space, this model would introduce additional polarity changes in combination with the effect of the solar cycle on all orbits. This is because of the waviness of the current sheet, which leads to different sections in the solar system. These correspond to regions either above or below this boundary even though the particles in those regions have the same inclination, for example. As they move on their orbit, this therefore leads to more frequent polarity changes of the magnetic field, as it acts on the particles.

The orientation of the dipole axis depends on the tilt angle, as explained in Section 3.3.1, which in this thesis is assumed to be zero. As Jokipii and Thomas 1981 states, this is only approximately accurate at solar minimum, and the angle varies strongly with the solar activity, which – in combination with the rotation of the sun – lead to the wavy structure of the current sheet. Results of Thomas and Smith 1981 suggest that, in the regions closest to the sun, the current sheet can be seen as flat and only becomes of a wavier shape further outward, which indicates that dust further inwards of the solar system may behave differently than the dust near Jupiter also simply due to the structure of the current sheet. This would mean that the dust in the outer solar system is more heavily affected by both the effect of the solar cycle and the shape of the current sheet.

The earlier assumption of this section – that particles with initial conditions resulting in librational orbits should be differentiated from the orbits resulting in longer period oscillations – is perhaps negligible when also taking into account this effect of the tilt angle. It is unlikely that the particle would complete one full orbit without passing through several sections, which could imply that the effect of the magnetic field may indeed average out over time for all cases. However, this does not necessarily have to be the case. It could also be that, upon polarity reversal, the further evolution is quite different from before, as the particle now has different 'initial' orbital properties, meaning that the reversed field lines will likely not create the exact opposite of the structure in the i-Ω-space. The resulting oscillations of the orbital plane may, therefore, be quite different to the initial shape, leading to an overall change in its orientation on longer timescales. Hence, the effect may not average out at all, but instead we may yet find an excitation of the inclinations, as was proposed earlier. The full complex structure of the interplanetary magnetic field will need to be studied in much more detail in future works, however, to be able to find more definitive answers.

5.3. The effect of resonance and solar distance

The discussions so far have mostly focused on the differences in the evolution of the inclination of charged dust particles in 1 : 1 mean motion resonance with Jupiter, with the exception of one

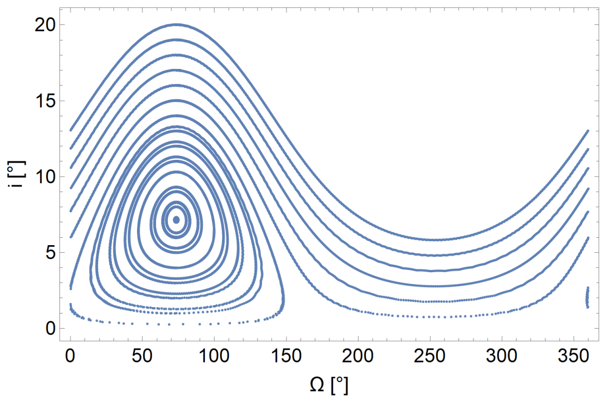

Figure 5.2.: The i-Ω-space for a 10 µm particle.

type of simulation set-up testing the effects of the Lorentz force outside of resonance in more detail, as seen in Figure 4.17b. As discussed in Sections 4.9 and 4.10, it has been found that the short-period oscillations (the higher order harmonics) are present in all cases for different solar distances, even when excluding the influence of Jupiter. The planetary effects are only noticeable for the minimum amplitude solution, as the planet pushes the orbital plane of the particle in resonance out of its equilibrium position more quickly than in the case further away from the perturber. As the particle out of resonance was placed at $a_0 = 3\,\mathrm{AU}$, the resulting variation of the minimum amplitude solution is smaller likely due to the combined effect of a less significant 'nudge' by Jupiter and the shorter orbital periods.

Further comparisons of different simulation runs of Section 4.5 have also shown, however, that a similar result of reduced strength of the higher order harmonics is obtained when slightly increasing the particle radius. This can be seen in Figure 5.2 for a particle size of 10 µm. We can infer that the reduced effect of the Lorentz force primarily leads to a loss of the higher order harmonics and hence – most interestingly when looking at the effect of Jupiter – also a reduced oscillation of the minimum amplitude libration. This implies that the effect of Jupiter in pushing the particle's orbital plane outside of its equilibrium position can only occur if the Lorentz force itself is strong enough to drive stronger oscillations in turn.

For the resonance itself, the results of Lhotka and Galeş 2019 suggest that the Lorentz force could lead to a faster escape from the resonance. This is connected to the results of this thesis, as the Lorentz forces induces large variations (of typically around 14°) from the particle's initial inclination, leading to higher values especially for initially smaller ecliptic latitudes. As the orbital elements are coupled according to their Gauss equations, this also influences other parameters, such as the eccentricity for example, perhaps eventually placing the particle further away from the resonant region. Hence, this would facilitate the dominance of the other forces such as the Poynting-Robertson effect, resulting in an inward 'drag' on the particle, effectively moving it away from the resonance (for a discussion of this effect, see for example Lhotka and Celletti 2015). However, even though the Poynting-Robertson effect typically leads to an inward-spiral of dust particles, Liou and Zook 1995 have found that particles which have emerged from inside the 1 : 1 resonance with Jupiter may still stay inside this system for some thousand years. Similarly, Lhotka, Bourdin and Narita 2016 have found that there are certain charge to mass ratios (depending on solar distance) that balance out the inward drag of the Poynting-Robertson effect, leading to secularly stable motions even outside of resonance. Whether this or an earlier escape would be more likely for specific particles is difficult to say from these simplified simulations of singular particles. However, it is likely that the smallest particles (displaying the largest amplitude changes and fastest oscillations in i and Ω, Figure 4.6) are likely to be the first to leave the system due to their more chaotic orbits. The additional force terms acting on the particles would then either lead them further inward towards the sun or place them on a trajectory leading outwards. Either way – but likely especially in the latter case – the particles may get trapped in other mean motion resonances, as well.[26]

Outside of resonance, the Lorentz force also plays a role in increasing the ecliptic latitude of the dust particles, as has been seen in Section 4.10. In a more realistic system, however, this force term also has to compete with the Poynting-Robertson effect and the solar radiation pressure. As neither of these forces influence the inclination or the longitude of the ascending node directly (due to the lack of a normal component, e.g Klacka 1992), it seems probable that the results of Figure 4.17b may yet be applicable even though the simulations have not taken the additional force terms into consideration. On the other hand, taking into account the parameters in the equations (3.21) and (3.22), it should be noted that they both depend on a factor of $\frac{1}{a^2}$. As the Poynting-Robertson effect reduces the eccentricity and, more importantly in this case, the semi-major axis (e.g. Wyatt and Whipple 1950), this could indicate that we may even find a further increase or at least some kind of significant change in the orbital evolution of i and Ω due to the combination of the Lorentz force and the Poynting-Robertson effect. In any case, due to the continuous decrease in solar distance, the inclusion of these additional force terms will likely lead to a decrease in the amplitudes and periods in the oscillations of i and Ω, according to the results of Figure 4.18.

Additionally, when considering the effect of these other force terms, the results of Zhou et al. 2021 should also be kept in mind, namely a resulting asymmetry between the two Lagrange points for different types of orbits in the e-ω-space. The combination with the Lorentz force – and due to the coupling of the Kepler elements from the equations of motion – in this case may also lead to an asymmetry in the structure of the i-Ω-space. To confirm this, however, it will be necessary to implement the influence of the radiation pressure and the Poynting-Robertson effect into the equations. It would, perhaps, be especially interesting to do this with the analytical model for the case of Venus to compare the results to those of Zhou et al. 2021. However, this would go beyond the scope of this thesis.

5.4. Second equilibrium solution

As explained in Section 4.8, it is possible to approximately infer the location of the minimum amplitude solution directly from the Gauss equations (3.21) and (3.22) by equating them to zero and solving for the initial conditions (i_0, Ω_0). According to these equations, it is apparent that a second extremum can be found as well, as it is necessary to do a distinction of cases. Considering the results in Figure 4.2, it appears that this extremum is found for particles with an $\Omega_0 = 253.5°$, as the inclinations display a minimum at this value in all simulation runs. This

[26] Lhotka and Galeş 2019 have found that the Lorentz force terms do not influence the capture process in that case.

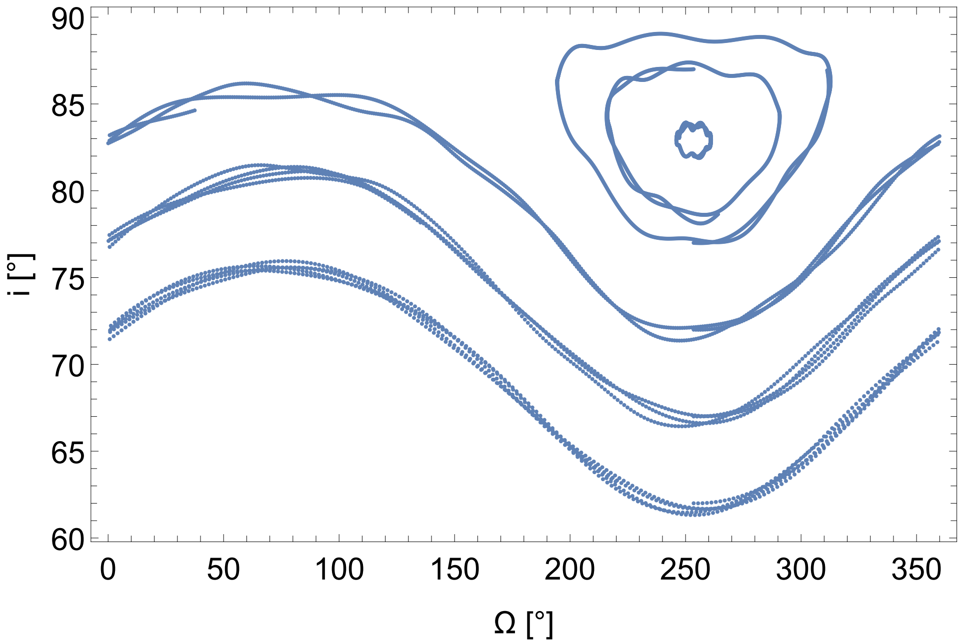

Figure 5.3.: The second 'equilibrium solution' from the results of the Gaussian approximation.

would align the particle's ascending node with the other node of the intersection line of the solar equator and the ecliptic.

After running a simulation with the initial condition set of $(i_0, \Omega_0) = (7.15°, 253.5°)$, it became apparent that rather than finding another minimum amplitude libration, the computation resulted in an oscillation of a relatively long period, as well as a large amplitude in the evolution of the inclination (not shown here). It was comparable in its form to the orbits within the rotational regime seen so far. The next step was therefore to refer back to the equations using this new Ω_0 value to derive the corresponding i_0 resulting in zero for both (3.21) and (3.22). With this new value, the appropriate initial inclination for the second extremum was found to be around i_0 =82.639° in the Gaussian approximation. The resulting shape in the i-Ω-space of a few simulation runs with a few different i_0 can be seen in Figure 5.3.

Similarly to what has been explained earlier in Section 4.8, the approximated value does differ slightly from the (expected) real value. It seems likely that the actual value, which needs to be used in the Newton equations to correctly position the orbital plane, is $i_0 = 82.85°$ (or, alternatively, $i_0 = 90° - 7.15°$). However, several test runs with the Newton equations have shown (not pictured here) that initial inclinations higher than around 45° resulted in very different oscillations in the i-Ω-space in comparison to the structure which has become expected from Figure 4.2. The oscillations are far less regular and eventually also show a complete deviation from a periodic evolution, making it impossible to differentiate between any librational and rotational orbits.

So, while it was possible to find this second equilibrium solution in the Gaussian approximation, from both the equations and the results seen in Figure 5.3, we note that the same could not be done using the full Newton solution, which is curious. Perhaps particles with initially high ecliptic latitudes are affected differently by the Lorentz force than particles starting near the ecliptic. In Lhotka and Galeş 2019, the authors point out that the approximation of the *tanh*-term they used in the Gaussian equations is valid only for moderate inclinations. This could mean that the results for the second minimum amplitude solution found in Gauss may not represent the real case due to the high initial inclination necessary to place the particle there. In any case, with the assumption that (most of) the particles near the Jupiter Trojan region originate from collisions of these asteroids, it is unlikely that many – if any – of these particles start their orbit at such great ecliptic latitudes.

5.5. Success and limitations of the Gaussian approximation

The results of Chapter 4 have shown that the Gaussian model can reproduce the main features in the i-Ω-space very well near the Lagrange points (see e.g. Figure 4.2 or 4.13). Because of this, it is possible to discern between the different dynamical regimes (librational and rotational behaviour) in the Gaussian representation as well as in the Newton solutions, allowing both a quantitative and qualitative comparison. It is possible to do this without adjusting the α parameter, as the phase space does not show the temporal effects of the evolution. Interestingly, α also does not seem to influence the resulting amplitudes, as the overall shape of the results (as seen in Figure 4.13c) is comparable to those of the Newton solutions. On the other hand, the Gaussian approximation does not yield accurate results for the frequencies of the oscillation without an adjustment in comparison to the Newton solution. However, as this can be done very easily in an automated process that does not prolong the integration process significantly, it does not pose a problem or introduce any inaccuracies. It should be kept in mind that the model does display an approximation error on longer timescales, leading to the open rotational curves seen in Figure 4.2 in the Gaussian results. In order to analyse the parameter space, it is therefore preferable to only compute one full period of the oscillation.

Perhaps the biggest restriction of the Gaussian model is its limitation to a certain particle size range. As discussed in Section 4.5, the smallest values for the particle radius used in the simulations yielded very different results in the i-Ω-space using the full Newtonian solution (i.e. Figure 4.8a), and further tests have shown that they cannot be reproduced with the Gaussian approximations. Therefore, this model can be applied for medium-sized and large particles, while the evolution of the smallest objects of $R \leq 1\,\mu\text{m}$ likely either needs to be studied in more detail in a full numerical study rather than an analytical approximation, or a different approach needs to be made in the derivations of the equations. It might prove beneficial to start with variation equations using the assumption of the dominant Lorentz force rather than gravity. This could be done by creating another model based on the dominance of the magnetic field in the generalized form of the Hamiltonian, for example, as can also be done for the solar gravity.

As a number of simulations were done with the full Newton solution for different orbits, it also has to be pointed out that the same was done using the Gaussian approximation only for the two Lagrange points and the tadpole orbit. As the variation equations due to the planetary perturber were derived for the case of $r \sim r_1$ in Section 3.2.1, this part of the approximation works only for particles with a semi-major axis the same as (or at least close to) that of planet Jupiter. This model can therefore not be used to recreate the results of the simulation run of the case out of resonance, as the equations would not be accurate for a case of $r < r_1$. For a more in-depth study of different locations in the solar system, it would be good to create separate models of the perturber problem, for the different relations between r and r_1, and then select which one to use for every simulation run, to also study particles at greater distances to Jupiter. This is especially important for particles moving on an orbital plane near the equilibrium, as the results indicate that the planet induces the variation around that position. On the other hand, for particles with higher initial inclinations, specifically in the case of the rotational regime in the i-Ω-space, it would theoretically be possible to use this model in simulations outside of the resonance as well. This is because further away from the minimum amplitude solution, the gravitational effect of Jupiter in the variation of the orbital plane is not noticeable in any case, and the results are dominated by the influence of the magnetic field. Therefore, the general structure of the parameter space remains the same and is comparable to the Newton results even out of resonance. Hence, it could be said that the model – combining equations (3.11) – (3.16) with (3.21) and (3.22) – can qualitatively recreate the structure of the i-Ω-space for charged particles regardless of particle position. Nevertheless, it would be best to switch off the influence of Jupiter completely when studying different particle positions, as otherwise the wrong set of equations would be used. This only yields accurate results because of the strength of the influence of the interplanetary magnetic field on dust particles in comparison to the influence of the planet.

It is also interesting to note, that the model can seemingly be applied to a more complex case study of the interplanetary magnetic field as well, as it can also recreate the results of a changing polarity in B_0, as was briefly discussed for the Newton equations in Section 5.2. Hence, it is reasonable to assume that the model would likely be able to reproduce the effects of the solar cycle and, more specifically, the resulting change in polarity. However, in order to incorporate the varying tilt angle and the accompanying variation of the – so far flat – heliospheric current sheet, the full equation of the Lorentz force (3.19) would need to be adjusted accordingly, which would likely lead to a different form of the Gauss equations than what is found for (3.21) and (3.22). However, by adapting the model accordingly, it should be possible in future works to further advance the model to include a more complex magnetic field structure, with which these effects can be studied analytically, as well.

5.6. Concluding Remarks

The main goal of this thesis was to study the basic behaviour of the inclination of charged dust particles trapped in the 1:1 mean motion resonance with Jupiter, as they interact with the interplanetary magnetic field. This was done by conducting a parameter study with two approaches: first, by doing full numerical simulations using the Newton equations of motion, and second, by creating a model using the Gauss equations and implementing the secular terms of both the perturbing body and of the magnetic field. In doing so, it was possible to create an analytical model reproducing the characteristic features in the parameter space of the inclination and the longitude of the ascending node due to the Lorentz force terms. For the computations, a simplified magnetic field model was used based on the Parker spiral model. We assumed a dipole structure, resulting in a magnetic north and a magnetic south with the so-called heliospheric current sheet as the boundary layer. This region is flat and aligned with the equatorial plane of the sun in our computations, as we did not include any time-dependent effects into the magnetic field model, such as the solar cycle. For the inclusion of Jupiter's influence into the analytical model, an approximation of the perturbing potential was used for the case of $r \sim r_1$. Hence, it can only be applied for particles in 1:1 mean motion resonance with the planet. For the majority of the computations, the particles were therefore initialised at the L4 point. The main results of the simulations and of the comparisons between the two approaches are summarised in the following:

(i) It has been found from the simulations and a closer look at the Gauss equations of the Lorentz term (Section 4.2) that the i-Ω-space shows a maximum in the inclination at Ω =73.5°. Alternatively speaking, the particle reaches its largest value in the ecliptic latitude when the ascending node of its orbit passes the intersection of the ecliptic and the equatorial plane, so as it coincides with one of the nodes of the heliospheric current sheet.

(ii) The parameter space in Figure 4.2 also shows two different regimes of motion in the osculating elements. We find a librational regime, in which the ascending node of the particle oscillates only between smaller values, for particles with initial inclinations of up to 14° and an Ω_0 in the range of 20° to 130°. For other initial conditions, the particle's orbital planes display a rotational motion, passing through all possible values of Ω and reaching amplitudes of around $\Delta i \sim 14°$ in all cases. (We note that this distinction disappears in the proper elements, Section 4.6.) The interplanetary magnetic field therefore induces a wide spread in the vertical distribution of the particles.

(iii) For the set of initial conditions $(i_0, \Omega_0) = (7.15°, 73.5°)$ (or, alternatively speaking, for particles whose orbital planes are initially located within the current sheet), a minimum libration amplitude solution is found, only showing small, non-periodic variations without discernible long-period oscillations, as discussed in Section 4.8. Comparisons to the results of simulations of a particle located at 3 AU and of a particle completely unperturbed by a planet (Figure 4.15 and Section 4.10) have shown that these variations are likely caused by the influence of Jupiter. The planetary perturbations lead to an early disruption of what would otherwise be an equilibrium position within the parameter space.

(iv) Additionally, a study in i_0 and U_0 was done for particles located in L4 but outside of the equilibrium condition of the i-Ω-space in Section 4.7. The case of $\Omega_0 = 0°$ did not show the separation into the two dynamical regimes. Upon varying that parameter, it became apparent that the librational region is only found for larger values of more than at least Ω_0 =15°, corresponding to what has been concluded from the full representation in the i-Ω-space.

The investigations have shown that the analytical model is able to replicate the amplitudes of the oscillations in those two orbital elements accurately in most cases (and hence the general structure of the i-Ω-space), while it cannot reproduce the exact oscillation frequency independently of additional computations (compare Figure 4.13). This is due to the modelling of the physical effect of the heliospheric current sheet. The correction of the period can be done by running both the Newton integration and the Gaussian model and subsequently adjusting the parameter accordingly. By doing this, the model can also accurately reproduce the temporal evolution of the orbital plane. The model does have limitations in recreating the results of the minimum amplitude solution, both for the correct initial value and the exact motion resulting form that. This is because the model only takes into account the secular effects of the force terms. The variation caused by Jupiter and then further amplified by the Lorentz force is, however, not a regular long-term effect, and the model is therefore unable to accurately reproduce the behaviour of such a particle. This is only a small exception, though, as all other modelled orbits in the initial inclination range of $[1, 20]^\circ$ have shown a very good agreement with the full solution (as seen e.g. in Figure 4.2).

We note that the model can only be applied in a specific range of particle size, namely for particles of $R \geq 2\,\mu\text{m}$ (Section 4.5). For smaller bodies, the Lorentz force would dominate, rendering the equations incorrect, as they assume the dominant force term to be the solar gravity. On the other hand, an upper limit for the particle size can be set to around $200\,\mu\text{m}$, according to the results analysed in proper elements space (Section 4.6). This is not necessarily a limit for the applicability of the model itself, but rather of the dominance of the effect of the interplanetary magnetic field in comparison to Jupiter. At around this particle size, the influence of the Lorentz force becomes comparable to that of the planet, resulting only in small changes of i and Ω on longer timescales.

The parameter study has shown that an increase in the charge to mass ratio due to the increase in the surface potential of the particle (Section 4.5) results in higher frequencies in the variation of i and Ω. However, it does not affect the amplitude of the oscillation significantly, at least not for typical values expected for that parameter, ranging here from 0.5 V to 5 V. On the other hand, the strong increase in the ratio that occurs for smaller particles does show a significant change in the behaviour of the orbit, as it leads to larger amplitudes and a loss of temporal regularity. This indicates that the smallest particles are likely more uniformly distributed in space than the larger objects of $R \geq 2\,\mu\text{m}$, which display periodic oscillations.

Comparisons of different orbits (Section 4.9) have shown that the interplanetary magnetic field always influences the dynamics in the i-Ω-space in a similar way, regardless of the particle location relative to Jupiter. It typically results in an underlying secular oscillation with superimposed higher order harmonics (again, with the exception of the orbits near the minimum amplitude solution). Further simulations without the influence of Jupiter (Section 4.10) have shown that these higher order harmonics are a direct result of the sign change occurring twice per orbit, i.e. their period lengths are the same as the particle's orbital period at a given distance (Figure 4.18c). Therefore, both the period and amplitude of these variations increase with solar distance. The same trend is found for the secular oscillation. The characteristic features of the orbital evolution for a charged dust particle in 1:1 resonance with Jupiter can therefore mostly be traced back to the influence of the Lorentz force terms. The effect of Jupiter itself is likely only dominant for orbital planes orientated close to the heliospheric current sheet. We do note the importance of the resonance in keeping the particle on a stable orbit on longer timescales, allowing the Lorentz force to act on the body without other perturbations to the orbit caused by additional force terms (such as the Poynting-Robertson effect or the solar radiation pressure). For the investigations into the isolated effect of the magnetic field at different solar distances, it should therefore be kept in mind that, outside of resonances, the particles consistently move further inward (or outward) of the solar system. This will likely lead to continually decreasing amplitudes and shorter periods in the oscillations of the orbital planes.

Evidently, the interplanetary magnetic field has a vital role in distributing charged dust particles towards more extreme ecliptic latitudes. The full extent of the change in the orientation of the orbital plane strongly depends on the initial conditions, as well as on the charge to mass ratio of the particle, and the shape of the heliospheric current sheet. Future inclusion of the solar cycle and the sector structure of the magnetic field into both the full numerical integrations and the analytical model should aid in placing further constraints on the spatial distribution of charged dust particles in the outer solar system.

A. Series expansion solutions

The series expansion for the eccentric anomaly E, true anomaly θ, true longitude u and the radius r in the eccentricity e up to the second order yields:

$$
\begin{aligned}
E &= M + e\sin(M) + \frac{1}{2}e^2\sin(2M) \\
\theta &= M + 2e\sin(M) + \frac{5}{4}e^2\sin(2M) \\
\sin(E) &= \left(1 - \frac{e^2}{8}\right)\sin(M) + \frac{1}{2}e\sin(2M) + \frac{3}{8}e^2\sin(3M) \\
\cos(E) &= -\frac{e}{2} + \left(1 - \frac{3e^2}{8}\right)\cos(M) + \frac{1}{2}e\cos(2M) + \frac{3}{8}e^2\cos(3M) \\
\sin(\theta) &= \left(1 - \frac{7e^2}{8}\right)\sin(M) + e\sin(2M) + \frac{9}{8}e^2\sin(3M) \\
\cos(\theta) &= -e + \left(1 - \frac{9e^2}{8}\right)\cos(M) + e\cos(2M) + \frac{9}{8}e^2\cos(3M) \\
\cos(u) &= \cos(M)\cos(\omega) - \sin(M)\sin(\omega) + ((-1 + \cos(2M))\cos(\omega) - \sin(2M)\sin(\omega))e \\
&\quad + \left(-\frac{9}{8}(\cos(M) - \cos(3M))\cos(\omega) + \left(\frac{7\sin(M)}{8} - \frac{9}{8}\sin(3M)\right)\sin(\omega)\right)e^2 \\
\sin(u) &= \cos(\omega)\sin(M) + \cos(M)\sin(\omega) + (\cos(\omega)\sin(2M) + (-1 + \cos(2M))\sin(\omega))e \\
&\quad + \left(\cos(\omega)\left(-\frac{7\sin(M)}{8} + \frac{9}{8}\sin(3M)\right) - \frac{9}{8}(\cos(M) - \cos(3M))\sin(\omega)\right)e^2 \\
r &= \frac{1}{2}\left(ae^2 + 2a\right) - ae\cos(M) - \frac{1}{2}ae^2\cos(2M)
\end{aligned}
$$

The series expansion for the components in the position and velocity vector in e up to the second order yields:

$$
\begin{aligned}
x = &\frac{1}{16}ae^2(\cos(i) + 1)\cos(M - \omega - \Omega) - \frac{3}{16}ae^2(\cos(i) - 1)\cos(3M + \omega - \Omega) \\
&- \frac{1}{16}ae^2(\cos(i) - 1)\cos(M - \omega + \Omega) + \frac{3}{16}ae^2(\cos(i) + 1)\cos(3M + \omega + \Omega) \\
&+ \frac{1}{4}a\left(e^2 - 2\right)(\cos(i) - 1)\cos(M + \omega - \Omega) - \frac{1}{4}a\left(e^2 - 2\right)(\cos(i) + 1)\cos(M + \omega + \Omega) \\
&- \frac{1}{4}ae(\cos(i) - 1)\cos(2M + \omega - \Omega) + \frac{1}{4}ae(\cos(i) + 1)\cos(2M + \omega + \Omega) \\
&+ \frac{3}{4}ae(\cos(i) - 1)\cos(\omega - \Omega) - \frac{3}{4}ae(\cos(i) + 1)\cos(\omega + \Omega)
\end{aligned}
$$

$$\begin{aligned} y = &-\frac{1}{16}ae^2(\cos(i)+1)\sin(M-\omega-\Omega)+\frac{3}{16}ae^2(\cos(i)-1)\sin(3M+\omega-\Omega) \\ &-\frac{1}{16}ae^2(\cos(i)-1)\sin(M-\omega+\Omega)+\frac{3}{16}ae^2(\cos(i)+1)\sin(3M+\omega+\Omega) \\ &-\frac{1}{4}a\left(e^2-2\right)(\cos(i)-1)\sin(M+\omega-\Omega)-\frac{1}{4}a\left(e^2-2\right)(\cos(i)+1)\sin(M+\omega+\Omega) \\ &+\frac{1}{4}ae(\cos(i)-1)\sin(2M+\omega-\Omega)+\frac{1}{4}ae(\cos(i)+1)\sin(2M+\omega+\Omega) \\ &-\frac{3}{4}ae(\cos(i)-1)\sin(\omega-\Omega)-\frac{3}{4}ae(\cos(i)+1)\sin(\omega+\Omega) \end{aligned}$$

$$\begin{aligned} z = &-\frac{1}{8}ae^2\sin(i)\sin(M-\omega)+\frac{3}{8}ae^2\sin(i)\sin(3M+\omega)-\frac{1}{2}a\left(e^2-2\right)\sin(i)\sin(M+\omega) \\ &+\frac{1}{2}ae\sin(i)\sin(2M+\omega)-\frac{3}{2}ae\sin(i)\sin(\omega) \end{aligned}$$

$$\begin{aligned} v_x = &-\frac{1}{16}ae^2n(\cos(i)+1)\sin(M-\omega-\Omega)+\frac{9}{16}ae^2n(\cos(i)-1)\sin(3M+\omega-\Omega) \\ &+\frac{1}{16}ae^2n(\cos(i)-1)\sin(M-\omega+\Omega)-\frac{9}{16}ae^2n(\cos(i)+1)\sin(3M+\omega+\Omega) \\ &-\frac{1}{4}a\left(e^2-2\right)n(\cos(i)-1)\sin(M+\omega-\Omega)+\frac{1}{4}a\left(e^2-2\right)n(\cos(i)+1)\sin(M+\omega+\Omega) \\ &+\frac{1}{2}aen(\cos(i)-1)\sin(2M+\omega-\Omega)-\frac{1}{2}aen(\cos(i)+1)\sin(2M+\omega+\Omega) \end{aligned}$$

$$\begin{aligned} v_y = &-\frac{1}{16}ae^2n(\cos(i)+1)\cos(M-\omega-\Omega)+\frac{9}{16}ae^2n(\cos(i)-1)\cos(3M+\omega-\Omega) \\ &-\frac{1}{16}ae^2n(\cos(i)-1)\cos(M-\omega+\Omega)+\frac{9}{16}ae^2n(\cos(i)+1)\cos(3M+\omega+\Omega) \\ &-\frac{1}{4}a\left(e^2-2\right)n(\cos(i)-1)\cos(M+\omega-\Omega)-\frac{1}{4}a\left(e^2-2\right)n(\cos(i)+1)\cos(M+\omega+\Omega) \\ &+\frac{1}{2}aen(\cos(i)-1)\cos(2M+\omega-\Omega)+\frac{1}{2}aen(\cos(i)+1)\cos(2M+\omega+\Omega) \end{aligned}$$

$$\begin{aligned} v_z = &-\frac{1}{8}ae^2n\sin(i)\cos(M-\omega)+\frac{9}{8}ae^2n\sin(i)\cos(3M+\omega) \\ &-\frac{1}{2}a\left(e^2-2\right)n\sin(i)\cos(M+\omega)+aen\sin(i)\cos(2M+\omega) \end{aligned}$$

B. Zusammenfassung

Das Ziel dieser Masterarbeit ist die Studie der grundlegenden Effekte des interplanetaren Magnetfelds auf die Inklination eines geladenen Staubteilchens in 1:1 Resonanz mit Jupiter. Beobachtungen des Zodiakallichts, welches durch die Streuung von Licht an µm-großen Staubteilchen entsteht, haben gezeigt, dass es hauptsächlich entlang der Ekliptik zu sehen ist, aber auch, dass Staubteilchen bei höheren Inklinationen vorhanden sind. Die Herkunft und die Ursache dieser Verteilung ist noch unklar. Eine mögliche Erklärung ist, dass die Lorentz-Kraft, die auf die geladenen Staubteilchen wirkt, zu starken Schwankungen der ekliptischen Höhen führen kann, was sich auch in den Ergebnissen der Arbeit zeigte. Um im Speziellen die säkulare Entwicklung der geladenen, μm-großen Teilchen in koorbitaler Bewegung mit Jupiter zu untersuchen, wurde ein semi-analytisches Modell entwickelt mit Fokus auf die Entwicklung der Inklination und der Länge des aufsteigenden Knotens. Diese Bahnelemente werden am stärksten von der Lorentz-Kraft beeinflusst und werden daher genutzt, um die Teilchenbewegung genauer zu studieren. Mithilfe der Gaussgleichungen war es möglich, die Bewegungsgleichungen der Bahnelemente auf die dynamisch relevanten Terme zur Beschreibung der Langzeitentwicklung des Orbits zu reduzieren. Dazu wurden Methoden der Reihenentwicklung und der zeitlichen Mittelung verwendet. Zusätzlich wurden die Bewegungsgleichungen in der Newton-Darstellung verwendet, um numerisch die vollständige Dynamik der Staubteilchen zu berechnen.

Das Modell reproduziert die Hauptcharakteristiken der Struktur im Parameterraum der Inklination und der Länge des aufsteigenden Knotens, insbesondere das Auftreten von sowohl Rotations- als auch Librationsbahnen, sowie eine Lösung mit minimaler Amplitude. Letztere steht im Zusammenhang mit einer Gleichgewichtslösung für den Einfluss der Lorentz-Kraft. Die weiteren Resultate der im Anschluss durchgeführten Parameter-Studie zeigten, dass das Modell am besten für Teilchen mit mittleren und größeren Radien ($\geq 2\,\mu$m) funktioniert. Diese Objekte zeigen periodische Schwingungen in der Inklination, welche die Berechnung mit dem Modell erlauben. Die Orbitebenen der kleinsten Teilchen verhalten sich laut den Ergebnissen der numerischen Berechnungen nicht periodisch.

Zusätzlich weisen die Ergebnisse darauf hin, dass die Nähe zu Jupiter der Grund für die (frühe) Auslenkung aus der Gleichgewichtslage ist, da der Planet zusätzliche Störungen in den Bahnelementen auslöst. Der Einfluss von Jupiter beeinflusst den Parameterraum aber nicht weiter wesentlich. Simulationen des isolierten Effekts des interplanetaren Magnetfelds deuten an, dass die Orbitebenen dieselben Oszillationen aufweisen wie im Fall mit dem Planeten, nämlich eine Superposition aus einer säkularen Schwingung (reproduzierbar mit dem Modell) und Oberschwingungen mit kürzeren Perioden (in den vollständigen Newton-Lösungen). Tests für Teilchenpositionen mit verschiedenen Entfernungen zur Sonne weisen auf, dass diese Variationen von höherer Frequenz mit den Orbitperioden des Teilchens zusammenhängen.

Über den kombinierten Effekt des Magnetfelds und des Jupiters kann gesagt werden, dass die Lorentz-Kraft den dominanten Einfluss in der Langzeitentwicklung der Orbitebene von μm-großen Teilchen angibt. Das im Zuge der Arbeit entwickelte semi-analytische Modell kann verwendet werden, um diese säkularen Effekte für verschiedene Teilcheneigenschaften zu untersuchen.

List of Figures

List of Tables

Bibliography

Alfvén, H. (Aug. 1977). 'Electric currents in cosmic plasma.' In: *Reviews of Geophysics and Space Physics* 15, pp. 271–284. DOI: 10.1029/RG015i003p00271 (cit. on p. 81).

Beauge, C. (Oct. 1994). 'Asymmetric Librations in Exterior Resonances'. In: *Celestial Mechanics and Dynamical Astronomy* 60.2, pp. 225–248. DOI: 10.1007/BF00693323 (cit. on p. 33).

Beaugé, C. and F. Roig (Oct. 2001). 'A Semianalytical Model for the Motion of the Trojan Asteroids: Proper Elements and Families'. In: *Icarus* 153.2, pp. 391–415. DOI: 10.1006/icar.2001.6699 (cit. on p. 47).

Beck, J. G. and P. Giles (Mar. 2005). 'Helioseismic Determination of the Solar Rotation Axis'. In: *ApJ* 621.2, pp. L153–L156. DOI: 10.1086/429224 (cit. on p. 41).

Berriman, G. B. et al. (Aug. 1994). 'COBE DIRBE Near-Infrared Polarimetry of the Zodiacal Light: Initial Results'. In: *ApJ* 431, p. L63. DOI: 10.1086/187473 (cit. on p. 5).

Brouwer, D. and G. M. Clemence (1961). *Methods of celestial mechanics* (cit. on p. 59).

Burns, J. A., P. L. Lamy and S. Soter (Oct. 1979). 'Radiation forces on small particles in the solar system'. In: *Icarus* 40.1, pp. 1–48. DOI: 10.1016/0019-1035(79)90050-2 (cit. on p. 7).

Carrington, R. C. (1863). *Observations of the spots on the sun from November 9, 1853, to March 24, 1861, made at Redhill* (cit. on p. 41).

Dermott, S. F. et al. (Dec. 1984). 'Origin of the Solar System dust bands discovered by IRAS'. In: *Nature* 312.5994, pp. 505–509. DOI: 10.1038/312505a0 (cit. on p. 5).

Dikarev, V. et al. (Aug. 2005). 'Update of the ESA Meteoroid Model'. In: *4th European Conference on Space Debris*. Ed. by D. Danesy. Vol. 587. ESA Special Publication, p. 271 (cit. on p. 8).

Dvorak, R. and C. Lhotka (2013). *Celestial dynamics : : chaoticity and dynamics of celestial systems*. eng. Weinheim : Wiley-VCH, ISBN: 9783527651856 (cit. on p. 20).

Espy, A. J. et al. (Feb. 2009). 'Evidence from IRAS for a very young, partially formed dust band'. In: *Planet. Space Sci.* 57.2, pp. 235–242. DOI: 10.1016/j.pss.2008.06.011 (cit. on p. 5).

Fahr, H. J., K. Scherer and M. Banaszkiewicz (Feb. 1995). 'The evolution of the zodiacal dust cloud under plasma drag and Lorentz forces in the latitudinally asymmetric solar wind'. In: *Planet. Space Sci.* 43.3, pp. 301–312. DOI: 10.1016/0032-0633(94)00174-P (cit. on p. 80).

Fitzpatrick, R. (2012). *An Introduction to Celestial Mechanics* (cit. on pp. 9, 10, 12, 14–16, 18, 20, 22, 58).

Gradshteyn, I. S. and I. M. Ryzhik (1980). *Table of integrals, series and products* (cit. on p. 20).

Grün, E., B. A. S. Gustafson et al. (June 1994). 'Interstellar dust in the heliosphere'. In: *A&A* 286, pp. 915–924 (cit. on p. 38).

Grün, E., H. A. Zook et al. (Apr. 1993). 'Discovery of Jovian dust streams and interstellar grains by the Ulysses spacecraft'. In: *Nature* 362.6419, pp. 428–430. DOI: 10.1038/362428a0 (cit. on p. 5).

Gustafson, B. A. S. (Feb. 1989). 'Comet Ejection and Dynamics of Nonspherical Dust Particles and Meteoroids'. In: *ApJ* 337, p. 945. DOI: 10.1086/167164 (cit. on p. 6).

– (Jan. 1994). 'Physics of Zodiacal Dust'. In: *Annual Review of Earth and Planetary Sciences* 22, pp. 553–595. DOI: 10.1146/annurev.ea.22.050194.003005 (cit. on p. 76).

Hanner, M. S. et al. (1976). 'Pioneer 10 Observations of Zodiacal Light Brightness Near the Ecliptic: Changes with Heliocentric Distance'. In: *Interplanetary Dust and Zodiacal Light*. Ed. by H. Elsaesser and H. Fechtig. Vol. 48, p. 29. DOI: 10.1007/3-540-07615-8_448 (cit. on p. 5).

Hansen, C. J. et al. (Mar. 2006). 'Enceladus' Water Vapor Plume'. In: *Science* 311.5766, pp. 1422–1425. DOI: 10.1126/science.1121254 (cit. on p. 5).

Jewitt, D. C., C. A. Trujillo and J. X. Luu (Aug. 2000). 'Population and Size Distribution of Small Jovian Trojan Asteroids'. In: *AJ* 120.2, pp. 1140–1147. DOI: 10.1086/301453. arXiv: astro-ph/0004117 [astro-ph] (cit. on p. 75).

Jokipii, J. R. and B. T. Thomas (Feb. 1981). 'Effects of drift on the transport of cosmic rays. IV - Modulation by a wavy interplanetary current sheet'. In: *ApJ* 243, pp. 1115–1122. DOI: 10.1086/158675 (cit. on pp. 40, 81).

Kimura, H., H. Okamoto and T. Mukai (June 2002). 'Radiation Pressure and the Poynting-Robertson Effect for Fluffy Dust Particles'. In: *Icarus* 157.2, pp. 349–361. DOI: 10.1006/icar.2002.6849 (cit. on p. 6).

Klacka, J. (Dec. 1992). 'Poynting-Robertson Effect - Part Two - Perturbation Equations'. In: *Earth Moon and Planets* 59.3, pp. 211–218. DOI: 10.1007/BF00054053 (cit. on p. 83).

Koschny, D. et al. (June 2019). 'Interplanetary Dust, Meteoroids, Meteors and Meteorites'. In: *Space Sci. Rev.* 215.4, 34, p. 34. DOI: 10.1007/s11214-019-0597-7 (cit. on pp. 5, 7, 8).

Kresak, L. (Jan. 1976). 'Orbital Evolution of the Dust Streams Released from Comets'. In: *Bulletin of the Astronomical Institutes of Czechoslovakia* 27, p. 35 (cit. on p. 7).

Krivov, A., H. Kimura and I. Mann (Aug. 1998). 'Dynamics of Dust near the Sun'. In: *Icarus* 134.2, pp. 311–327. DOI: 10.1006/icar.1998.5949 (cit. on pp. 7, 76).

Landgraf, M. (May 2000). 'Modeling the motion and distribution of interstellar dust inside the heliosphere'. In: *J. Geophys. Res.* 105.A5, pp. 10303–10316. DOI: 10.1029/1999JA900243. arXiv: astro-ph/9906300 [astro-ph] (cit. on p. 76).

Lemaitre, A. (June 1993). 'Proper Elements - what are they'. In: *Celestial Mechanics and Dynamical Astronomy* 56.1-2, pp. 103–119. DOI: 10.1007/BF00699724 (cit. on p. 58).

Lhotka, C., P. Bourdin and Y. Narita (Sept. 2016). 'Charged Dust Grain Dynamics Subject to Solar Wind, Poynting-Robertson Drag, and the Interplanetary Magnetic Field'. In: *ApJ* 828.1, 10, p. 10. DOI: 10.3847/0004-637X/828/1/10. arXiv: 1608.07040 [astro-ph.EP] (cit. on pp. 7, 38, 82).

Lhotka, C. and A. Celletti (Apr. 2015). 'The effect of Poynting-Robertson drag on the triangular Lagrangian points'. In: *Icarus* 250, pp. 249–261. DOI: 10.1016/j.icarus.2014.11.039. arXiv: 1412.1630 [astro-ph.EP] (cit. on pp. 31, 32, 82).

Lhotka, C. and C. Galeş (Nov. 2019). 'Charged dust close to outer mean-motion resonances in the heliosphere'. In: *Celestial Mechanics and Dynamical Astronomy* 131.11, 49, p. 49. DOI: 10.1007/s10569-019-9928-y. arXiv: 1911.02778 [astro-ph.EP] (cit. on pp. 6, 7, 32, 39–43, 45, 51, 52, 55, 67, 76, 78, 79, 82, 83, 85).

Lhotka, C. and Y. Narita (May 2019). 'Kinematic models of the interplanetary magnetic field'. In: *Annales Geophysicae* 37.3, pp. 299–314. DOI: 10.5194/angeo-37-299-2019 (cit. on pp. 39, 40, 81).

Lhotka, C., N. Rubab et al. (Oct. 2020). 'Charging time scales and magnitudes of dust and spacecraft potentials in space plasma scenarios'. In: *Physics of Plasmas* 27.10, 103704, p. 103704. DOI: 10.1063/5.0018170 (cit. on pp. 7, 78).

Liou, J. C. and H. A. Zook (Feb. 1995). 'An Asteroidal Dust Ring of Micron-Sized Particles Trapped in the 1:1 Mean Motion Resonance with Jupiter'. In: *Icarus* 113.2, pp. 403–414. DOI: 10.1006/icar.1995.1030 (cit. on pp. 7, 8, 69, 82).

– (Aug. 1997). 'Evolution of Interplanetary Dust Particles in Mean Motion Resonances with Planets'. In: *Icarus* 128.2, pp. 354–367. DOI: 10.1006/icar.1997.5755 (cit. on p. 7).

Liu, X. and J. Schmidt (Jan. 2018a). 'Dust arcs in the region of Jupiter's Trojan asteroids'. In: *A&A* 609, A57, A57. DOI: 10.1051/0004-6361/201730951. arXiv: 1801.03128 [astro-ph.EP] (cit. on pp. 7, 8, 75–77).

– (June 2018b). 'Comparison of the orbital properties of Jupiter Trojan asteroids and Trojan dust'. In: *A&A* 614, A97, A97. DOI: 10.1051/0004-6361/201832806. arXiv: 1805.04932 [astro-ph.EP] (cit. on pp. 7, 8, 44, 75).

Mann, I. et al. (Dec. 2010). 'Dust in the interplanetary medium'. In: *Plasma Physics and Controlled Fusion* 52.12, 124012, p. 124012. DOI: 10.1088/0741-3335/52/12/124012. arXiv: 1008.1742 [physics.space-ph] (cit. on p. 7).

Matsumoto, T. et al. (Sept. 2018). 'Zodiacal Light Beyond Earth Orbit Observed with Pioneer 10'. In: *AJ* 156.3, 86, p. 86. DOI: 10.3847/1538-3881/aad0f0. arXiv: 1808.03759 [astro-ph.EP] (cit. on p. 5).

May, B. H. (2007). *A Survey of Radial Velocities in the Zodiacal Dust Cloud*. DOI: 10.1007/978-0-387-77706-1 (cit. on p. 5).

McNamara, H. et al. (Dec. 2004). 'Meteoroid Engineering Model (MEM): A Meteoroid Model For The Inner Solar System'. In: *Earth Moon and Planets* 95.1-4, pp. 123–139. DOI: 10.1007/s11038-005-9044-8 (cit. on p. 8).

Morbidelli, A. (2002). *Modern celestial mechanics : aspects of solar system dynamics* (cit. on pp. 9, 12, 17, 19, 58).

Moro-Martín, A. and R. Malhotra (Apr. 2003). 'Dynamical Models of Kuiper Belt Dust in the Inner and Outer Solar System'. In: *AJ* 125.4, pp. 2255–2265. DOI: 10.1086/368237. arXiv: astro-ph/0506703 [astro-ph] (cit. on p. 80).

Moulton, F. R. (1914). *An introduction to celestial mechanics* (cit. on p. 25).

Murray, C. D. and S. F. Dermott (1999). *Solar system dynamics*.

– (2000). *Solar System Dynamics*. Cambridge University Press. DOI: 10.1017/CBO9781139174817 (cit. on pp. 32, 58, 59).

Parker, E. N. (Nov. 1958). 'Dynamics of the Interplanetary Gas and Magnetic Fields.' In: *ApJ* 128, p. 664. DOI: 10.1086/146579 (cit. on pp. 7, 39).

Robertson, H. P. (Apr. 1937). 'Dynamical effects of radiation in the solar system'. In: *MNRAS* 97, p. 423. DOI: 10.1093/mnras/97.6.423 (cit. on p. 6).

Smith, E. J. (Aug. 2001). 'The heliospheric current sheet'. In: *J. Geophys. Res.* 106.A8, pp. 15819–15832. DOI: 10.1029/2000JA000120 (cit. on pp. 40, 79).

Smith, E. J., B. T. Tsurutani and R. L. Rosenberg (Feb. 1978). 'Observations of the interplanetary sector structure up to heliographic latitudes of 16°: Pioneer 11'. In: *J. Geophys. Res.* 83.A2, pp. 717–724. DOI: 10.1029/JA083iA02p00717 (cit. on p. 40).

Sterken, V. J. et al. (Oct. 2019). 'Interstellar Dust in the Solar System'. In: *Space Sci. Rev.* 215.7, 43, p. 43. DOI: 10.1007/s11214-019-0607-9 (cit. on p. 5).

Thomas, B. T. and E. J. Smith (Dec. 1981). 'The structure and dynamics of the heliospheric current sheet'. In: *J. Geophys. Res.* 86.A13, pp. 11105–11110. DOI: 10.1029/JA086iA13p11105 (cit. on p. 81).

Webb, G. M. et al. (Oct. 2010). 'Homotopy formulas for the magnetic vector potential and magnetic helicity: The Parker spiral interplanetary magnetic field and magnetic flux ropes'. In: *Journal of Geophysical Research (Space Physics)* 115.A10, A10112, A10112. DOI: 10.1029/2010JA015513 (cit. on pp. 7, 39, 76).

Wyatt, S. P. and F. L. Whipple (Jan. 1950). 'The Poynting-Robertson effect on meteor orbits'. In: *ApJ* 111, pp. 134–141. DOI: 10.1086/145244 (cit. on p. 83).

Zhou, L. et al. (Jan. 2021). 'Dynamics of charged dust in the orbit of Venus'. In: *A&A* 645, A63. ISSN: 1432-0746. DOI: 10.1051/0004-6361/202039617. URL: http://dx.doi.org/10.1051/0004-6361/202039617 (cit. on pp. 68, 77, 83).